Experimental and Numerical Investigations into Terahertz Time-Domain Spectroscopy

by

Aidan Schiff-Kearn

Thesis submitted to the
Faculty of Graduate and Postdoctoral Studies
In partial fulfillment of the requirements
For the M.Sc. degree in
Master of Science in Physics

Ottawa-Carleton Institute of Physics
Faculty of Science
University of Ottawa

Abstract

This Master's thesis presents numerical and experimental results that benchmark a state-of-the-art terahertz time-domain spectrometer. We begin by describing the theory behind the nonlinear optical mechanisms through which we generate and detect short pulses of THz radiation. Based on a coherent electro-optic detection scheme, our measurements trace out the oscillating electric field of the THz pulses generated from the optical mixing process of optical rectification. A numerical simulation based on the theory presented in this work helps present the physical intuition behind our use of these nonlinear optical processes and is furthermore used to complement our measurements with theory. Utilizing the simultaneous amplitude and phase information provided by our detection scheme, we perform terahertz time-domain spectroscopy on sample materials. Our samples of interest are the III-V zinc-blende semiconductors GaP and ZnTe which are nonlinear media popular for their advantageous dispersive and absorptive properties in the terahertz range. Therefore, the thesis culminates in the demonstration of a material parameter extraction procedure which we use to obtain the complex refractive index of a GaP crystal and a ZnTe crystal.

Acknowledgements

I wish to thank my supervisor Prof. Jean-Michel Ménard for giving me the opportunity to pursue this Master's thesis. His passion for terahertz science is infectious and his dedication to the craft inspirational. I also have untold gratitude for my lab-partner-in-crime Wei Cui who helped me grow both as a scientist and as a person these last two years. And thanks for showing me where to get the best Chinese food in Ottawa. Moreover, I would like to thank the many talented undergraduate students who helped brighten our dimly lit lab from its humble beginnings, in particular Nicolas Couture and Emily Zhang for their hard work and deserved successes. Thank you to Murat Yildirim, a great post-doc whom I'm glad to call my friend.

Over the course of this thesis, I had the pleasure of working with many esteemed colleagues both local and abroad. Thank you to Profs. Robert Boyd, Ksenia Dolgaleva, Ravi Bhardwaj and Jean-Michel Ménard for fostering an invigorating environment in which to do terahertz science. I am also extremely thankful to Rubert Huber and his research group who kicked my scientific senses into high gear by welcoming me into their group for a short time. A special thanks to Profs. Paul Corkum and Ravi Bhardwaj and their research groups at the University of Ottawa for hosting us for the first year of my thesis until we were able to move in to a lab of our own.

Most importantly, above all, thank you to my family for their love, patience and unconditional support. Thanks, Hannah, for holding up the fort while I'm away.

Table of Contents

List of Tables

List of Figures

CV

Publications

1. L. Gingras, W. Cui, **A. W. Schiff-Kearn**, J.-M. Ménard, and D. G. Cooke, "Active phase control of terahertz pulses using a dynamic waveguide," *Optics Express* **26**, 13876 (2018).

2. W. Cui, **A. W. Schiff-Kearn**, E. Zhang, N. Couture, F. Tani, D. Novoa, P. St.J. Russell, and J.-M. Ménard, "Broadband and tunable time-resolved THz system using argon-filled hollow-core photonic crystal fiber," *APL Photonics* **3**, 111301 (2018).

Conference Proceedings

1. W. Cui, **A. W. Schiff-Kearn**, E. Zhang, N. Couture, F. Tani, D. Novoa, P. St.J. Russell, and J.-M. Ménard, "Frequency-tunable THz source using Ar-filled HC-PCF pulse shaper," *Proceedings of Photonics North 2018*, Montreal, QC (2018).

2. L. Gingras, W. Cui, **A. W. Schiff-Kearn**, J.-M. Ménard, and D. G. Cooke, "Phase control of broadband THz pulses," *Proceedings of Photonics North 2018*, Montreal, QC (2018).

3. L. Gingras, W. Cui, **A. W. Schiff-Kearn**, J.-M. Ménard, and D. G. Cooke, "All-optical phase control of THz waveforms," *Proceedings of the 43rd International Conference on Infrared, Millimeter, and Terahertz Waves*, Nagoya, Japan (2018). In print.

Statement of originality and collaborative contributions

To the best of his knowledge, the author states that the work described in this Master's thesis constitutes original research in the field of physics. Jean-Michel Ménard initiated the work. Wei Cui and Aidan Schiff-Kearn collected the data. Aidan Schiff-Kearn devised the theoretical model and analysed the data. All authors designed the experiments. Zi Qi Lin and Jean-Michel Ménard designed the homebuilt autocorrelator while Nicolas Couture and Wei Cui maintained and operated it.

Chapter 1

Introduction

Light is a prime driver of scientific pursuits both fundamental and technological. The eminence of light traces its heritage back to the 1950s, a period which saw the invention of the maser become the development of the laser [1, 2]. This marriage of optics and electronics took place at one of the most pivotal moments in the lineage of light, when Arthur Schawlow and Charles Townes extended the idea of stimulated microwave amplification into the visible and infrared [3]. In so doing, their manoeuvre surged interest into these optical domains and helped spark the etymological change from maser to laser, as is colloquial today. The coherent nature of the laser cemented its widespread use, despite first being described as "a solution looking for a problem" [4]. However, a challenge remained in accessing longer wavelengths in the far-infrared where sources and detectors remained incoherent and narrow in spectral coverage [5]. For the purposes of broadband spectroscopy, this difficulty persisted until the advent of the Ti:Sapphire laser in the late 1980s [6] in large part due to the work of such pioneers as David Auston [7], Martin Nuss [8] and Dan Grischkowsky [9]. In this thesis, I will take advantage of this age-old momentum to explore the comparatively unexplored region in the terahertz (THz) domain. This introductory chapter seeks to provide a basic perspective on the ongoing development of THz science and motivates the use of nonlinear optical methods for generating and detecting broadband pulses of THz radiation. For the interested reader, a historical account of experimental access to the THz regime is expertly outlined in Ref. [10].

Situated in between the microwave and far-infrared regions, THz radiation bridges the gap between the worlds of electronics and photonics. Its extent the electromagnetic spectrum is typically said to extend from 0.3 THz to 10 THz with respective sub-mm wavelengths from 1 mm to 30 μm [11], as shown in Figure 1.1. Historically, this so-called terahertz gap has been defined by the limitations of its neighbours. However, the last couple of decades have seen a marked shift in perspective as a result of the massive proliferation of technology racing to fill the region with sources and detectors. Namely, new solid-state optoelectronic platforms have demonstrated broad spectral coverage at THz frequencies [12]. One exciting ongoing development is the THz quantum cascade laser, a compact and specially-engineered semiconductor source, which has recently demonstrated spectral coverage of 1-5 THz at up to mW powers at room temperature [13], earning it top spot on the roadmap for next-generation THz technology in 2017 [14].

In 2014, Lewis reviewed the exponential growth of the word "terahertz" appearing in the literature in abstracts, titles or keyword fields and found an approximate doubling every 3 years since 1975 [15]. This trend continues in large part due to the wide adoption of

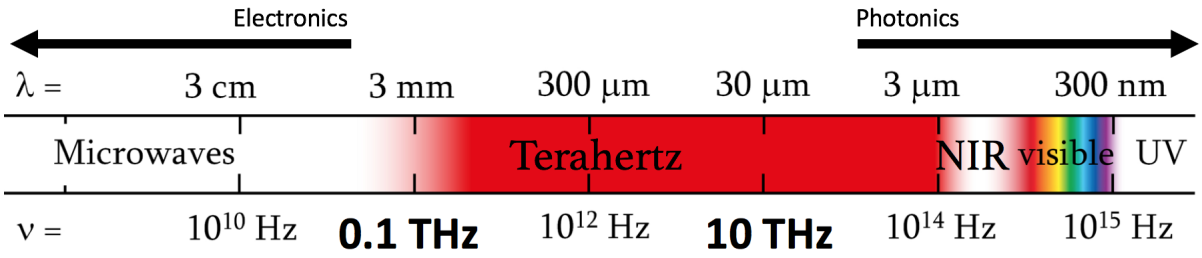

Figure 1.1: Terahertz-centric map of the electromagnetic spectrum.

terahertz time-domain spectroscopy (THz-TDS) ever since its inception in the mid 1980s. A typical experimental apparatus for THz-TDS contains three main parts: the source to generate the THz radiation, optical components to manipulate the radiation and finally a detection scheme to perform the measurement. The spectroscopic technique then relies on introducing a sample before detection and comparing the measured signal to another obtained in its absence. The earliest versions of THz-TDS were borne out of such milestones as the *Auston* switch for which the activation of ultrafast currents in a photoconductive material using short pulses of light causes emission or reception at THz frequencies [16, 17]. Grischkowsky *et al.* added an optical approach to this technique by capturing and refocusing the emitted THz radiation in free space using a Si lens mounted to the device [18]. Soon afterwards, a version of electro-optic sampling (EOS) in free space was integrated into the scheme and continues to this day to be one of the broadest coherent detection schemes available for sensing pulsed THz radiation [19]. Based on the well-known linear electro-optic effect, the reach of EOS has even been demonstrated as far as the near-infrared [20].

The emergence of THz-TDS as a powerful tool for investigations into material properties beyond the far-infrared owes a great deal of its success to the application of the chirped pulse amplification technique to optical sources starting in 1985 [21]. This act put into the hands of every laser experimentalist a high-intensity source of visible or near-infrared laser pulses of duration in the tens to hundreds of femtoseconds (note 1 fs = 10^{-15} s). Interestingly, the concept of chirped pulse amplification was first realized out of the need to increase the average power of radar pulses whose high intensities would otherwise break the electric circuit [22]. This transposition of radar technology to optical applications helped facilitate access to non-resonant nonlinear optical mechanisms as alternative approaches to THz generation. In short, irradiation by light of high intensity perturbs the optical response of a material as a nonlinear function of the incident light field which results in the emission of light at new frequencies.

The particular nonlinear effect utilized in this thesis to generate the THz radiation is the inverse electro-optic effect [23], which came into prominence alongside the *Auston* switch and other advances in the fabrication of crystalline semiconductor devices [24]. Commonly known as optical rectification [25], this optical mixing process is a result of a quasi-DC (i.e. time-varying) material polarization formed by the action of an ultrashort pulse focused to high intensity in a nonlinear medium with second-order nonlinearity, resulting in the coherent build-up and eventual emission of pulsed THz radiation. Like any other nonlinear optical process, the efficiency in the down-conversion of pump light to THz frequencies is subject to phase-matching conditions that depend on the dispersive and absorptive properties of the nonlinear medium of choice [26]. A list is given in Table 1.1 of a variety of popular electro-optic crystals that have been used to generate THz pulses using optical

Table 1.1: Electro-optic crystals commonly used for generating THz radiation via optical rectification, categorized by type.

Semiconductors	**Inorganics**	**Organics**
GaP [35]	$LiNbO_3$ [28]	DAST [36]
ZnTe [37]	$LiTaO_3$ [38]	HMQ-TMS [39]
GaAs [40]		LAPC [41]
GaSe [29]		DSTMS [42]

rectification. In this thesis, we utilize and analyze the III-V zinc-blende semiconductors GaP and ZnTe. Since a frequency of 1 THz corresponds to a photon energy of 4.1 meV, the maximum energy conversion efficiency typically attained for optical rectification is around 10^{-3}. Modern efforts to improve the conversion efficiency have turned towards the structuring of media that display large nonlinear coefficients, following the success of the tilted-pulse-front technique with $LiNbO_3$ in generating high energy THz pulses [27, 28]. Other modern strategies include quasi-phase-matching methods [29, 30], air-based THz generation [31] and the use of organic crystals such as DAST [32] which all now regularly produce focused THz field strengths on the order of MV/cm [33]. In turn, the maturation of these methods for high-intensity broadband THz generation has ushered in the era of nonlinear spectroscopy experiments in the THz range [34].

The leading mechanisms for generating broadband THz pulses rely on two vital components: a high-intensity femtosecond laser to seed the nonlinear interactions and knowledge of the optical properties of the nonlinear medium. The former has seen a persistent trend towards higher central wavelengths of operation out from the visible and into the mid-infrared as the powerful techniques of Kerr-lens modelocking and chirped pulse amplification are put to use with new solid-state gain media such as Yb:KGW [43], Ho:YAG [44] and Cr:Mg_2SO_4 [42]. In this thesis, we use near-infrared femtosecond pulses from an amplified Yb:KGW laser to address the latter and realize a THz time-domain spectrometer. We combine efficient THz generation via optical rectification with its subsequent coherent detection via electro-optic sampling. The field-sensitive EOS technique affords both amplitude and phase information of the electric field of a THz pulse in the time domain. Using THz-TDS, we extract simultaneously the dispersive and absorptive properties of a material under study in the THz beam by performing two measurements: one in the presence of the sample in the path of the THz beam and the other in its absence. To reveal the frequency-dependence of the material response to the interrogating THz pulse, we compare the results of a numerical Fourier transform to the frequency domain performed on both datasets. For the relatively weak THz fields employed in this thesis, this analysis reveals the linear complex refractive index of the sample material.

Traditional far-infrared Fourier-transform spectrometers (FIR-FTS) utilize blackbody radiation sources, such as arc lamps or SiC globars, and bolometer detectors. As an established science, there exist a multitude of reviews on the design and methodology of material parameter extraction using an FIR-FTS, such as Ref. [45]. Although both THz-TDS and FIR-FTS derive spectral data from the use of the Fourier transform on their measured signals, a typical FIR-FTS collects intensity data which is insensitive to phase and is generally limited to frequencies greater than 3 THz. In contrast, the detection in THz-TDS

is coherent, allowing the extraction of both the real and imaginary optical properties of the material under study without having to resort to Kramers-Kronig relations which are generally subject to phase-correction issues [46]. The technique of THz-TDS is well-suited to probe low-frequency excitations in solid-state matter such as collective electronic motion (plasmons) [47], lattice mode vibrations (phonons) [48] and intra-excitonic transitions [49]. Besides applications in condensed matter, the relatively low THz photon energies involved in THz-TDS give it a niche in non-destructive, contact-free applications such as conservation science [50], quality control and differentiation of polymorphs for industry [51] and also especially at security checkpoints where the precise identification of questionable materials is of utmost importance [51]. Furthermore, the field-sensitivity of the THz-TDS technique has propelled it into other scientific disciplines including analytical chemistry and molecular biology [52, 53]. However, THz metrology is a science still in maturation. In this vein, a major goal of this thesis is to help address the need to formulate a standard practice with which one can use to organize a reliable library of spectral signatures in the THz domain for any material under study. Finally, the promise of the THz-TDS technique is the unambiguous determination of the complex optical properties of a sample material with or without distinct features such as resonance lines [54].

Chapter 2 presents the theory behind the nonlinear optical methods we use to generate and to detect pulses of THz radiation. First, the nonlinear wave equation is explicitly developed starting from Maxwell's equations for the optical mixing process of optical rectification. Next, our coherent electro-optic detection scheme is formulated based on the linear electro-optic effect. We begin with a time domain description of this effect in order to illustrate the method of electro-optic sampling of our THz pulses. The discussion then shifts into an equivalent frequency domain description in order to examine the spectral components of the THz radiation obtained at detection. At the heart of the theory is our treatment of short pulses of light which proceeds through the careful analysis of the phase-matching considerations in these nonlinear optical processes. In addition, the orientation of the zinc-blende crystals that serve as emitters and detectors of the THz radiation is investigated with respect to the polarizations of the involved light fields in order to maximize our signals. Along the way, a numerical simulation is constructed to help visualize the theory in the form of the spectral content of the calculated THz fields.

Chapter 3 walks through the experimental apparatus of our THz time-domain spectrometer. Our system incorporates the nonlinear optical mechanisms for the generation of THz pulses via optical rectification and their subsequent detection through electro-optic sampling as introduced in Chapter 2. We first discuss our PHAROS laser system which we use to seed these optical mixing processes with short, intense pulses of near-infrared light. Next, the typical operation of our THz spectrometer is outlined, resulting in the spectral analysis of the measured signals. Through lock-in detection, we register these weak signals and reject noise. The chapter ends with a comparison between an experimentally derived signal and the ideal result expected from the numerical simulation based on the theoretical treatment of Chapter 2.

Chapter 4 discusses THz-TDS in detail and outlines the numerical procedure we use to extract the complex refractive index of a material under study from our measured signals. This technique fundamentally relies on the coherent electro-optic detection scheme described in Chapter 3. The results of this procedure are documented for the III-V semiconductor crystals GaP and ZnTe.

Chapter 2

Theory and Modelling of Nonlinear Optical Processes

Chapter 1 explored the motivation and background for the nonlinear optical methods we will use in Chapter 3 to experimentally demonstrate the generation and detection of pulsed terahertz (THz) radiation. Herein we discuss these processes in explicit mathematical detail. The main goal of this chapter is to outline the physical considerations required to prepare a broadband THz time-domain spectrometer based on these nonlinear optical mechanisms. Working within the classical framework of Maxwell's equations, we derive expressions that predict the spectrum of THz pulses generated via optical rectification and subsequently detected through electro-optic sampling, a similar process of reversal that resolves the electric field of the THz pulse in the time domain. Specifically, the chapter begins with the derivation of a first-order differential equation one-dimensional in space that describes the propagation of a pulsed electromagnetic wave through a nonlinear medium used to drive the process of optical rectification. Afterwards, the generated THz pulse is carried through another nonlinear medium to act upon an optical gate via the linear electro-optic "Pockels" effect. To help realize the theoretical framework for our electro-optic detection scheme, we conclude by consulting the literature to develop an equivalent frequency-domain approach. Throughout the chapter, the efficient coupling between the low-frequency THz pulses and the near-infrared (NIR) pulses that seed these nonlinear interactions is addressed by carefully analysing phase-matching during the processes as well as the orientation of the nonlinear media with respect to the incoming light fields. A numerical simulation written in MATLAB based on our derived expressions illustrates our findings throughout the chapter.

2.1 The Nonlinear Optical Wave Equation

This investigation into nonlinear optics starts on the usual route with classical electromagnetic theory as described by Maxwell's equations [26, 55]. We set our focus on dielectric media that are nonmagnetic, homogeneous, dispersive and isotropic as embodied by the zinc-blende crystal class, examples of which include the semiconductors encountered throughout this thesis. These constraints suggest the use of the macroscopic version of Maxwell's equations which considers the volume-average of microscopic motion over, for

instance, unit cells in the semiconductor. These macroscopic equations take the form:

$$\nabla \times \vec{\boldsymbol{E}}(\vec{\boldsymbol{r}},t) = -\frac{\partial}{\partial t}\vec{\boldsymbol{B}}(\vec{\boldsymbol{r}},t) \qquad \text{(Faraday's law)} \tag{2.1}$$

$$\nabla \times \vec{\boldsymbol{H}}(\vec{\boldsymbol{r}},t) = \vec{\boldsymbol{J}}_f(\vec{\boldsymbol{r}},t) + \frac{\partial}{\partial t}\vec{\boldsymbol{D}}(\vec{\boldsymbol{r}},t) \qquad \text{(Ampère's law)} \tag{2.2}$$

$$\nabla \cdot \vec{\boldsymbol{B}}(\vec{\boldsymbol{r}},t) = 0 \qquad \text{(No magnetic monopoles)} \tag{2.3}$$

$$\nabla \cdot \vec{\boldsymbol{D}}(\vec{\boldsymbol{r}},t) = \rho_f(\vec{\boldsymbol{r}},t) \qquad \text{(Gauss's law)} \tag{2.4}$$

where $\vec{\boldsymbol{E}}(\vec{\boldsymbol{r}},t)$ and $\vec{\boldsymbol{H}}(\vec{\boldsymbol{r}},t)$ are respectively the electric and magnetic field vectors while $\vec{\boldsymbol{D}}(\vec{\boldsymbol{r}},t)$ and $\vec{\boldsymbol{B}}(\vec{\boldsymbol{r}},t)$ are the corresponding electric and magnetic flux densities. The uniform medium is neutral such that, in the absence of external fields, the negatively charged electrons perfectly screen the positively charged atomic nuclei. External fields can polarize these charges and induce electric dipole moments. Our interest is in the macroscopic electric polarization density $\vec{\boldsymbol{P}}(\vec{\boldsymbol{r}},t)$ that emerges in a medium lacking free currents ($\vec{\boldsymbol{J}}_f(\vec{\boldsymbol{r}},t) = \vec{\boldsymbol{0}}$) and free charge densities ($\rho_f(\vec{\boldsymbol{r}},t) = 0$). The following constitutive relations are defined:

$$\vec{\boldsymbol{D}}(\vec{\boldsymbol{r}},t) = \epsilon_0\vec{\boldsymbol{E}}(\vec{\boldsymbol{r}},t) + \vec{\boldsymbol{P}}(\vec{\boldsymbol{r}},t) \tag{2.5}$$

$$\vec{\boldsymbol{B}}(\vec{\boldsymbol{r}},t) = \mu_0\vec{\boldsymbol{H}}(\vec{\boldsymbol{r}},t) + \vec{\boldsymbol{M}}(\vec{\boldsymbol{r}},t) \tag{2.6}$$

where ϵ_0 and μ_0 are respectively the permittivity and permeability of free space. The assumption of nonmagnetic media zeroes the macroscopic magnetic polarization density as in $\vec{\boldsymbol{M}}(\vec{\boldsymbol{r}},t) = 0$. Combining the curl of eq. 2.1 with the equations 2.2 and 2.6 leads to the basic form of the wave equation:

$$\nabla \times \Big(\nabla \times \vec{\boldsymbol{E}}(\vec{\boldsymbol{r}},t)\Big) = -\mu_0\frac{\partial^2}{\partial t^2}\vec{\boldsymbol{D}}(\vec{\boldsymbol{r}},t) \tag{2.7}$$

To tackle the right hand side, the electric polarization density is expanded into its linear and nonlinear contributions so that eq. 2.5 becomes:

$$\vec{\boldsymbol{D}}(\vec{\boldsymbol{r}},t) = \epsilon_0\vec{\boldsymbol{E}}(\vec{\boldsymbol{r}},t) + \vec{\boldsymbol{P}}^{(1)}(\vec{\boldsymbol{r}},t) + \vec{\boldsymbol{P}}^{\mathrm{NL}}(\vec{\boldsymbol{r}},t) \tag{2.8}$$

Meanwhile, the left hand side of eq. 2.7 is replaced by the vector identity:

$$\nabla \times \big(\nabla \times \vec{\boldsymbol{E}}(\vec{\boldsymbol{r}},t)\big) = \nabla\big(\nabla \cdot \vec{\boldsymbol{E}}(\vec{\boldsymbol{r}},t)\big) - \nabla^2\vec{\boldsymbol{E}}(\vec{\boldsymbol{r}},t) \approx -\nabla^2\vec{\boldsymbol{E}}(\vec{\boldsymbol{r}},t) \tag{2.9}$$

where the above simplification is made by assuming that all applied electric fields are much weaker than atomic binding strengths E_{atom} [26]:

$$E_{\mathrm{atom}} = \frac{e}{4\pi\epsilon_0 a_0^2} \approx 5 \times 10^9 \text{ V/cm},$$

where e is the electron charge and a_0 is the Bohr radius. The nonlinear optical wave equation can now be expressed simply as:

$$\nabla^2\vec{\boldsymbol{E}}(\vec{\boldsymbol{r}},t) = \frac{1}{c^2}\frac{\partial^2}{\partial t^2}\Big(\vec{\boldsymbol{E}}(\vec{\boldsymbol{r}},t) + \frac{1}{\epsilon_0}\big(\vec{\boldsymbol{P}}^{(1)}(\vec{\boldsymbol{r}},t) + \vec{\boldsymbol{P}}^{\mathrm{NL}}(\vec{\boldsymbol{r}},t)\big)\Big) \tag{2.10}$$

having defined the speed of light in vacuum by $c = 1/\sqrt{\mu_0\epsilon_0}$.

2.1.1 Short Pulses and Fourier Decomposition

This section expresses eq. 2.10 in the context of short pulses. We first consider the following definitions of the Fourier transform and its inverse:

$$\vec{\boldsymbol{F}}(\vec{\boldsymbol{r}},\omega) \equiv \int_{-\infty}^{\infty} \vec{\boldsymbol{F}}(\vec{\boldsymbol{r}},t)\ \mathrm{e}^{-i\omega t}\ \mathrm{d}t \tag{2.11}$$

$$\vec{\boldsymbol{F}}(\vec{\boldsymbol{r}},t) \equiv \frac{1}{2\pi}\int_{-\infty}^{\infty} \vec{\boldsymbol{F}}(\vec{\boldsymbol{r}},\omega)\ \mathrm{e}^{i\omega t}\ \mathrm{d}\omega \tag{2.12}$$

where $\omega = 2\pi\nu$ is the angular frequency to which the regular frequency ν corresponds. In words, equation 2.12 states that any time-dependent function $\vec{\boldsymbol{F}}(\vec{\boldsymbol{r}},t)$ can be decomposed into an infinite sum of terms oscillating at different frequencies with specific amplitudes. The above definitions then allow us to recast eq. 2.10 to the frequency domain. Importantly, this mathematical representation lends itself to the language of short pulses which necessarily contain a broad range of frequencies.

A short pulse impinging on the medium is not quite an instantaneous event but rather one that extends over the duration of the pulse. The linear response of the medium to the action of the short pulse should then be expressed as a convolution integral in time. The associated Fourier pair is:

$$\vec{\boldsymbol{P}}^{(1)}(\vec{\boldsymbol{r}},t) = \epsilon_0 \int_{-\infty}^{t} \vec{\chi}^{(1)}(t-T)\vec{\boldsymbol{E}}(\vec{\boldsymbol{r}},T)\ \mathrm{d}T \tag{2.13}$$

$$\vec{\boldsymbol{P}}^{(1)}(\vec{\boldsymbol{r}},\omega) = \epsilon_0 \vec{\chi}^{(1)}(\omega)\vec{\boldsymbol{E}}(\vec{\boldsymbol{r}},\omega) \tag{2.14}$$

where $\vec{\chi}^{(1)}(\omega)$ is the Fourier transform of the linear susceptibility $\vec{\chi}^{(1)}(t)$. Therefore, the equivalent form of the nonlinear optical wave equation in the frequency domain is:

$$\nabla^2\vec{\boldsymbol{E}}(\vec{\boldsymbol{r}},\omega) = -\frac{\omega^2}{c^2}\left(\vec{\epsilon}^{\,(1)}(\omega)\vec{\boldsymbol{E}}(\vec{\boldsymbol{r}},\omega) + \frac{1}{\epsilon_0}\vec{\boldsymbol{P}}^{\mathrm{NL}}(\vec{\boldsymbol{r}},\omega)\right) \tag{2.15}$$

where the relative permittivity of the medium is related to the linear susceptibility and complex refractive index via $\vec{\epsilon}^{\,(1)}(\omega) = 1 + \vec{\chi}^{(1)}(\omega) = \tilde{n}^2(\omega)$. In the context of short pulses, equation 2.15 describes the propagation of a particular component $\vec{\boldsymbol{E}}(\vec{\boldsymbol{r}},\omega)$ of the total electric field $\vec{\boldsymbol{E}}(\vec{\boldsymbol{r}},t)$ of the pulse. In other words, this equation represents just one of a set of differential equations, each corresponding to a discrete frequency component within the bandwidth of the short pulse.

2.1.2 Plane Wave Decomposition

Besides assuming short pulses, no other restrictions have yet been made on the form of the electric fields. That said, the infinite plane wave assumption is now invoked to help solve the nonlinear optical wave equation. The reasoning is that in the absence of the nonlinear source term $\vec{\boldsymbol{P}}^{\mathrm{NL}}(\vec{\boldsymbol{r}},\omega)$, equation 2.15 reduces to the Helmholtz equation:

$$(\nabla^2 + \tilde{k}^2(\omega))\vec{\boldsymbol{E}}(\vec{\boldsymbol{r}},\omega) = \vec{\boldsymbol{0}} \tag{2.16}$$

where $\tilde{k}(\omega) = \tilde{n}(\omega)\omega/c$ is the complex wave-vector of the field component. Particular solutions to the Helmholtz equation include infinite plane waves [56]. Bringing the nonlinear polarization back into the mix, transverse changes in the field can still be neglected if we assume a sufficiently thin medium. The field component travelling in the direction of the z-axis is then also a plane wave but now modulated by a complex amplitude $\tilde{A}(z,\omega)$:

$$\vec{\boldsymbol{E}}(z,\omega) = \tilde{A}(z,\omega)\ \mathrm{e}^{i\tilde{k}(\omega)z}\vec{\boldsymbol{u}}, \tag{2.17}$$

where $\vec{\boldsymbol{u}}$ is the field polarization. Under the framework of the slowly-evolving-wave approximation [57], as prescribed for example by Sommer *et al.* [58], this complex amplitude is subject to the following constraint:

$$\left|\frac{\partial^2}{\partial z^2}\vec{\boldsymbol{A}}(z,\omega)\right| \ll \left|2i\tilde{k}(\omega)\frac{\partial}{\partial z}\vec{\boldsymbol{A}}(z,\omega) - \tilde{k}^2(\omega)\vec{\boldsymbol{A}}(z,\omega)\right| \tag{2.18}$$

which is better known as the slowly varying envelope approximation [26]. The physical implication of this approximation is that we can neglect backwards-propagating field components generated by the nonlinear polarization [55]. Inputting the forward component as given by eq. 2.17 into eq. 2.15 and performing some simple arithmetic produces the following equation which couples the generated field $\vec{\boldsymbol{E}}(z,\omega)$ to its source $\vec{\boldsymbol{P}}^{\mathrm{NL}}(z,\omega)$:

$$\frac{\partial}{\partial z}\vec{\boldsymbol{E}}(z,\omega) = \frac{i\omega}{2\epsilon_0\tilde{n}(\omega)c}\vec{\boldsymbol{P}}^{\mathrm{NL}}(z,\omega) \tag{2.19}$$

2.1.3 The Nonlinear Polarization

Equation 2.19 states that the solution to the nonlinear optical wave equation depends on the exact form of the nonlinear polarization. How does nonlinear behaviour arise in the presence of a short pulse? The answer lies in the interplay between the motions of the electrons and nuclear centres in the medium. As the short pulse passes through the medium, the electrons are compelled to move under the combined influence of its electric field and the restorative Coulomb force that binds them to their host nuclei. A sufficiently weak external field merely forces the electrons to oscillate about their equilibrium positions under simple harmonic motion at the bottom of Coulombic potential wells. In this case, Hooke's law is valid and the restorative force depends linearly on the electronic displacement which itself depends linearly on the external field. But if the field is strong enough to compete with the binding force, then the otherwise linear response is perturbed and Hooke's law breaks down. This situation is akin to stretching a spring to the point just before it snaps and releasing it: the spring will no longer shake symmetrically about its equilibrium point. In this case, the restorative force is no longer linear in the electronic displacement and so the electrons move instead in asymmetric potential wells as seen in Figure 2.1. This anharmonicity is modeled by expanding the polarization of the medium as a power series in terms of the applied field strength [26].

$$\vec{\boldsymbol{P}}(z,t) = \epsilon_0\left(\vec{\vec{\chi}}^{(1)}\cdot\vec{\boldsymbol{E}}(z,t) + \vec{\vec{\chi}}^{(2)}:\vec{\boldsymbol{E}}(z,t)^2 + \vec{\vec{\chi}}^{(3)}\vdots\vec{\boldsymbol{E}}(z,t)^3 + \ldots\right) \tag{2.20}$$

$$\equiv \vec{\boldsymbol{P}}^{(1)}(z,t) + \vec{\boldsymbol{P}}^{(2)}(z,t) + \vec{\boldsymbol{P}}^{(3)}(z,t) + \ldots \tag{2.21}$$

The tensor rank of the susceptibilities is one greater than the value of their superscripts in parentheses. Note that all of the terms after the first term, which is linear in field strength,

constitute the nonlinear term defined earlier in eq. 2.8. As a perturbation series, all of the terms in eq. 2.21 decrease in magnitude with increasing order. For the purpose of this thesis, we truncate the series to the second term, second-order in field strength. Notably, terms of even-order can only arise in noncentrosymmetric media, which lack inversion symmetry, since an asymmetric potential is required. For example, in the case of zinc-blende crystals, the different electronegativities of the two atom types in the lattice is responsible for the anharmonicity and therefore, importantly, a second-order nonlinearity.

In what follows, we will make use of the complex representation of the fields and material polarizations:

$$F(z,t) = \frac{1}{2}\sum_m \left(\tilde{F}(z,\omega_m)e^{-i\omega_m t} + c.c.\right) \tag{2.22}$$

where *c.c.* denotes the complex conjugate, ensuring real quantities, and $\tilde{F}(z,\omega_m)$ notates the complex amplitude of the m-th frequency component ω_m of the field or polarization at hand.

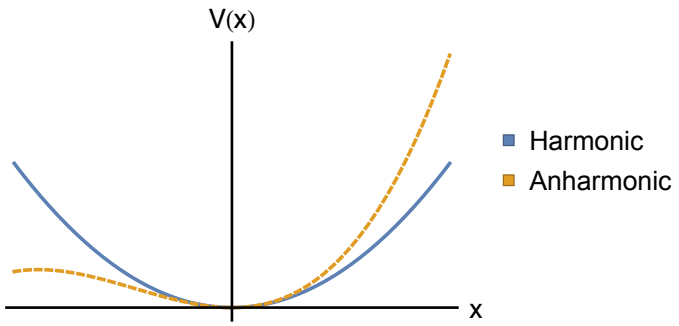

Figure 2.1: One-dimensional case of anharmonicity in the nonlinear response.

2.2 Optical Rectification

Optical rectification arises from the second-order nonlinearity of the medium as a type of optical mixing. Historically, optical rectification has referred to the creation of a static electric field across the medium which thereby establishes a DC polarization [26]. Analogously, in electronics, the unidirectional behaviour of diodes can be used to convert or "rectify" an AC signal into DC. However, in the presence of a short pulse, the optically-induced DC polarization evolves with the rise and fall of the electric field of the pulse. Consider the second-order nonlinear polarization that develops from two frequency components ω_1 and ω_2 within the bandwidth of the pulse:

$$P^{(2)}(t) \propto \chi^{(2)}E_1(t)E_2(t) = \chi^{(2)}\frac{E_0^2}{2}\Big(\cos\big((\omega_2-\omega_1)t\big) + \cos\big((\omega_2+\omega_1)t\big)\Big) \tag{2.23}$$

where $E_1(t) = E_0\cos(\omega_1 t)$ and $E_2(t) = E_0\cos(\omega_2 t)$. Clearly, equation 2.23 shows that any arbitrary pair of frequencies will establish components of the nonlinear polarization that oscillate either at the difference or the sum of their frequencies. Recalling that the nonlinear polarization shows up in the wave equation as a source term (see eq. 2.19), we consider now the two cases of the frequency pair being degenerate or nondegenerate. In

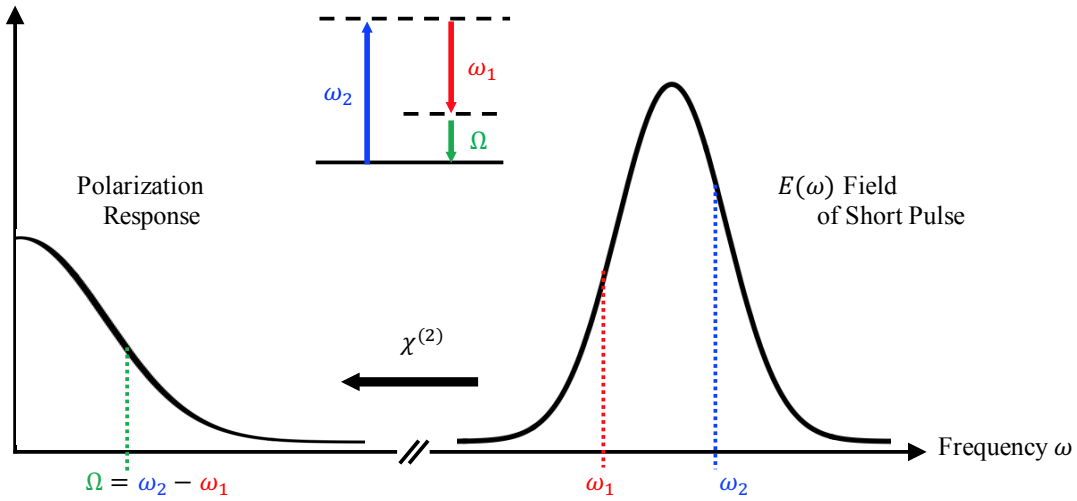

Figure 2.2: Pictorial representation of optical rectification shown with the energy-level diagram for intra-pulse difference frequency mixing. Adapted from [59].

the degenerate case, where $\omega_1 = \omega_2$, the conventional picture of optical rectification as a static polarization is recovered by the difference term, while the sum term corresponds to the second harmonic. However, it is easy to see that the nondegenerate case generalizes the second harmonic to a sum of any two frequency components. Similarly, the difference term also becomes a time-dependent source term when considering nondegenerate frequencies. For this thesis, ω_1 and ω_2 fall in the NIR so their difference lies in the THz range. Therefore, in the pursuit of generating broadband THz pulses, we take the broader view of optical mixing and consider optical rectification and intra-pulse difference frequency mixing as one and the same without loss of generality.

Figure 2.2 illustrates how NIR frequencies (for $\omega_2 > \omega_1$) produce a down-converted polarization at the THz frequency Ω at their difference through a second-order nonlinearity. Also drawn is the energy-level diagram ($\hbar = 1$) for the difference frequency mixing which shows that the underlying mechanism of this process involves the annihilation of one photon at ω_2 to enable the creation of the two photons at ω_1 and Ω. The solid line indicates the atomic ground state while the dashed lines are virtual states. These virtual states allow this non-resonant process to proceed through a superposition of real excited states of the system. Since they themselves are not eigenstates of the interaction Hamiltonian, they have indefinite energy and only exist within a time allowed by the Uncertainty Principle.

Since the sum and difference mixing terms in eq. 2.23 differ only by a minus sign, we treat positive and negative frequency components as distinct but related through the reality condition. The i-th Cartesian component of the second-order nonlinear polarization vector for a generalized sum frequency is given by [26]:

$$\tilde{P}_i^{(2)}(z, \omega_n + \omega_m) = \epsilon_0 \sum_{jk} \sum_{(nm)} \chi_{ijk}^{(2)}(\omega_n + \omega_m; \omega_n, \omega_m) \tilde{E}_j(z, \omega_n) \tilde{E}_k(z, \omega_m) \tag{2.24}$$

where the notation (nm) signifies that the sum $\omega_n + \omega_m$ is held fixed while performing the addition of ω_n and ω_m. In practice, the discrete sum extends over the entire spectral bandwidth of our short NIR pulse. We will use this generalized frequency-domain expression

to follow the optical mixing process of optical rectification by making the substitutions $\omega_n = \omega + \Omega$ and $\omega_m = -\omega$, where ω is an arbitrary NIR frequency component.

2.2.1 The Dispersion of $\chi^{(2)}$ in the Terahertz Regime

In the THz range, the presence of optical phonons distorts the electric susceptibility of the semiconductor media we consider throughout this thesis. Optical phonons are quanta of vibration that correspond to out-of-phase motion of neighbouring atoms in the lattice. Interestingly, light incident on the surface of a semiconductor cannot propagate if its frequency falls within the so-called reststrahlen band of the material. Coinciding with strong absorption, this highly reflective region on the short wavelength side of the far-infrared (typically $20 - 100$ μm [60]) lies in between the frequencies corresponding to the lowest longitudinal (LO) and transverse (TO) optical phonons. The spectral content of our laser imposes an upper limit on the THz light generated using optical rectification in this thesis, often below the reststrahlen band. The phonon contribution to the dielectric function of the material inflates the refractive index in the THz range as compared to that of the NIR which causes phase-matching concerns between the two kinds of pulses.

Historical efforts to measure the second-order nonlinear susceptibility of zinc-blende semiconducting crystals in the far-infrared date back to Raman scattering experiments performed by Faust and Henry in the late 1960s [61, 62]. In their experiment, optical mixing was observed in a gallium phosphide (GaP) crystal between a continuous-wave visible laser and various far-infrared laser lines. The authors modelled the nonlinear polarization induced about the reststrahlen band by treating the electric susceptibility as a linear combination of ionic displacement and the electric field of the visible light. At the frequency of the scattered light $\Omega = \omega_L - \omega_I$, with frequencies ω_L and ω_I respective of the visible laser and the infrared line, they empirically demonstrated that the frequency dependence of the electric susceptibility follows that of forced harmonic oscillation:

$$d(\Omega) = d_E\Big(1 + \frac{C\ \Omega_{\mathrm{TO}}^2}{\Omega_{\mathrm{TO}}^2 - \Omega^2 - i\Omega\Gamma_{\mathrm{TO}}}\Big), \tag{2.25}$$

where the nonlinear coefficient is defined as $d \equiv \chi^{(2)}/2$ and Ω_{TO} and Γ_{TO} are the TO angular frequency and phonon scattering rate, respectively. If both ω_L and ω_I are far from any resonant frequencies of the crystal, the so-called Faust-Henry coefficient C, which represents the ratio of the contributions from the electronic (of magnitude d_E) and the ionic parts of the susceptibility, is taken to be a frequency-independent constant. Notably, the nonlinear coefficient goes to zero at about 7.5 THz for GaP due to the cancellation of its ionic and electronic contributions. Table 2.1 quantifies each of these material constants for GaP and also zinc telluride (ZnTe), both of which have a zinc-blende crystal structure. A more recent experiment performed by Leitenstorfer *et al.* on the response of electro-optic crystals to THz light supplies the tabulated values for ZnTe [63, 64].

Underlying eq. 2.25 is the fact that, for a non-vanishing dielectric function, electromagnetic plane waves couple only to transverse vibrational modes. This statement simply follows from plugging our plane wave solutions (eq. 2.17) into Gauss's law (eq. 2.4) for a source-free medium:

$$0 = \nabla \cdot \vec{\boldsymbol{D}} = \nabla \cdot (\epsilon \vec{\boldsymbol{E}}) = \epsilon \vec{\boldsymbol{k}} \cdot \vec{\boldsymbol{E}}, \tag{2.26}$$

which indicates the orthogonality between the wave-vector $\vec{\boldsymbol{k}}$ and the field $\vec{\boldsymbol{E}}$ for a homogeneous dielectric function ϵ.

Table 2.1: Material constants used to calculate the $\chi^{(2)}(\Omega)$ susceptibility of the zinc-blende crystals GaP and ZnTe in the THz regime.

Crystal	d_E (pm/V)	C	Ω_{TO} (THz)	Γ_{TO} (THz)
GaP	1.00	−0.47	10.89	0.02
ZnTe	4.25	−0.07	5.32	0.09

2.2.2 Optimizing the Orientation of Zinc-Blende Crystals for Optical Rectification

The tensorial nature of the second-order susceptibility adds another dimension to the story beyond the frequency dependence identified in Section 2.2.1. Here we lay out a rigorous procedure that addresses the dependence of optical rectification on the polarization of the incident NIR pump field. The nonlinear medium of choice is a (110)-oriented zinc-blende crystal. Since zinc-blende crystals belong to the cubic $\bar{4}$3m crystal class, the spatial indices corresponding to non-zero elements of the $\vec{\vec{\chi}}^{(2)}$ susceptibility tensor satisfy the rule $i \neq j \neq k$. This condition allows the tensor to be written in contracted notation as prescribed by Table 2.2. Furthermore, the high degree of symmetry of these crystals reduces the nonlinear tensor to only one non-zero independent coefficient $\chi^{(2)}_{41} = \chi^{(2)}_{52} = \chi^{(2)}_{63} \equiv \chi^{(2)}$ [26]. Then, from equation 2.24, the nonlinear polarization vector for optical rectification can be expressed as an integral over all frequency space:

$$\begin{pmatrix} \tilde{P}_i^{(2)'}(z,\Omega) \\ \tilde{P}_j^{(2)'}(z,\Omega) \\ \tilde{P}_k^{(2)'}(z,\Omega) \end{pmatrix} = 2\epsilon_0 \chi^{(2)}(\Omega) \int_0^\infty \begin{pmatrix} \tilde{E}'_j(z,\omega+\Omega)\tilde{E}'_k(z,-\omega) + \tilde{E}'_k(z,\omega+\Omega)\tilde{E}'_j(z,-\omega) \\ \tilde{E}'_i(z,\omega+\Omega)\tilde{E}'_k(z,-\omega) + \tilde{E}'_k(z,\omega+\Omega)\tilde{E}'_i(z,-\omega) \\ \tilde{E}'_i(z,\omega+\Omega)\tilde{E}'_j(z,-\omega) + \tilde{E}'_j(z,\omega+\Omega)\tilde{E}'_i(z,-\omega) \end{pmatrix} \mathrm{d}\omega. \tag{2.27}$$

By the reality of the fields, $\tilde{E}(z,-\omega) = \tilde{E}(z,\omega)^*$ where the asterisk denotes the complex conjugate operation. Equation 2.27 orients the polarization vector in the crystallographic axes $\{ijk\}$ of the zinc-blende medium, as indicated by the primed notation. Note that since the nonlinear optical wave equation given by eq. 2.19 is situated in the coordinates $\{xyz\}$ of the laboratory reference frame, a coordinate transformation of eq. 2.27 is required before it can be used. As before, the z-axis defines the direction of light propagation and is pointed along the [110] Miller direction, out of the plane of the page in Figure 2.3. The azimuthal angles ϕ and θ are respective of the linear polarizations of the THz and NIR electric fields taken with respect to the [001]-axis of the crystal, parallel to which the x-axis is defined.

This coordinate transformation has been well developed in Ref. [66] which specifies

Table 2.2: Prescription for contracting the notation $\chi^{(2)}_{ijk}$ to $\chi^{(2)}_{mk}$.

m	1	2	3	4	5	6
ij	11	22	33	32, 23	31, 13	12, 21

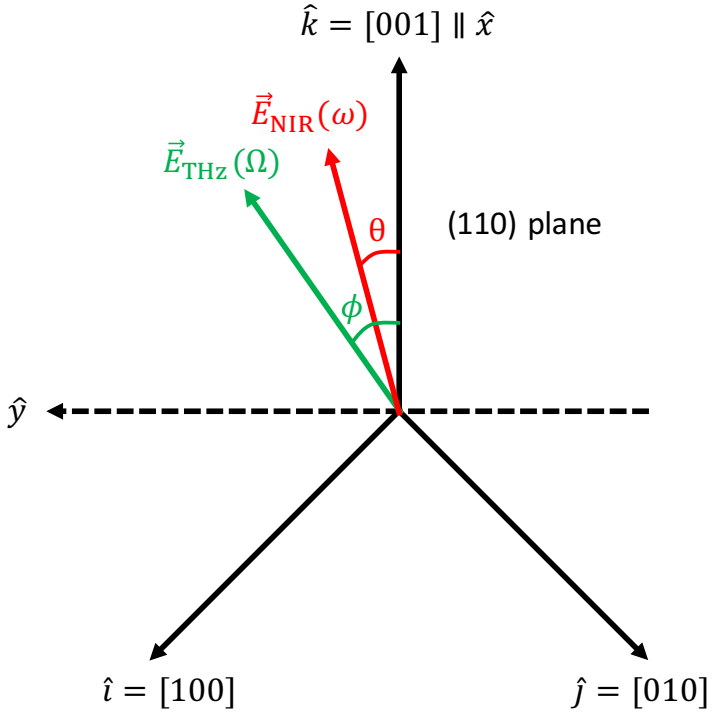

Figure 2.3: Orientation of the NIR and THz electric field vectors with respect to the geometry of the (110)-oriented zinc-blende crystal. Adapted from [65].

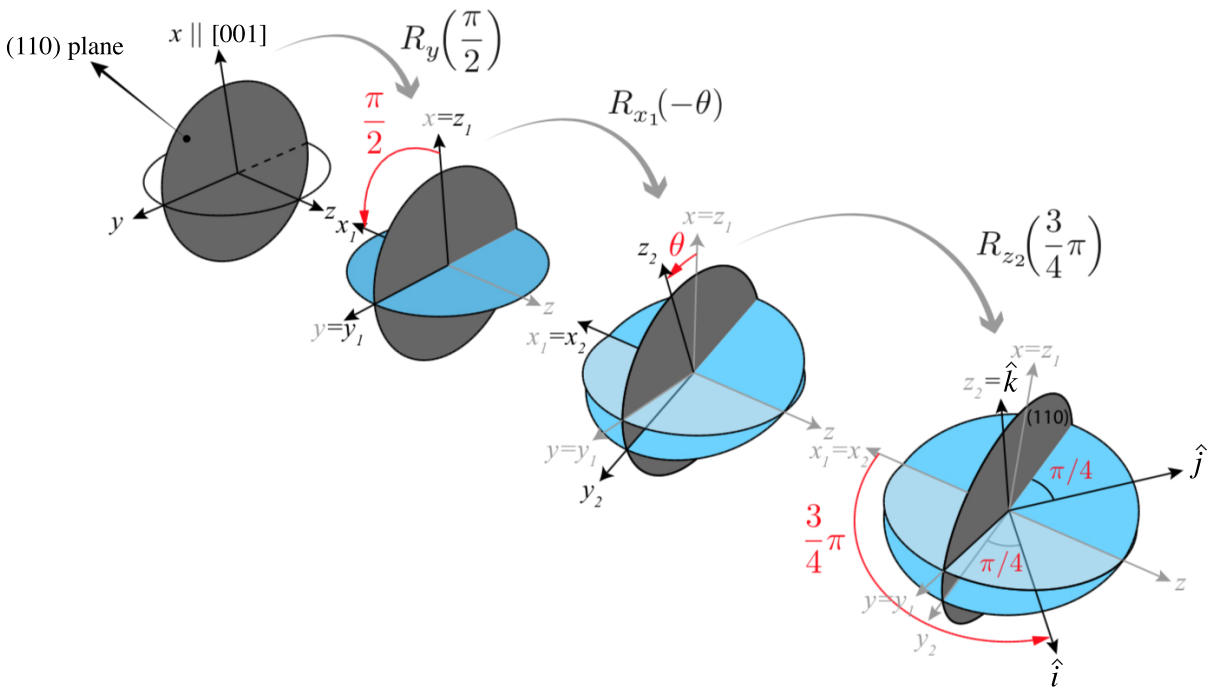

Figure 2.4: Illustration of the set of rotations required to transform between laboratory and crystallographic axes for a (110)-oriented zinc-blende crystal. Adapted from [66].

the series of rotations needed to be performed on an incident electric field polarized, for example, along the x-axis, as in:

$$\vec{\boldsymbol{E}}_{\text{inc}}(z,\omega) = \tilde{E}_0(z,\omega)\begin{pmatrix}1\\0\\0\end{pmatrix}. \tag{2.28}$$

The naught subscript indicates a field component belonging to the NIR pulse. As shown in Figure 2.4, we require the following rotation operators where the subscript indicates the axis of rotation [67]:

$$R_x(\theta) = \begin{bmatrix}1 & 0 & 0\\ 0 & \cos(\theta) & \sin(\theta)\\ 0 & -\sin(\theta) & \cos(\theta)\end{bmatrix} \tag{2.29}$$

$$R_y(\theta) = \begin{bmatrix}\cos(\theta) & 0 & -\sin(\theta)\\ 0 & 1 & 0\\ \sin(\theta) & 0 & \cos(\theta)\end{bmatrix} \tag{2.30}$$

$$R_z(\theta) = \begin{bmatrix}\cos(\theta) & \sin(\theta) & 0\\ -\sin(\theta) & \cos(\theta) & 0\\ 0 & 0 & 1\end{bmatrix}. \tag{2.31}$$

The coordinate transform $\underline{\underline{M}}^{(110)}$ that brings vectors from the laboratory frame into the crystallographic axes and its inverse are defined by the following sets of rotations:

$$\underline{\underline{M}}^{(110)} \equiv R_{z_2}\Big(\frac{3}{4}\pi\Big)R_{x_1}(-\theta)R_y(\pi/2) \tag{2.32}$$

$$(\underline{\underline{M}}^{(110)})^{-1} \equiv R_y(-\pi/2)R_{x_1}(\theta)R_{z_2}\Big(-\frac{3}{4}\pi\Big). \tag{2.33}$$

In defining the rotation about the x_1-axis, the angle θ generalizes the polarization of the NIR electric field within the (110) crystal plane. In the crystal frame, the incident electric field is:

$$\vec{\boldsymbol{E}}'_{\text{inc}}(z,\omega) = \underline{\underline{M}}^{(110)}\vec{\boldsymbol{E}}_{\text{inc}}(z,\omega) = \tilde{E}_0(z,\omega)\begin{pmatrix}-\sin(\theta)/\sqrt{2}\\ \sin(\theta)/\sqrt{2}\\ -\cos(\theta)\end{pmatrix}. \tag{2.34}$$

Plugging this form of the NIR field into eq. 2.27 gives:

$$\vec{\boldsymbol{P}}^{(2)'}(z,\Omega) = 2\epsilon_0\chi^{(2)}(\Omega)\int_0^\infty \tilde{E}_0(z,\omega+\Omega)\tilde{E}_0(z,-\omega)\begin{pmatrix}\sqrt{2}\cos(\theta)\sin(\theta)\\ -\sqrt{2}\cos(\theta)\sin(\theta)\\ -\sin^2(\theta)\end{pmatrix}\mathrm{d}\omega. \tag{2.35}$$

Transforming back to the laboratory frame requires the inverse transform, leading to:

$$\vec{\boldsymbol{P}}^{(2)}(z,\Omega) = (\underline{\underline{M}}^{(110)})^{-1}\vec{\boldsymbol{P}}^{(2)'}(z,\Omega) \tag{2.36}$$

$$= 2\epsilon_0\chi^{(2)}(\Omega)\int_0^\infty \tilde{E}_0(z,\omega+\Omega)\tilde{E}_0(z,-\omega)\begin{pmatrix}-3\cos(\theta)\sin^2(\theta)\\ 2\cos^2(\theta)\sin(\theta)-\sin^3(\theta)\\ 0\end{pmatrix}\mathrm{d}\omega. \tag{2.37}$$

From eq. 2.37, we can work out the angle θ of NIR polarized light that maximizes the optical rectification process for our (110)-oriented crystal. Using eq. 2.19, we know that

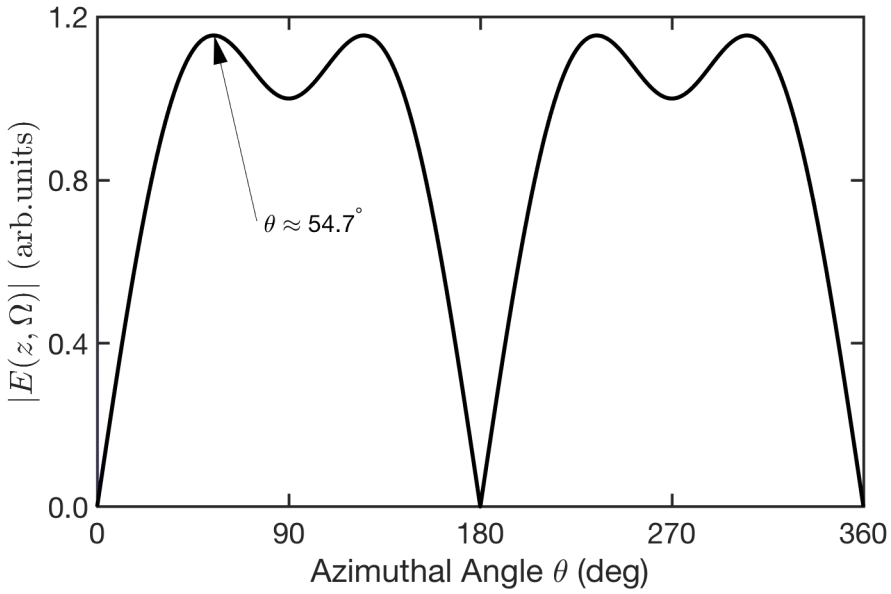

Figure 2.5: Dependence of the magnitude of the THz field on the azimuthal angle of the NIR field.

the magnitude of the THz field evolves in proportion to the nonlinear polarization as [65]:

$$\begin{aligned} \left|\vec{\boldsymbol{E}}(z,\Omega)\right| &\propto \left|\vec{\boldsymbol{P}}^{(2)}(z,\Omega)\right| \\ &\propto \sqrt{\left(\tilde{P}_x^{(2)}(z,\Omega)\right)^2 + \left(\tilde{P}_y^{(2)}(z,\Omega)\right)^2} \\ &\propto \sqrt{-3\left(\sin^2(\theta) - \frac{2}{3}\right) + \frac{4}{3}}. \end{aligned} \tag{2.38}$$

Therefore, the maximum THz field output by optical rectification occurs for $\sin^2(\theta) = 2/3 \rightarrow \theta \approx 54.7^{\circ}$ [65]. Figure 2.5 plots equation 2.38 as a function of the NIR azimuthal angle. Furthermore, the linear polarization of the THz field can be predicted:

$$\tan(\phi) \equiv \frac{\tilde{P}_y^{(2)}}{\tilde{P}_x^{(2)}} = \frac{2\cos^2(\theta)\sin(\theta) - \sin^3(\theta)}{-3\cos(\theta)\sin^2(\theta)}, \tag{2.39}$$

recalling the definition of ϕ shown in Fig. 2.5. Equation 2.39 states that the polarization of the generated THz field can be controlled via the relative orientation of the zinc-blende medium and the NIR field vector. The maximal angle $\theta = 54.7^{\circ}$ gives $\phi = 0^{\circ}$, corresponding to a (vertically) polarized THz field vector aligned along the x-axis.

Hereafter we assume that the polarization of the NIR pump pulses has been optimized so as to maximize the magnitude of the generated THz light. From equation 2.38, the angular dependence can be replaced simply by a factor of $\sqrt{4/3}$ under this condition. Our main concern becomes the shape of the THz frequency spectrum generated by optical rectification. Now that we have obtained the proper form of the induced nonlinear polarization as in eq. 2.37, we can plug it into eq. 2.19 and obtain a first-order differential equation that

is one dimensional in the propagation coordinate:

$$\frac{\partial}{\partial z}\tilde{E}(z,\Omega) = \frac{2i\Omega\chi^{(2)}(\Omega)}{\tilde{n}(\Omega)c}\sqrt{\frac{4}{3}}\int_0^\infty \tilde{E}_0(z,\omega+\Omega)\tilde{E}_0(z,-\omega)\ \mathrm{d}\omega. \tag{2.40}$$

2.2.3 Material Dispersion of Zinc-Blende Crystals

Our derivation of equation 2.40 showed how a second-order nonlinearity can be used to couple NIR field components for the purpose of generating THz light. It is worthwhile to detail how the short NIR pulse travels through the nonlinear medium to seed this interaction. Since two NIR components are needed to produce each THz component, we consider the motion of the NIR pulse as a whole as opposed to its individual components. Being that a short pulse is simply the coherent superposition of many individual frequency components, the NIR pulse propagates with a group velocity $v_\mathrm{g} \equiv c/n_g$, defined by the group refractive index n_g of the medium. The polarization that develops through optical rectification varies with the pulse and thus also evolves with this group velocity. Meanwhile, the THz wave generated by the nonlinear polarization travels through the medium at the phase velocity $v_\mathrm{ph}(\Omega) \equiv c/n(\Omega)$. For the generation process to be efficient, the THz light produced at the entrance of the medium should remain in phase with that generated through to the exit. In other words, the phase velocity of the THz component must match the NIR group velocity for its efficient generation:

$$v_\mathrm{ph}(\Omega) = v_\mathrm{g}(\lambda_0). \tag{2.41}$$

This equality should hold, at least approximately, for as many THz frequencies as possible in order to maximize the spectral bandwidth of the generated THz radiation. However, due to the additional refractive index from phonon modes at THz frequencies, most electro-optic crystals have a greater THz refractive index $n_\mathrm{THz}(\Omega)$ than their NIR group index n_g and so the NIR pulse moves faster than the THz waves they generate. This is also a challenge for THz detection, as we will see in Section 2.3.3, where a NIR pulse can be used to sample the local oscillation of the THz field.

In eq. 2.17, we expressed our field components as a complex amplitude multiplied by an exponential phase factor whose argument contained a frequency-dependent complex wave-vector $\tilde{k}(\omega)$. With this in mind, eq. 2.41 can be more generally understood by analyzing the phase evolution of each of the waves participating in the nonlinear process. Actually, eq. 2.41 corresponds to a special case where all of the involved waves propagate collinearly. Alternative non-collinear generation schemes are in widespread use for their ability to produce some of the strongest and highest energy THz pulses to date [33, 30], but their specifics are beyond the scope of this work. Important to both types, however, is exploitation of the dispersive properties of the medium to achieve high efficiency through phase-matching between the NIR and THz fields.

For the semiconductors considered in this thesis, dispersion is caused mainly by infrared-active lattice resonances that lie in the THz range as well as band-gap resonances in the visible. In particular, the zinc-blende crystal zinc telluride (ZnTe) has a direct band-gap energy of about 2.26 eV, or roughly 550 nm [68]. Similarly, the gallium phosphide (GaP) crystal belongs to the same crystal class with an indirect band-gap of 2.27 eV while its direct band-gap is about 2.79 eV [68]. To quantify the dielectric response of our chosen media, we turn to empirical models derived in the literature from classical dispersion theory

in which the atoms are treated as damped harmonic oscillators forced to oscillate by an optical field. For the ZnTe crystal, the complex dielectric response has been structured via the Lorentz model as [69]:

$$\tilde{\epsilon}(\Omega) = \epsilon_{\text{el}} + \frac{\epsilon_{\text{str}}\Omega_{\text{TO}}^2}{\Omega_{\text{TO}}^2 - \Omega^2 - 2i\Gamma_{\text{TO}}\Omega}, \tag{2.42}$$

where the first term, $\epsilon_{\text{el}} \equiv \epsilon(\Omega \to \infty)$, is largely due to the electronic response of the medium at high frequencies while the second term accounts for the response of the ions with $\epsilon_{\text{str}} \equiv \epsilon(\Omega = \Omega_{\text{TO}})$ describing the strength of the lattice resonance. Equation 2.42 can be broken up into its real and imaginary constituents as:

$$\tilde{\epsilon}(\Omega) = \mathbb{R}[\tilde{\epsilon}(\Omega)] + i\,\mathbb{I}[\tilde{\epsilon}(\Omega)] \tag{2.43}$$

$$\equiv \tilde{n}^2(\Omega) = \big(n(\Omega) + i\kappa(\Omega)\big)^2, \tag{2.44}$$

where $\mathbb{R}$ takes the real part and the $\mathbb{I}$ operator takes the imaginary part. The frequency-dependent real and imaginary parts of the complex refractive index $\tilde{n}(\Omega)$ are $n(\Omega)$, the refractive index, and $\kappa(\Omega)$, the extinction coefficient. These quantities can be shown to relate to the complex dielectric function via:

$$n(\Omega) = \mathbb{R}[\sqrt{\tilde{\epsilon}(\Omega)}] \equiv \sqrt{\frac{|\tilde{\epsilon}(\Omega)| + \mathbb{R}[\tilde{\epsilon}(\Omega)]}{2}} \tag{2.45}$$

$$\kappa(\Omega) = \mathbb{I}[\sqrt{\tilde{\epsilon}(\Omega)}] \equiv \sqrt{\frac{|\tilde{\epsilon}(\Omega)| - \mathbb{R}[\tilde{\epsilon}(\Omega)]}{2}}. \tag{2.46}$$

The extinction coefficient is related to the power absorption coefficient, as defined by Beer's law $I(z) = I_0\ \mathrm{e}^{-\alpha z}$, by:

$$\alpha(\Omega) = \frac{2\kappa(\Omega)\Omega}{c}. \tag{2.47}$$

Table 2.3 lists each of the material properties for our chosen models for GaP and ZnTe at room temperature (300 K). The spectral range over which the experiment was performed by Gallot *et al.* on ZnTe extended from 0.3 to 4.5 THz [69]. They found that the refractive index was predominantly determined by the TO phonon resonance at 5.32 THz. On the other hand, their experiment was also sensitive to the absorptive strength of two other higher-order phonon resonances at 1.6 and 3.7 THz which they found to limit their accessible frequency range. Jepsen *et al.* explored the temperature dependence of these resonances and attributed these features to two-phonon processes [70]. We will discuss these features more in Chapter 4 when we present our own empirical data. The currently accepted model for the NIR refractive index of ZnTe is given by a Sellmeier equation [71]:

$$n(\lambda) = \sqrt{A_{\text{ZnTe}} + \frac{B_{\text{ZnTe}}}{\lambda^2 - C_{\text{ZnTe}}}}, \tag{2.48}$$

where the wavelength λ is specified in microns.

For the GaP crystal, Parsons and Coleman have empirically verified Barker's classical model of the dielectric response in which a frequency-dependent damping factor was introduced [72, 73]:

$$\tilde{\epsilon}(\Omega) = 1 + \sum_{a=1}^{3} \frac{S_{ea}\Omega_{ea}^2}{\Omega_{ea}^2 - \Omega^2} + \frac{S_{\text{TO}}\Omega_{\text{TO}}^2\big(1 - \sum_{b=1}^{2} S_{lb}\big)}{\big(\Omega_{\text{TO}}^2 - \Omega^2 - i\Omega\Gamma_{\text{TO}}\big) - \Omega_{\text{TO}}^2 \sum_{b=1}^{2} \frac{S_{lb}\Omega_{lb}^2}{\Omega_{lb}^2 - \Omega^2 - i\Omega\Gamma_{lb}}}, \tag{2.49}$$

Table 2.3: Material properties from literature models for the complex dielectric functions of GaP and ZnTe.

(a) ZnTe [69, 71]

ϵ_{el}	7.44	
ϵ_{str}	2.58	
$\Omega_{\text{TO}}/2\pi$	5.32	THz
$\Gamma_{\text{TO}}/2\pi$	0.025	THz
A_{ZnTe}	4.27	
B_{ZnTe}	3.01	μm^2
C_{ZnTe}	0.142	μm^2

(b) GaP [72]

S_{e1}	2.570		S_{TO}	2.056	
$\Omega_{e1}/2\pi$	29,000	cm^{-1}	$\Omega_{\text{TO}}/2\pi$	363.4	cm^{-1}
S_{e2}	4.131		$\Gamma_{\text{TO}}/2\pi$	1.1	cm^{-1}
$\Omega_{e2}/2\pi$	42,700	cm^{-1}	S_{l1}	7.0	$\times 10^{-4}$
S_{e3}	1.390		$\Omega_{l1}/2\pi$	349.4	cm^{-1}
$\Omega_{e3}/2\pi$	58,000	cm^{-1}	$\Gamma_{l1}/2\pi$	21	cm^{-1}
			S_{l2}	3.5	$\times 10^{-4}$
			$\Omega_{l2}/2\pi$	358.4	cm^{-1}
			$\Gamma_{l2}/2\pi$	12.6	cm^{-1}

where S_e and S_l respectively denote an electronic or ionic oscillator strength corresponding to angular frequencies Ω_e and Ω_l with ionic damping factors Γ_l and TO oscillator strength S_{TO}. Using data in the NIR from Ref. [74], the authors used this model to update the established values for the refractive index extending all the way from the microwave to visible frequencies.

In Fig. 2.6, the left axes show the real refractive indices in the THz range compared to their respective group index at $\lambda_0 = 1035$ nm [72, 69, 71]. This wavelength is chosen since it is the central wavelength of our laser, as presented in Chapter 3. The right axes plot the amplitude absorption coefficients over the same frequency range. For either crystal, the lattice resonances near 5.32 THz (ZnTe) and 10.89 THz (GaP) are due to the presence of their lowest transverse optical phonons at $\Omega = \Omega_{\text{TO}}$. Finally, the following dimensional analysis can be used to convert between frequencies stated in units of inverse centimetres and THz frequencies:

$$f(\text{cm}^{-1}) \equiv \frac{f(\text{THz})}{c(\text{cm/ps})}, \tag{2.50}$$

where c is the speed of light in vacuum.

2.2.4 Phase-Matching

Due to material dispersion, the NIR pump pulse stays in phase with the THz waves it generates only for so long. Therefore, we designate a length over which they stay coherent. This so-called coherence length is defined as the distance over which generation of the THz waves remains entirely constructive. In other words, the distance at which they are produced out of phase by π radians marks the onset of destructive interference [75]:

$$L_{\text{coh}} \equiv \frac{\pi}{\mathbb{R}[\Delta\tilde{k}]} \approx \frac{\pi c}{|n_{\text{g}}(\lambda_0) - n(\Omega)|}, \tag{2.51}$$

where the NIR group index, $n_{\text{g}}(\lambda_0) \equiv n(\lambda_0) - \lambda_0 \frac{\partial n(\lambda)}{\partial \lambda}|_{\lambda=\lambda_0}$, is evaluated at the central wavelength of the pulse provided that the spectral bandwidth of the pump pulse is small enough to assume $\Delta\omega \ll \omega_0 = 2\pi c/\lambda_0$. The complex wave-vector mismatch $\Delta\tilde{k}$ between the three waves mixing in collinear optical rectification is:

$$\Delta\tilde{k}(\omega, \Omega) = \tilde{k}(\omega + \Omega) - \tilde{k}(\omega) - \tilde{k}(\Omega). \tag{2.52}$$

Figure 2.6: Real part of the refractive index and amplitude absorption coefficient of zinc-blende semiconductors in the THz range: (a) GaP [72]; (b) ZnTe [69]. The labelled dashed lines indicate the value of the group index at 1035 nm.

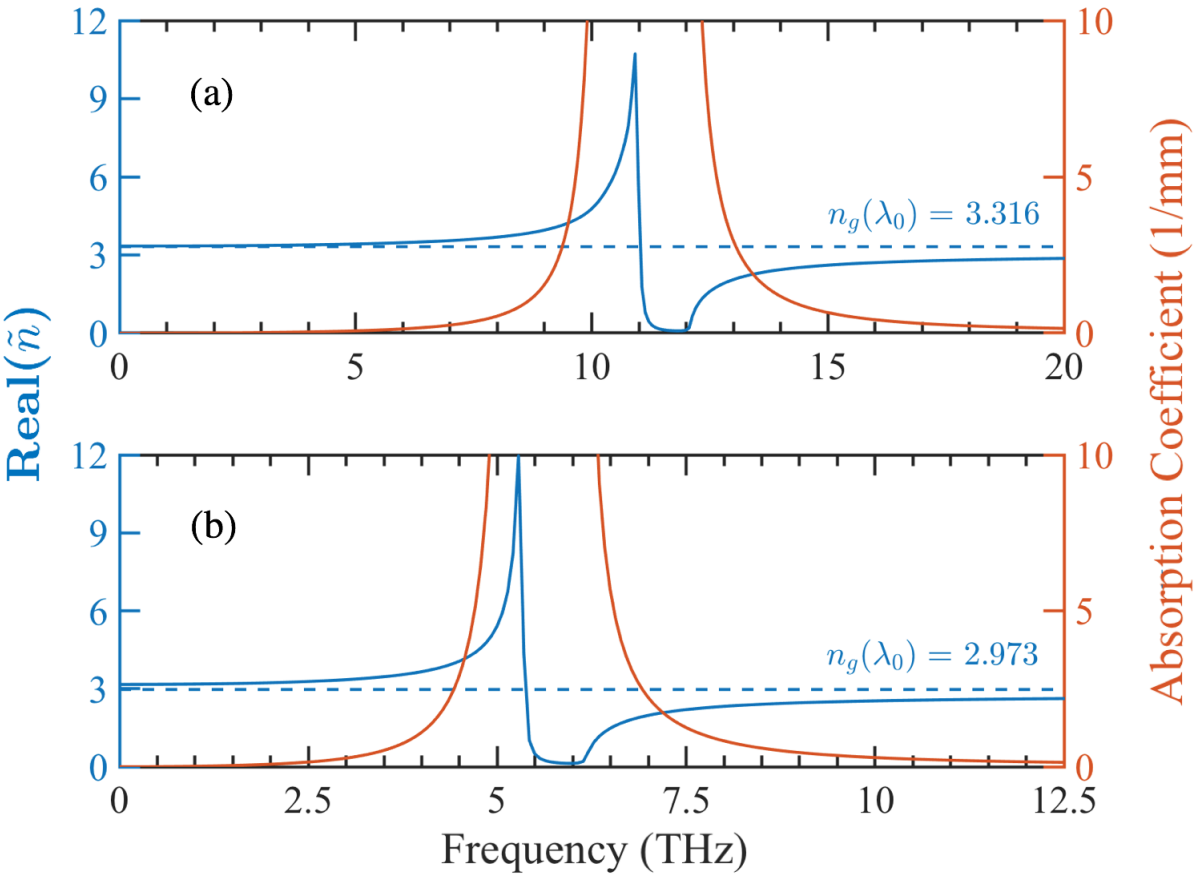

Equation 2.52 shows that any phase common to the NIR components will be cancelled by the subtractive process. For example, the carrier-envelope phase (CEP) between the central carrier frequency and the position of the intensity envelope of the short pulse is common to all of the frequencies in a pulse. Therefore, the nonlinear process of difference frequency mixing passively produces CEP-stable THz pulses [76]. Perfect phase-matching occurs when $\Delta\tilde{k} = 0$.

We now show how the coherence length finds use in estimating the effects of phase mismatch by following its derivation from our equations. First, eq. 2.40 is solved by performing the integral of both sides over the spatial coordinate. The limits of integration extend over the thickness of the medium L, starting at the entrance to the medium at $z = 0$. If there are no THz waves at the input, then imposing the boundary condition $\tilde{E}(z = 0, \Omega) = 0$ leads to a solution at the exit of the medium:

$$\tilde{E}(z = L, \Omega) = \frac{2i\Omega\chi^{(2)}(\Omega)}{\tilde{n}(\Omega)c}\sqrt{\frac{4}{3}}\int_0^\infty \mathrm{d}\omega\left\{\int_0^L \tilde{E}_0(z, \omega + \Omega)\tilde{E}_0(z, -\omega)\ \mathrm{d}z\right\}. \tag{2.53}$$

Plugging in our amplitude-modulated plane wave solutions from eq. 2.17 allows us to develop the phase-matching integral in the curly brackets:

$$\int_0^L \tilde{E}_0(z, \omega + \Omega)\tilde{E}_0(z, -\omega)\ \mathrm{d}z = \int_0^L \tilde{A}_0(z, \omega + \Omega)\ \mathrm{e}^{i\tilde{k}(\omega+\Omega)z}\tilde{A}_0(z, -\omega)\ \mathrm{e}^{-i\tilde{k}(\omega)z}\ \mathrm{d}z. \tag{2.54}$$

If the NIR spectral amplitudes do not change significantly longitudinally, phase mismatch affects the amplitude of the THz wave at the output according to:

$$\tilde{A}(L, \Omega) \propto \tilde{A}_0(\omega + \Omega)\tilde{A}_0(-\omega)\int_0^L \mathrm{e}^{i\Delta\tilde{k}(\omega,\Omega)z}\ \mathrm{d}z. \tag{2.55}$$

Solving the phase-matching integral:

$$\begin{aligned}\int_0^L \mathrm{e}^{i\Delta\tilde{k}(\omega,\Omega)z}\ \mathrm{d}z &= \frac{\mathrm{e}^{i\Delta\tilde{k}(\omega,\Omega)L} - 1}{i\Delta\tilde{k}(\omega, \Omega)} \\ &= \mathrm{sinc}(x)\ L\ \mathrm{e}^{ix},\end{aligned} \tag{2.56}$$

where $x \equiv \Delta\tilde{k}L/2$. Therefore, we arrive at a solution for the complex amplitude spectrum of the THz field produced from optical rectification through a nonlinear medium of thickness L, neglecting the effects of multi-photon absorption or free-carrier absorption:

$$\tilde{A}(L, \Omega) = \frac{2i\Omega\chi^{(2)}(\Omega)L}{\tilde{n}(\Omega)c}\sqrt{\frac{4}{3}}\int_0^\infty \tilde{A}_0(\omega + \Omega)\tilde{A}_0(-\omega)\,\mathrm{sinc}(x(\omega, \Omega))\ \mathrm{e}^{ix(\omega,\Omega)}\ \mathrm{d}\omega. \tag{2.57}$$

The inset of Fig. 2.7 shows that the zeros of the symmetric $\mathrm{sinc}(x)$ function occur at $\mathbb{R}[x] = \pm N\pi$ for non-zero integer N. Since lengths are positive quantities, we focus on the positive values and note in particular that the first zero corresponds to the distance at which the generation process is completely cancelled by destructive interference. From eq. 2.51, this distance is twice our definition of the coherence length. Therefore, the first zero of the $\mathrm{sinc}(x)$ function marks the lowest-frequency minimum in the generated spectrum above zero frequency. That is, we always expect the first minimum to occur at zero frequency (which we will call DC) because static fields do not propagate, as seen by setting $\Omega = 0$ in

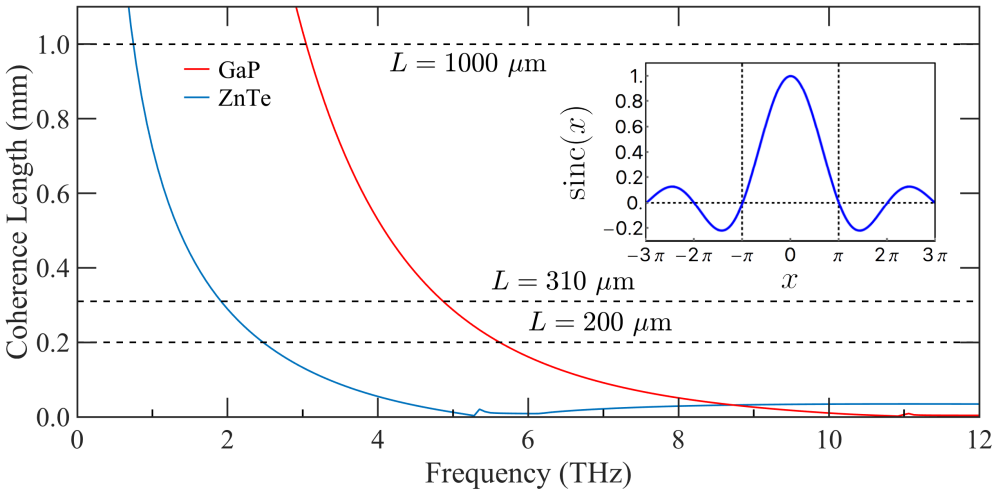

Figure 2.7: Coherence lengths of GaP and ZnTe pumped by light centred at 1035 nm. Dashed lines indicate the thickness of various crystals we have in the laboratory. The inset shows the sinc(x) term from the phase-matching integral in eq. 2.56.

eq. 2.57. For a nonlinear medium of thickness L, we expect the phase-matched bandwidth to extend from DC up to the lowest frequency satisfying the condition $L = 2L_{\text{coh}}$. The frequency space afterwards will suffer from destructive interference until the next highest minimum, after which the cycle repeats anew.

For our choice of a NIR pump centred at 1035 nm, Figure 2.7 overlays the coherence lengths for GaP and ZnTe along with crystals of various thickness. The greater mismatch in ZnTe between the THz and NIR refractive indices as compared to GaP, as seen in Fig. 2.6, leads to faster decoherence which produces smaller coherence lengths. Using the relation $L = 2L_{\text{coh}}$, the resulting phase-matching bandwidth of the 200 μm thick ZnTe crystal, for example, extends up to about 3.4 THz while that of a GaP crystal of equal length is about double at 6.8 THz. The modelled coherence length for GaP at 4 THz is about 530 μm, so use of the twice-as-long 1000 μm thick crystal should display its first minimum in the generated spectrum at about 4 THz. Additionally, the 310 μm thick GaP crystal should have its minimum at around 6 THz for which the coherence length is about 160 μm. Finally, since the largest index mismatch occurs for frequencies close to phonon resonances, they display the smallest coherence lengths and can therefore go through many cycles of constructive and destructive interference in thicker crystals.

In general, this method of estimating the spectral extent of the generated THz spectrum leads to a few major predictions based on phase-matching arguments. First, for the same crystal thickness, the lower overall dispersion of GaP promises generation of broader spectra than that from ZnTe. Second, regardless of crystal type, the generated spectrum will narrow with increasing thickness.

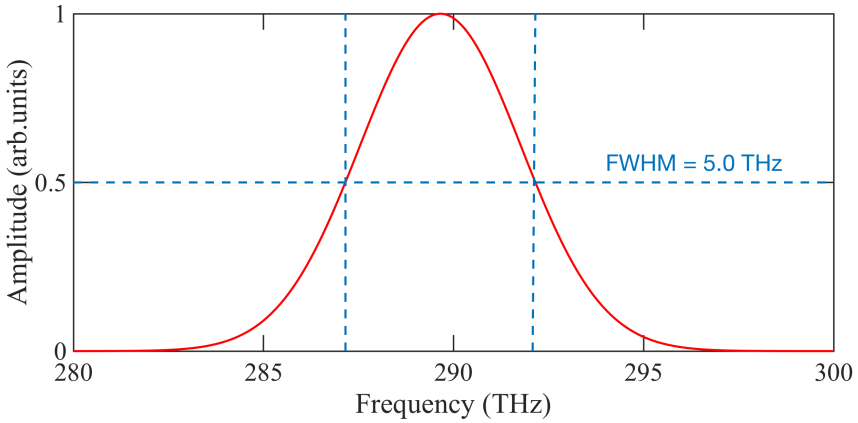

Figure 2.8: Simulated amplitude spectrum of a NIR pulse using a Gaussian profile that is centred at about 290 THz (or 1035 nm) and given a FWHM bandwidth of 5.0 THz.

2.2.5 Tradeoff between Thickness and Spectral Bandwidth

The theoretical predictions laid out in the previous section suggest a much closer look at the role played by the thickness of the medium L in optical rectification. Each term in the phase-matching integral given by eq. 2.56 depends on the thickness which stresses its important yet non-intuitive influence. Previously, we focused our attention only on the sinc(x) term derived from the phase-matching integral and constructed a method based on the coherence length to estimate minima in the generated THz spectrum. Here we present a more complete picture by implementing numerically using MATLAB our analytical solution to the nonlinear optical wave equation for optical rectification given by eq. 2.57. We utilize the chosen models of material dispersion from the literature presented in Sect. 2.2.3. In order to find the expected shape of the generated THz spectrum, we keep the assumption that our zinc-blende media have been oriented optimally to produce maximum signal as described in Sect. 2.2.2. Another input to the code is the amplitude spectrum of the NIR pulse, modelled as shown in Fig. 2.8 by a simple Gaussian envelope defined by:

$$A_0(\omega) = \mathrm{e}^{-(\omega-\omega_0)^2/2\sigma^2}, \tag{2.58}$$

where the half-width at 1/e-intensity σ is related to the full-width at half-maximum (FWHM) in amplitude σ_{FWHM} via:

$$\sigma = \frac{\sigma_{\mathrm{FWHM}}}{2\sqrt{2\ln(2)}}. \tag{2.59}$$

For our analysis, we emulate the spectrum of our laser by centring it on about 290 THz (or 1035 nm) and fixing its FWHM bandwidth to 5.0 THz in amplitude. This choice of bandwidth sets a rough upper limit to the difference frequency mixing that is below the reststrahlen bands of ZnTe and GaP. Additionally, the empirical data that supports the chosen models for the refractive indices only extend at most up to 5 THz due to experimental limitations.

Figures 2.9 and 2.10 plot the resulting spectra calculated using either GaP or ZnTe crystals of various but equivalent thicknesses, normalized to the peak signal produced from the largest thickness of 2 mm. The curves are related by halving the thickness of the nonlinear medium all the way down to 250 μm. Immediately, we see that the better

phase-matching provided by GaP crystals produces broader spectra than those generated from equally-thick ZnTe crystals. In particular, a 2 mm crystal has its phase-matched bandwidth extend up to about 3.0 THz for GaP as opposed to 0.75 THz for ZnTe. These results support our expectation that broader spectra are generated by crystals with higher frequency TO phonon resonances. For GaP, the TO phonon resonance occurs at about 11 THz and this relatively high value leads to flatter dispersion at low THz frequencies than for ZnTe. This property allows these low frequencies to stay better phase-matched with our light centred at 1035 nm even through thicker crystals. An important historical milestone in this regard was the first measurement of a 7 THz wide bandwidth using a 150 μm GaP crystal as a detector [77], demonstrating the equivalence between the emission and detection bandwidths of a nonlinear crystal. Generating or detecting THz frequencies beyond about 7.5 THz is difficult due to the zeroing of the nonlinear coefficient through the cancellation of its ionic and electronic contributions, as mentioned in Sect. 2.2.1.

In Figure 2.9, we see that increasing the thickness of a GaP crystal from 0.25 mm to 0.50 mm pushes the lowest-frequency minimum from about 6.4 THz down to 5.2 THz. Recall that in Sect. 2.2.4, we predicted the phase-matching bandwidth of our similar 200 μm thick GaP crystal to extend until 6.8 THz. This agreement supports our phase-matching argument that the relationship $L = 2L_{\text{coh}}$, between the calculated coherence length and the thickness of the medium, can be used to predict the appearance of minima in the generated spectra. The cyclic behaviour of coherence manifests as minima clustering at certain frequencies, such as near 1.3 THz and 3.0 THz for ZnTe, due to our choice of a simple factor-of-two relationship between the thicknesses. For either the GaP or ZnTe crystal, doubling the thickness shows the expected narrowing of the spectra. Finally, the greater phase-mismatch of the ZnTe crystal pumped by 1035 nm light is clearly shown by the greater number of minima appearing in the generated spectra which indicates that more frequencies are going in and out of cycles of coherence.

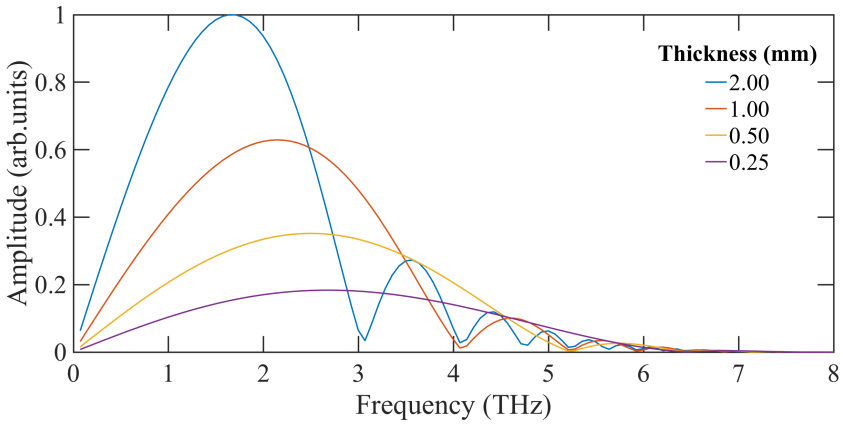

Figure 2.9: Calculated THz emission from (110)-oriented GaP crystals based on input NIR spectrum from Fig. 2.8.

2.3 Electro-Optic Detection

In the previous section, we described how the nonlinear process of optical rectification could be used to convert NIR pulses down to THz frequencies. The next task is to explain

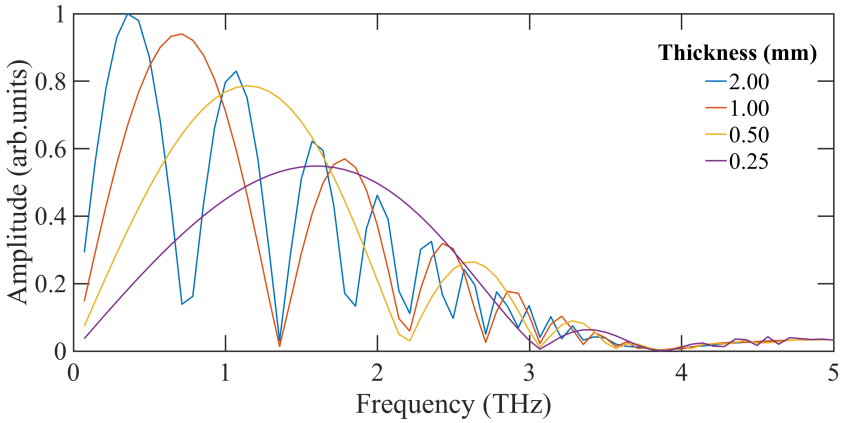

Figure 2.10: Calculated THz emission from (110)-oriented ZnTe crystals based on input NIR spectrum from Fig. 2.8.

their subsequent detection. Interestingly, the fields of these THz pulses oscillate about one hundred times slower than those of the NIR, being practically DC in comparison. In noncentrosymmetric media, like our favoured zinc-blende crystal class, the action of a DC field enables the linear electro-optic "Pockels" effect. This nonlinear effect is usually understood through the ensuing rotation of the index ellipsoid of the medium which induces a birefringence in the NIR range that is, to first order, linearly proportional to the applied electric field. In this section, we show that measurement of this field-sensitive effect is central to our method of detecting pulsed THz radiation.

2.3.1 The Pockels Effect for Short Pulses

In Section 2.2, our refinement of the form of the polarization associated with optical rectification led us to an expression for the electric field of a THz pulse, as given by eq. 2.57. The strategy here, however, is to simply show that the refractive index of a medium with a second-order nonlinearity develops a linear dependence on the applied electric field through the Pockels effect. First, recall that the Fourier component of the electric flux density (eq. 2.8) at an arbitrary frequency ω_m is:

$$D(\omega_m) = \epsilon_0 E(\omega_m) + P^{(1)}(\omega_m) + P^{\mathrm{NL}}(\omega_m) = \epsilon(\omega_m) E(\omega_m), \tag{2.60}$$

where the permittivity of the medium $\epsilon(\omega_m)$ contains both the linear and nonlinear contributions. Let us focus on the nonlinear polarization established at the particular sum frequency $\omega_m = \omega + \Omega$ due to the coherent mixing of only one frequency component at Ω of the THz pulse with an arbitrary NIR ω frequency. For the moment, we apply the scalar approximation to omit tensor indices. From the general form given previously by eq. 2.24, an electro-optic medium displays a second-order nonlinear polarization via the Pockels effect as:

$$P^{(2)}(\omega + \Omega) = 2\epsilon_0 \chi^{(2)}(\omega + \Omega; \omega, \Omega) E(\omega) E(\Omega), \tag{2.61}$$

where the degeneracy factor of 2 accounts for the intrinsic permutation symmetry of the second-order susceptibility tensor. Plugging eq. 2.61 into eq. 2.60 directly gives:

$$\epsilon(\omega + \Omega) E(\omega + \Omega) = \epsilon_0 E(\omega + \Omega) + \epsilon_0 \chi^{(1)} E(\omega + \Omega) + 2\epsilon_0 \chi^{(2)}(\omega + \Omega) E(\omega) E(\Omega). \tag{2.62}$$

The next step is to impose the assumption $\omega+\Omega \approx \omega$ due to the many orders of magnitude between THz and NIR frequencies. As a simple shorthand, we also use this assumption to collapse the notation for the frequency dependence of the second-order susceptibility. Accordingly:

$$\epsilon(\omega) = \epsilon_0\big(1 + \chi^{(1)}(\omega) + 2\chi^{(2)}(\omega)E(\Omega)\big). \tag{2.63}$$

The refractive index of the electro-optic medium is defined through the relative permittivity:

$$n(\omega) \equiv \sqrt{\frac{\epsilon(\omega)}{\epsilon_0}} \approx n_O(\omega) + \frac{\chi^{(2)}(\omega)}{n_O(\omega)}E(\Omega), \tag{2.64}$$

having defined the part of the refractive index in the absence of the THz field as $n_O^2(\omega) = 1 + \chi^{(1)}(\omega)$. This expression was obtained by truncating the binomial expansion to its second term, assuming a weak THz field. Therefore, eq. 2.64 states that the refractive index of the electro-optic medium will change, to first order, in proportion with the electric field of the low-frequency THz pulse. Since the linear electro-optic effect is described by a second-order nonlinearity, it can only occur for noncentrosymmetric media as we found with optical rectification.

2.3.2 Optimizing the Orientation of Zinc-Blende Crystals for Electro-Optic Detection

Dropping the tensor indices of the nonlinear susceptibility in the last section helped us form an intuitive picture of the influence of the Pockels effect on NIR light. In reality, our detection scheme hinges on the relative orientation of the electro-optic medium with respect to the incoming THz and NIR fields. Here we seek to detail the detection of the THz field for the case of a (110)-oriented zinc-blende electro-optic crystal. In general, for an anisotropic medium, eq. 2.60 relates the electric field vector in the medium to the electric flux density by the inverse of the permittivity tensor:

$$E_i(\omega) = \sum_j \Big(\epsilon(\omega)^{-1}\Big)_{ij} D_j(\omega). \tag{2.65}$$

By defining components of the impermeability tensor as $\eta_{ij}(\omega) \equiv \epsilon_0\big(\epsilon(\omega)^{-1}\big)_{ij}$, the energy density stored in the electric field is:

$$\begin{aligned} U = \frac{\vec{E}\cdot\vec{D}}{2} &= \frac{1}{2}\sum_i \Big(\sum_j \frac{\eta_{ij}}{\epsilon_0} D_j \hat{e}_j\Big)\cdot\Big(\sum_k D_k \hat{e}_k\Big) \\ &= \frac{1}{2\epsilon_0}\sum_{ijk} \delta_{ik}\eta_{ij} D_j D_k \\ &= \frac{1}{2\epsilon_0}\sum_{jk} \eta_{kj} D_j D_k. \end{aligned} \tag{2.66}$$

Far from resonance, the permittivity and impermeability tensors lack dispersion and are effectively real and symmetric. Importantly, as we saw for optical rectification in Sect. 2.2.2, we should make careful note of the reference frames in which our equations are expressed.

Figure 2.11 shows the relationship between the Cartesian coordinates of the relevant crystallographic axes, indicated by primed and umprimed notation, and the laboratory reference frame which is given by coordinates with asterisks. By accounting for the necessary coordinate transformations between these axes, we aim to derive an expression for the index ellipsoid of the medium in the NIR range as a function of the perturbative THz field. We will follow the procedure well documented by Refs. [26, 78, 66]. The first step is to define the crystallographic coordinates $x_j(\omega) \equiv D_j(\omega)/\sqrt{2\epsilon_0 U}$, where x_j belong to the set $\{x, y, z\}$ determined by the principal Miller directions. Equation 2.66 may now be expanded as:

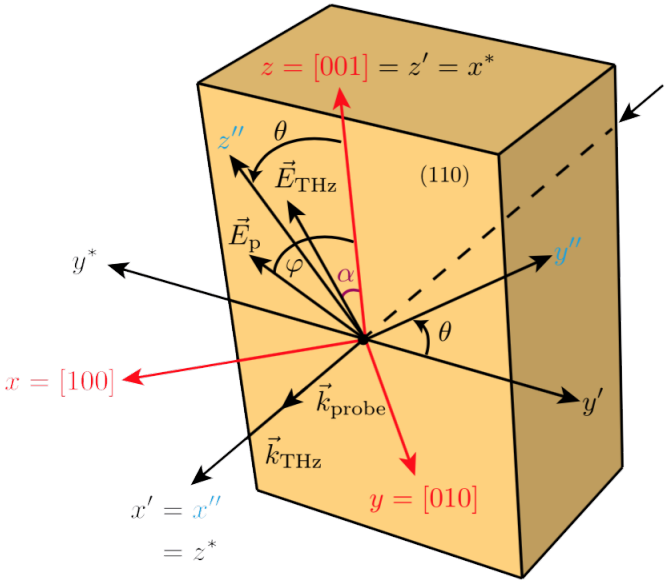

Figure 2.11: Illustration of the electro-optic medium and the relevant Cartesian axes used in deriving the index ellipsoid in the presence of the electric field of a THz pulse. The unprimed axes $\{x, y, z\}$ define the unperturbed crystallographic axes of the crystal. The single-primed axes are simply an intermediate as described in the text. The angle θ rotates these axes into the double-primed axes which correspond to the directions of the crystallographic axes perturbed by the THz field. The angles of the THz and NIR field polarizations are given respectively by α and ψ with respect to the [001] axis of the crystal in the laboratory coordinate frame indicated by the asterisks notation. Adapted from [66].

$$1 = \eta_{xx}x^2 + \eta_{yy}y^2 + \eta_{zz}z^2 + 2(\eta_{xy}xy + \eta_{yz}yz + \eta_{xz}xz). \tag{2.67}$$

To find how an applied field affects the index ellipsoid, we expand the impermeability tensor components in a power series of the field strength:

$$\eta_{ij}(\vec{E}) = \eta_{ij}(\vec{E} = \vec{0}) + \sum_k r_{ijk}E_k + \sum_{k,l} s_{ijkl}E_kE_l + \dots \tag{2.68}$$

where the linear electro-optic coefficients are defined as $r_{ijk} \equiv \frac{\partial \eta_{ij}}{\partial E_k}\big|_{\vec{E}=\vec{0}}$ and the quadratic electro-optic coefficients are $s_{ijkl} \equiv \frac{1}{2}\frac{\partial^2 \eta_{ij}}{\partial E_k \partial E_l}\big|_{\vec{E}=\vec{0}}$. Recall that in Sect. 2.3.1 we found that the Pockels effect led to a change in the refractive index of the medium that was proportional to the field strength. A similar procedure to the higher order finds that the quadratic electro-optic coefficients describe a dependence of the refractive index on the square of the field

strength, also known as the Kerr effect. Since we utilize relatively weak THz fields, however, we truncate eq. 2.68 to the term linear in field strength. The linear electro-optic coefficients inherit the symmetry of the impermeability tensor and, in turn, the nonlinear susceptibility via the relation $\chi^{(2)}_{41}(\omega+\Omega;\omega,\Omega) = -n^4(\omega)r_{41}(\omega+\Omega;\omega,\Omega)/2$ [79, 80]. Since our NIR spectra are centred a wavelength of 1035 nm, far from any resonance, we approximate a flat dispersion of the linear electro-optic coefficients for our crystals. Thus, the ij indices share the contracted notation as prescribed previously in Table 2.2:

$$\eta_m(\vec{E}) = \eta_m(\vec{E}=\vec{0}) + \sum_k r_{mk}E_k + \dots \tag{2.69}$$

Notably, the first term on the right hand side corresponds to the unperturbed refractive indices of the anisotropic medium:

$$\eta_m(\vec{E}=\vec{0}) = \begin{pmatrix} 1/n_1^2 \\ 1/n_2^2 \\ 1/n_3^2 \\ 0 \\ 0 \\ 0 \end{pmatrix}. \tag{2.70}$$

The isotropy of the zinc-blende crystal establishes the equality between the unperturbed refractive indices which we define as $n_1 = n_2 = n_3 \equiv n_O$. Equation 2.67 can now be rewritten in the presence of an applied field $\vec{E}$ as:

$$1 = \frac{1}{n_O^2}(x^2+y^2+z^2) + 2r_{41}\big(E_z xy + E_y xz + E_x yz\big). \tag{2.71}$$

The applied field is the electric field of a THz pulse which evolves as a function of time. Here we consider the instance at time t corresponding to the relative arrival time of the sub-ps long NIR probe within duration of the THz pulse. As shown in Fig. 2.11, the applied field $\vec{E}(t) \equiv \vec{E}_{\mathrm{THz}}(t)$ is linearly-polarized at the angle α in the (110)-plane with respect to the [001] direction having components:

$$\begin{pmatrix} E_x(t) \\ E_y(t) \\ E_z(t) \end{pmatrix} = |\vec{E}_{\mathrm{THz}}(t)| \begin{pmatrix} \sin(\alpha)\cos(45^\circ) \\ \sin(\alpha)\sin(45^\circ) \\ \cos(\alpha) \end{pmatrix}. \tag{2.72}$$

One can make similar coordinate transformation arguments as before in Sect. 2.2.2, therefore using the rotation matrices defined before in eq. 2.30 we find that two coordinate rotations are required to re-express the index ellipsoid given by eq. 2.71 from the crystallographic axes $\{x,y,z\}$ to the principal axes $\{x'',y'',z''\}$ of the perturbed dielectric system. Recall that one more rotation is then needed to obtain the laboratory coordinate frame which we denote by asterisks as $\{x^*,y^*,z^*\}$. The first rotation is by an angle of 45° about the z-axis which aligns the intermediate x'-axis with the direction of propagation:

$$\begin{pmatrix} x' \\ y' \\ z' \end{pmatrix} = R_z(45^\circ) \begin{pmatrix} x \\ y \\ z \end{pmatrix}. \tag{2.73}$$

The second rotation is by angle θ about the x'-axis in order to define the principal axes $\{x'',y'',z''\}$, while maintaining the x''-axis parallel with the propagation direction:

$$\begin{pmatrix} x'' \\ y'' \\ z'' \end{pmatrix} = R_{x'}(\theta) \begin{pmatrix} x' \\ y' \\ z' \end{pmatrix}. \tag{2.74}$$

We arrive at the version of eq. 2.71 in the principal axes of the perturbed system by combining these coordinate transformations to achieve:

$$1 = \left(\frac{x''}{n_{x''}}\right)^2 + \left(\frac{y''}{n_{y''}}\right)^2 + \left(\frac{z''}{n_{z''}}\right)^2, \tag{2.75}$$

where the principal refractive indices in the presence of the THz-induced perturbation have become:

$$\begin{aligned} n_{x''}^2 &= \left(\frac{1}{n_O^2} + r_{41}|\vec{E}_{\mathrm{THz}}(t)|\cos(\alpha)\right)^{-1} \\ n_{y''}^2 &= n_O^2\Big(1 - n_O^2 r_{41}|\vec{E}_{\mathrm{THz}}(t)|\big(\cos(\alpha)\sin^2(\theta) + \cos(\alpha+2\theta)\big)\Big)^{-1} \qquad (2.76) \\ n_{z''}^2 &= n_O^2\Big(1 - n_O^2 r_{41}|\vec{E}_{\mathrm{THz}}(t)|\big(\cos(\alpha)\cos^2(\theta) - \cos(\alpha+2\theta)\big)\Big)^{-1}. \qquad (2.77) \end{aligned}$$

Since we will show in Sect. 3.5 that our relatively weak field strengths are below the kV/cm level and the linear electro-optic coefficients are of magnitude $r_{41} = 0.87 \times 10^{-12}$ m/V for GaP [81] and $r_{41} = 4.04 \times 10^{-12}$ m/V for ZnTe [82], then we can safely truncate the binomial expansion of eqs. 2.76 and 2.77 to the second of their terms:

$$\begin{aligned} n_{y''} &\approx n_O + \frac{n_O^3}{2} r_{41}|\vec{E}_{\mathrm{THz}}(t)|\big(\cos(\alpha)\sin^2(\theta) + \cos(\alpha+2\theta)\big) \\ n_{z''} &\approx n_O + \frac{n_O^3}{2} r_{41}|\vec{E}_{\mathrm{THz}}(t)|\big(\cos(\alpha)\cos^2(\theta) - \cos(\alpha+2\theta)\big). \end{aligned}$$

A linearly-polarized NIR pulse propagating through this now-birfringent electro-optic medium will see its orthogonal polarization components accumulate different phase. In this case, for a medium of thickness d, the phase retardation Γ experienced by the polarization components of the NIR pulse projected onto the orthogonal y''- and z''-axes is:

$$\begin{aligned} \Gamma(t,\omega) &= \frac{\omega d}{c}\big(n_{y''} - n_{z''}\big) \qquad (2.78) \\ &\approx \frac{\omega d}{c}\frac{n_O^3 r_{41}|\vec{E}_{\mathrm{THz}}(t)|}{2}\Big(\cos(\alpha)\big(\sin^2(\theta) - \cos^2(\theta)\big) + 2\cos(\alpha+2\theta)\Big). \qquad (2.79) \end{aligned}$$

This phase modulation causes the polarization of the NIR pulse to rotate as a function of the electric field of the THz pulse. In particular, eq. 2.79 depends on the strength of the THz field $|\vec{E}_{\mathrm{THz}}(t)|$ at the time of overlap t and also on the sign of the THz field through the angular dependence on α. The degree of induced ellipticity constitutes the physical basis for our coherent electro-optic detection scheme. The essential point is that since typical THz pulses have pulse durations on the order of picoseconds, the NIR pulse, which can be shorter by at least an order of magnitude, will experience a different phase modulation depending on its arrival time within the THz pulse. In other words, the modulation imparted to NIR probe can be used to sample the local oscillations of the THz field.

Experimental realization of this technique requires passing the modulated NIR pulse through a series of detection optics, as will be shown in Section 3.2. Directly after its transmission through the electro-optic crystal, the NIR pulse is first sent through a quarter-wave plate. The role of the quarter-wave plate is to circularize the polarization of the NIR probe in the absence of the modulation. Then, the probe is passed through a Wollaston prism in order to direct its orthogonal polarization components towards two separate photodiodes.

One then optimizes these optics so that in the absence of the THz modulation, a circularly-polarized probe is produced and split into two beams of equal intensity. However, THz field-induced ellipticity in the probe disrupts the balance and causes the photodiodes to detect different intensities. Measurement of the intensity difference is performed by subtracting the signals from the two photodiodes and then amplifying the differential signal with a lock-in amplifier. This differential signal can be expressed in the laboratory reference frame $\{x^*, y^*, z^*\}$ from Fig. 2.11 as [78]:

$$\begin{aligned}\Delta I(t,\omega,\alpha,\psi) &= |E_{x^*}|^2 - |E_{y^*}|^2 \\ &= I_p \sin\big(2(\psi-\theta)\big)\sin\big(\Gamma(t,\omega)\big),\end{aligned} \tag{2.80}$$

where ψ is the angle of the incident NIR polarization with respect to the [001]-axis and I_p is its intensity. With our weak THz field strengths, we can safely assume that our detection scheme operates in the linear range such that $\sin(\Gamma) \approx \Gamma$. It should be noted that the breakdown of this assumption can lead to ambiguities in the measured signal [83], especially in the case of thick electro-optic crystals. After some simple trigonometry, we arrive at:

$$\Delta I(t,\omega,\alpha,\psi) = I_p \frac{\omega d}{c}\frac{n_O(\omega)^3 r_{41}|\vec{E}_{\mathrm{THz}}(t)|}{2}\Big(\cos(\alpha)\sin(2\psi) + 2\sin(\alpha)\cos(2\psi)\Big), \tag{2.81}$$

which expresses a measurable intensity imbalance that depends on the magnitude and polarization of the THz electric field at the arrival time of the probing NIR pulse.

If an experimentalist was posed with optimizing their detection scheme, the challenge would be to independently vary the NIR and THz polarizations. However, solving eq. 2.81 analytically reveals that the maximum signal can be achieved if the polarizations of the NIR and THz fields are set either parallel ($\psi = \alpha$) or orthogonal ($\psi = \alpha + \pi$) at particular angles with respect to the medium [78]. For example, parallel polarizations maximize the signal if they make an angle of $\alpha = \psi = 3\pi/2$ with respect to the [001]-axis. Furthermore, eq. 2.81 can be used to verify the prediction we made earlier in Sect. 2.2 that the optimal orientation of a (110)-oriented zinc-blende crystal for optical rectification generates vertically-polarized THz light. This vertical polarization of the THz field corresponds to the angle $\alpha = 0$. Let us assume that the polarization of such a THz field is maintained at the location of the detection medium. If we bring in a NIR probe that is also vertically polarized, then the last degree of freedom for this thought experiment is the orientation of the medium with respect to these polarizations. By rotating the medium about the [110]-axis, it can be seen that eq. 2.81 goes to zero when the [001]-axis is aligned with the vertical direction and therefore $\alpha = \psi = 0$. If a zero cannot be found experimentally then either the THz polarization is inferred to be elliptical.

In this section, we have discussed a means of detecting the slow oscillations of the electric field of a THz pulse. We arrived at eq. 2.81 by converting the THz field-induced phase modulation into an intensity imbalance in the orthogonal polarization components of a probing NIR pulse. Since the modulation directly depends on the electric field of the THz pulse, it is possible to realize an experimental detection technique based on this coherent mechanism. Simply by sweeping the timing of shorter NIR pulse through the longer duration of the THz pulse, we can measure the local oscillations of the THz field. As a function of the relative optical delay between the pulses, this cross-correlation technique constitutes the method of electro-optic sampling.

2.3.3 Transfer Matrix Formalism of Electro-Optic Sampling

In Section 2.3.2, we introduced a procedure for electro-optic sampling in the time domain by accounting for the influence of the THz-induced Pockels effect on a co-propagating NIR pulse. The NIR pulse acted as an optical gate, sampling only the part of the THz field that it overlaps with in time. Here we complement the discussion with an equivalent frequency-domain approach whose classical theory was first formalized by Grischkowsky and Gallot [84]. The authors interpreted the problem through the lens of nonlinear optics, akin to our discussion of optical rectification earlier in Sect. 2.2. Specifically, they considered how the NIR pulse acquires phase-coherent sidebands through sum and difference frequency mixing with the THz pulse during their co-propagation in an electro-optic medium. For example, a high-frequency NIR component of the probe can be down-shifted to the central carrier frequency by the subtraction of an appropriate THz frequency component. These additional terms impart their own respective phases onto the initially linearly-polarized NIR probe, causing dephasing as described in the previous section. The main result of this formalism is that the measured signal $S(\Omega)$ is simply the product of a transfer function $f(\Omega)$ acting on the generated THz spectrum $E_{\mathrm{THz}}(\Omega)$:

$$S(\Omega) = \frac{\pi\epsilon_0}{c} f(\Omega) E_{\mathrm{THz}}(\Omega). \tag{2.82}$$

If the electro-optic response function $f(\Omega)$ were frequency-independent, then the measurement would faithfully replicate the shape of the THz spectrum. However, this function contains experimental features that can cause pulse distortion and loss of bandwidth [85]. Using the approximation that the NIR pulse has a small spectral bandwidth compared to its central frequency, such that $\Delta\omega \ll \omega \approx \omega_0$, the multiple spectral filters that make up the electro-optic response function are:

$$f(\Omega) \approx C(\omega_0, \Omega)\tilde{P}(\omega_0, \Omega) t_{\mathrm{THz}} \tilde{T}_{\mathrm{NIR}} \tilde{C}_{\mathrm{ACF}}(\omega, \Omega). \tag{2.83}$$

The first term collects the following coefficients:

$$C(\omega_0, \Omega) = \chi^{(2)}(\omega_0; \omega_0 - \Omega, \Omega) \frac{c\omega_0}{\mathbb{R}[\tilde{n}(\omega_0)]}, \tag{2.84}$$

which contains factors that involve material properties specific to the chosen electro-optic medium such as the second-order nonlinearity for the Pockels effect $\chi^{(2)}$ and dispersion through the refractive index. Next, the second multiplicative term incorporates the phase-matching condition between the NIR and THz field components, similar to eq. 2.56 for optical rectification, for the coherent addition of the sum and difference frequency components:

$$P(\omega_0, \Omega) = \frac{e^{i\Delta\tilde{k}(\omega_0,\Omega)L_{\mathrm{det}}} - 1}{i\Delta\tilde{k}(\omega_0, \Omega)}, \tag{2.85}$$

where L_{det} is the thickness of the electro-optic medium and the complex wave-vector mismatch is $\Delta\tilde{k}(\omega, \Omega) = -\tilde{k}(\omega_0 + \Omega) + \tilde{k}(\Omega) + \tilde{k}(\omega_0)$. The real part of $\Delta\tilde{k}(\omega, \Omega)$ corresponds to the mismatch of the phase velocities of the THz components and the NIR group velocity. The imaginary part of $\Delta\tilde{k}(\omega, \Omega)$ represents the absorptive losses. The next two terms in eq. 2.83 account for the Fresnel coefficient factors for each of the fields:

$$t_{\mathrm{THz}} = \frac{2n_{\mathrm{air}}}{n_{\mathrm{air}} + n(\Omega)} \tag{2.86}$$

$$\tilde{T}_{\mathrm{NIR}} = \frac{4n_{\mathrm{air}} n(\Omega)}{\big(n_{\mathrm{air}} + n(\Omega)\big)^2} e^{-\mathbb{I}[\tilde{k}(\omega_0)]L_{\mathrm{det}}}. \tag{2.87}$$

We have assumed that the electro-optic medium is immersed in air and that the THz field is negligibly absorbed during its propagation. To affect the NIR pulse, the THz pulse only needs to enter and traverse the medium while the NIR pulse must also leave through the exit interface in order to be detected. For our purposes here, we neglect these Fresnel coefficients since they are relatively constant over our bandwidth and therefore have a negligible effect on the shape of the resulting THz spectra.

Finally, the last term of eq. 2.83 emphasizes the second-order nature of the nonlinear detection process. We showed before in Sect. 2.3.2 that the intensity imbalance given by eq. 2.81 expresses the influence of the THz field on the intensity of the NIR pulse via the Pockels effect. This nonlinear interaction manifests here via the spectral autocorrelation function of the NIR pulse:

$$\tilde{C}_{\mathrm{ACF}}(\omega, \Omega) = \int_{-\infty}^{\infty} \tilde{A}(-\omega)\tilde{A}(\omega - \Omega)\, \mathrm{d}\omega. \tag{2.88}$$

One usually considers autocorrelation in time as it is easier to form an intuitive picture in the time domain. In this situation, one pulse is held fixed in time while another is swept across it and the signal they produce corresponds to their total overlap. In fact, we will detail such a procedure in Chapter 3 as a means of measuring the duration of our NIR pulses. On the other hand, equation 2.88 utilizes a similar frequency-domain idea where each spectral component of the THz field is swept individually across the entire spectrum of the NIR pulse. As mentioned earlier in this section, it is through this nonlinear interaction that the THz field produces phase-coherent sidebands in the NIR spectrum through sum and difference frequency mixing. If one properly accounts for the minus sign differing between the sum and difference terms, one describes the mixing process simply in terms of the difference term in the form of the spectral autocorrelation given by eq. 2.88.

Using the same basic Gaussian model of the amplitude spectrum for an incident NIR pulse as before in Sect. 2.2.5, Fig. 2.12 plots the spectral autocorrelation given by eq. 2.88 for NIR amplitude spectra given various FWHM amplitudes. From this figure, we see that a significant drop-off in detection efficiency is expected at high THz frequencies since they only efficiently combine with the frequencies at the edges of the NIR spectra. The half-width at half-maximum (HWHM) amplitude for each of the calculated curves conform to the relation $\nu^{\mathrm{ACF}}_{\mathrm{HWHM}} = \nu^{\mathrm{NIR}}_{\mathrm{FWHM}}/\sqrt{2}$, as expected from eq. 2.88. Clearly, a prerequisite for sampling a THz pulse with a certain bandwidth is the use of a NIR gate with a greater spectral bandwidth.

The multiplicative terms in eq. 2.83 as a whole comprise a transmissive transfer function that must be accounted for in order to reconstruct the spectrum of the generated THz pulse. We show numerical calculations of this electro-optic response function $f(\Omega)$ in Fig. 2.13 for GaP and Fig. 2.14 for ZnTe with various choices of medium thickness L_{det}, each using a fixed FWHM amplitude of 5.0 THz for the NIR gate centred on 1035 nm. For the same thickness, GaP crystals demonstrate broader detection capabilities than ZnTe crystals due to their broader phase-matching properties. Also note the reappearance of minima at the same frequencies as seen before in Figs. 2.9 and 2.10 for optical rectification. Again, the lowest-frequency minimum in transmission marks the onset of incoherence between the travelling THz field components and the NIR group velocity. Since the refractive index increases with frequency, we know that higher THz frequencies travel at phase velocities slower than the NIR group velocity. The NIR pulse cannot match the slow pace of these

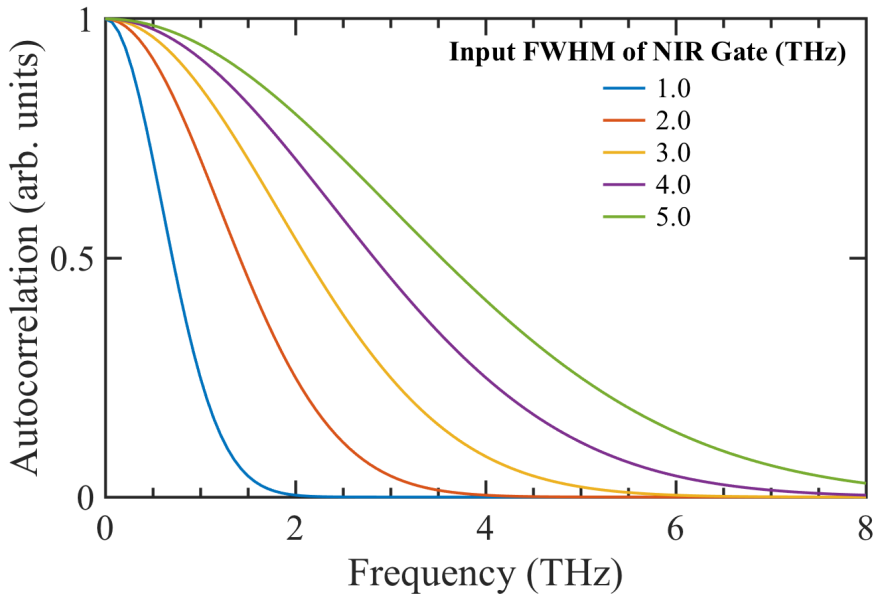

Figure 2.12: Calculated spectral autocorrelations of a NIR gating pulse with amplitude spectra centred on 1035 nm (about 290 THz) for various choices of the FWHM-amplitude of the input NIR gate.

THz frequencies and will sweep across multiples of their periods of oscillation by the time it leaves the detection medium. This effectively averages the resulting signal, leading to destructive interference at the minima observed in the figures. Therefore, we verify the statement made in Sect. 2.2.5 that the phase-matched bandwidth supported by an electro-optic medium for optical rectification is equivalent to that able to be detected by the same medium through the inverse process based on the linear electro-optic effect.

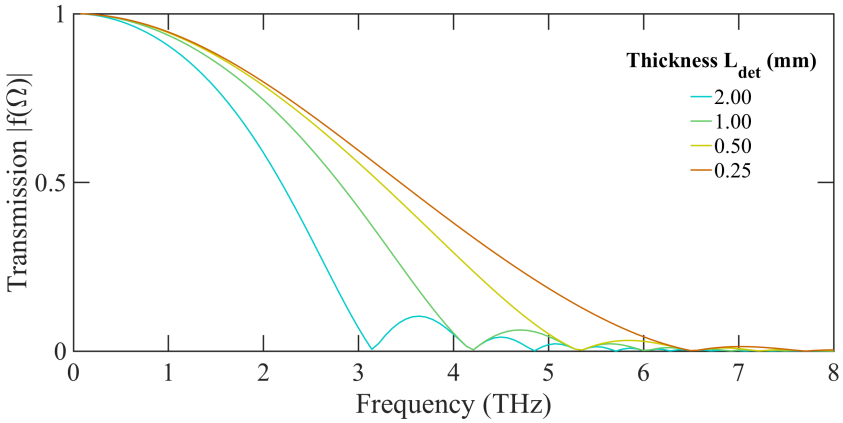

Figure 2.13: Calculated electro-optic spectral response function using a (110)-oriented GaP crystals and a NIR gating pulse with an amplitude spectrum centred on 1035 nm with a FWHM of 5.0 THz. Results are shown for a variety of detector crystal thicknesses, related by factors of two.

We are now in a position to calculate the THz spectra resulting from electro-optic detection by applying the electro-optic response function to the generated THz spectra predicted by eq. 2.57. In Fig. 2.15, we show the result of using a NIR gate pulse centred at

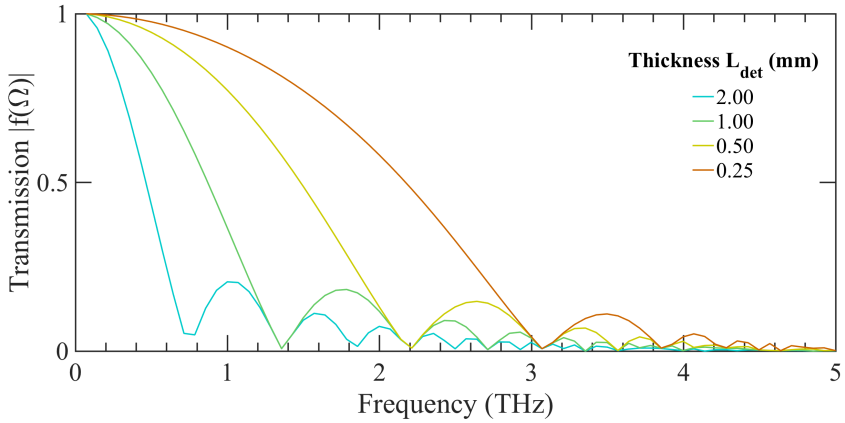

Figure 2.14: Calculated electro-optic spectral response function using a (110)-oriented ZnTe crystals and a NIR gating pulse with an amplitude spectrum centred on 1035 nm with a FWHM of 5.0 THz. Results are shown for a variety of detector crystal thicknesses, related by factors of two.

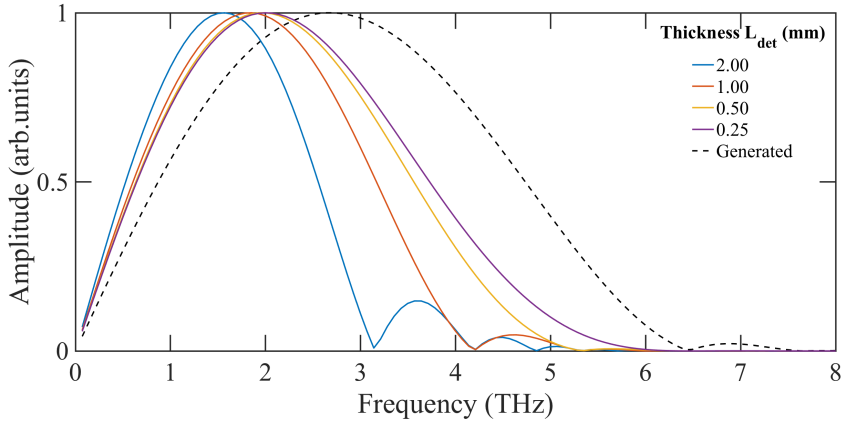

Figure 2.15: Calculated THz spectra after electro-optic detection by a GaP crystal of the indicated thickness. The NIR gating pulse used was given an amplitude spectrum centred on 1035 nm with a FWHM of 5.0 THz. Each curve is normalized to show the impact of the spectral filters due to the electro-optic response function.

1035 nm with an amplitude FWHM of 5.0 THz on the signals generated by a 250 μm thick (110)-oriented GaP crystal and detected by the same type of crystal but with a variety of thicknesses. The black dashed curve shows the spectrum calculated at generation while the colourful curves show the effect of multiplying this curve by the appropriate electro-optic response function corresponding to the indicated thickness of the detection medium (see Fig. 2.13). Clearly, the thinner media are much better suited for detection due to their broader phase-matching abilities. However, spectral filtering is evident in all cases since the NIR gating pulse we chose to use was the same as the pulse used to pump the generation. This crucial factor is important to keep in mind as typical THz time-domain spectrometers are seeded by the same pulse for THz generation and detection. Ref. [86] presents an investigation into the effect of spectral broadening of the NIR pulses on the generation and detection of THz pulses.

In conclusion, the formalism presented in this chapter outlines the key physical consid-

erations required to prepare a THz time-domain spectrometer based on nonlinear optical effects. We utilized phase-matching arguments and geometrical considerations to predict the THz spectra generated from optical rectification and detected by electro-optic sampling using NIR pulses and nonlinear media with known properties. Although our choice of zinc-blende type nonlinear media are advantageous for their low dispersion and low absorption of THz light, we found that the thickness of the media can be a limiting factor for both the generation and detection of pulsed THz radiation in addition to the spectral bandwidth of the NIR pulses that seed the nonlinear optical interactions.

Chapter 3

Experimental Apparatus

This chapter outlines the development and experimental setup of a state-of-the-art THz time-domain spectrometer. Our main objective is to detail the major constituents of the spectrometer including its ability to perform time-resolved THz generation and detection. An important advantage in conducting time-domain spectroscopy with our system is that both the generation and detection of the pulsed THz radiation are optically gated events. Therefore, we begin by outlining the functionality of the PHAROS laser system and how it produces short, amplified NIR pulses that are tunable in power, chirp and energy. Next, we introduce the experimental apparatus we use to conduct spectroscopy. Based on the theory proposed in Chapter 2, our discussion here seeks to explain the means by which we achieve THz generation via optical rectification and its subsequent detection via electro-optic sampling in the laboratory. Every THz pulse after generation is manipulated by a series of identical off-axis parabolic mirrors which are set up to either collect or focus the radiation. This arrangement provides multiple points in space where the THz radiation is brought to a focus, thus enabling us to conduct transmission spectroscopy on materials and then detection. In Chapter 4, we make use of this geometry to conduct our spectroscopic technique on the zinc-blende semiconductors used here as THz emitters and detectors. Finally, the chapter culminates in a comparison of the results of the numerical treatment in Chapter 2 and the experimentally measured signals with the goal of identifying challenges and limitations.

3.1 Producing Ultrashort Pulses with the PHAROS Laser System

Since the late 1980s, the key ingredient enabling THz generation and detection systems has been the steady technological advancement of short and intense pulses of light produced by femtosecond lasers. However, our treatment of short pulses thus far has been confined to a mathematical description from the point of view of nonlinear optics. In this section, we outline the experimental techniques used to obtain short pulses from a femtosecond laser and amplify them to higher intensities as required for driving nonlinear optical processes.

Previously in Chapter 1, we discussed several advancements in semiconductor fabrication and in nonlinear optics that have been instrumental in facilitating terahertz science. However, this progress is in spite of the fact that conventional semiconductor lasers are

unable to operate at THz frequencies. Recall that the mechanism by which a semiconductor diode laser outputs light is through the recombination of an electron and hole pair. This event results in the emission of a photon whose energy corresponds to a direct transition between energy levels in the gain medium. Importantly, semiconductors have band-gap energies on the order of electron-volts. Even if such a band-gap could be engineered at 4.1 meV, the corresponding 1 THz photon emitted would be clouded by the thermal background at room temperature. The central frequency of the technological THz gap is particularly interesting to note since it corresponds to the frequency at which photon energies match thermal energies, occurring at approximately $\nu = k_B T/h \approx 6.2$ THz [11]. Therefore, random thermal effects that are ordinarily overcome through stimulated emission in the higher energy regimes of the NIR and the visible are enough to disrupt the coherence needed to sustain conventional lasing at THz frequencies. In spite of this, the combination of conventional femtosecond lasers and nonlinear methods of optical mixing in semiconducting media has become widely adopted to realize the generation of intense pulses of THz radiation.

Femtosecond lasers operate based on mode-locking principles. At the heart of the laser lies a resonator cavity which is simply an active gain medium placed between two mirrors, one of which is partially transmissive and the other entirely reflective. This geometry imposes longitudinal cavity modes, therefore gain media with broad bandwidths are chosen and can typically support the lasing of hundreds of thousands of frequencies. However, in a free-running configuration these cavity modes oscillate independently and the laser outputs a continuous wave of power equal to the average of their random fluctuations. A mode-locked configuration forces a fixed phase relationship between the modes and their resulting superposition produces a pulse train at moments of synchronous constructive interference. The pulses repeat with a period equal to the cavity round-trip time and their duration is determined by the phase relationship. One way in particular to induce mode-locking is through a passive technique called Kerr-lens mode-locking, as sketched in Fig. 3.1, where a gain medium displaying a third-order Kerr nonlinearity is chosen. As mentioned previously in Sect. 2.3.2, the Kerr effect describes a change in the refractive index of the medium proportional to the incident intensity[1]. Typical lasers operate with Gaussian transverse intensity profiles; therefore the electro-optic medium itself acquires a Gaussian refractive index profile. The medium acts as a lens because the centre of the beam experiences a higher refractive index than the edges. Since the amount of focusing increases with intensity, introducing an aperture in the cavity rejects low intensities. In other words, the role of the aperture is to select out the phase relationship that produces the highest intensity: a pulse.

Since the Fourier transform relates temporal and spectral characteristics, the pulse duration τ_{FWHM} and spectral bandwidth $\Delta\nu_{\mathrm{FWHM}}$ (both with respect to intensity) cannot vary independently. For the case of Gaussian intensity profiles, these quantities conform to the fundamental relation $\tau_{\mathrm{FWHM}}\Delta\nu_{\mathrm{FWHM}} \geq 0.441$ [87]. If the pulse properties satisfy the equality, the pulse is called Fourier transform-limited. This time-bandwidth product signifies that larger gain bandwidths are required to achieve shorter pulses. A list of common media with broad gain bandwidths that support femtosecond lasing are given in Table 3.1. In particular, the Ti:Sapphire gain medium has been the workhorse of femtosecond lasers for the last few decades due to its abnormally broad spectral bandwidth which extends from

[1] In eq. 2.68, the Kerr effect was shown to depend on the square of the electric field. The intensity is related to the time-averaged Poynting vector via $I = |\langle \vec{S} \rangle| = \frac{1}{2}\epsilon_0 cn|E_0|^2$, usually given in W/cm^2.

Table 3.1: Common gain media with broad bandwidths used in femtosecond lasers [89].

Gain Medium	**Bandwidth**
Ti:Sapphire ($Ti:Al_2O_3$)	650 - 1100 nm
Yb doped materials (Yb:KGW, Yb:YAG)	1020 - 1050 nm
Alexandrite ($Cr:Be_2O_3$)	700 - 820 nm
Colquirites (Cr:LISAF, Cr:LICAF, etc.)	800 - 1000 nm
Fosterite	1250 - 1300 nm
Glasses (Nd:glass)	1040 - 1070 nm

Figure 3.1: Sketch of the Kerr-lens mode-locking technique to produce short NIR pulses. Adapted from the PHAROS laser manual [90].

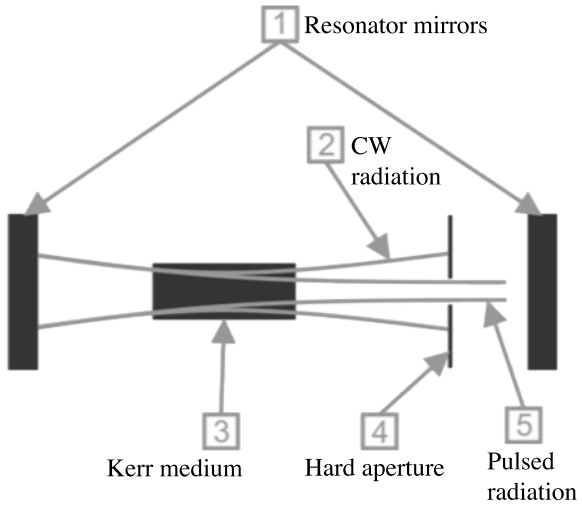

650 to 1100 nm. Alternative gain media that have found regular use in femtosecond laser systems include Yd-doped materials such as Yb:KGW crystals[2]. Since these gain media output light centred at NIR wavelengths, they are advantageous to use for THz generation in combination with, for example, semiconductors such as GaP and ZnTe because broad phase-matching can be achieved as we saw in Chapter 2. These crystals have a similar band-gap corresponding to about 550 nm [68], which is direct for ZnTe and indirect for GaP. Therefore, choosing a NIR femtosecond laser can reduce the impact of multi-photon absorption processes significantly for these two crystals [88].

Our PHAROS laser system (Light Conversion, Ltd. model PH1-SP-1.5mJ) exploits the technique of Kerr-lens mode-locking to produce short NIR pulses. Its oscillator contains a Yb:KGW crystal with a gain bandwidth centred on 1035 nm that is pumped into population inversion by a semiconductor diode laser. The PHAROS oscillator produces pulses that repeat at a fixed rate of $f_{\text{rep}} = 76$ MHz, each with FWHM pulse duration of about $\tau_{\text{FWHM}} = 90$ fs and they reach average powers of about $P_{\text{ave}} = 4.0$ W. These

[2]Yb:KGW stands for ytterbium doped potassium gadolinium tungstate.

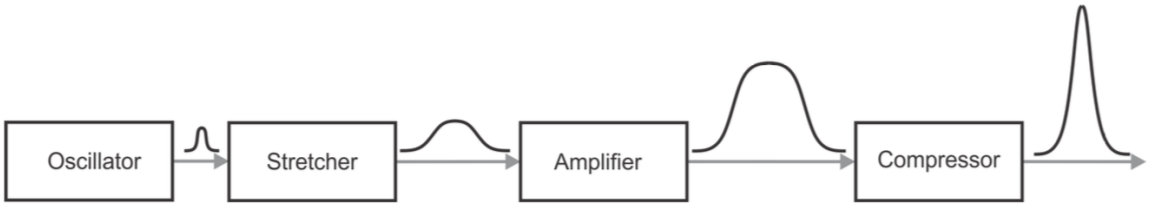

Figure 3.2: The stages of chirped pulse amplification. Adapted from the PHAROS laser manual [90].

parameters correspond to output pulse energies of $\varepsilon = P_{\text{ave}}/f_{\text{rep}} = 0.05\ \mu\text{J}$. Recall that our use of nonlinear optical methods requires high pulse intensities beyond the threshold of linear optics. Specifically, our discussion of the THz spectrum generated by optical rectification depended on the product of two spectral amplitudes within the NIR spectrum (see eq. 2.57). Therefore, in practice, the efficiency of optical rectification depends on the intensity of the NIR light. Although the PHAROS oscillator provides a sufficient pulse energy to achieve THz generation, a major research goal of this thesis is to perform transmission spectroscopy through a sample. This task requires THz pulse energies high enough to traverse the sample with minimal loss of spectral content, keeping in mind that absorptive losses increase at higher THz frequencies (e.g. towards a phonon resonance).

The greater the NIR pulse energy, the stronger the THz pulse will be when produced through optical rectification. In this vein, we make use in this thesis of the amplification stage in the PHAROS laser head that follows the oscillator. About 1.0 W of the total power from the oscillator is passed into a regenerative amplifier where the technique of chirped pulse amplification (CPA) is used to increase the pulse energy. The rest of the oscillator power exits an external port on the laser head to be available for other experiments. In essence, the regenerative amplifier is simply a cavity containing another gain medium which in the PHAROS is another Yb:KGW crystal. Amplification is achieved by passing the beam many times through the gain medium, which is also pumped into population inversion by a diode laser, each time building up more and more photon flux due to stimulated emission.

The basic idea behind CPA is to amplify the pulse energy while at the same time keeping the pulse intensity below the threshold that enables parasitic nonlinear effects, such as the onset of self-focusing. As shown schematically in Fig. 3.2, this is accomplished by stretching the pulses in time before amplification. Pulse stretching is a way of intentionally modulating or "chirping" the instantaneous frequency of the pulse as a function of time. Pulse chirp is the optical analogue to the sound of a bird's tweet or of a passing train and can be affected by dispersive optics. We will focus our attention on the case of linear chirp where frequencies are spread linearly in time. For instance, positive chirp corresponds to the case where low frequencies are made to arrive in time before high frequencies. The opposite case of negative chirp is where blue wavelengths lead red wavelengths (or, high frequencies lead low ones). Figure 3.3(b) shows the effect of adding negative chirp to the Fourier transform-limited pulse with a Gaussian intensity profile shown in Fig. 3.3(a). The pulse duration increases from about 130 to 347 fs due to the redistribution of the frequencies and the peak intensity decreases accordingly since the total intensity is ideally conserved.

In the PHAROS laser system, two diffraction gratings are used to affect the chirp. The

first grating angularly disperses each frequency component along different optical path lengths in order to impart on them a frequency-dependent time delay and the second grating re-collimates the stretched beam. Amplified pulses are picked out from the cavity at a repetition rate set by the electronic activation of a Pockels cell which functions similar to the THz-induced Pockels effect described in Sect. 2.3. When activated by a static electric field, a Pockels cell rotates the polarization of the amplified pulse so that it may pass a Faraday isolator and leave the amplifier. Finally, the amplified pulses navigate through a compression stage that is comprised of similar dispersive optics to compensate the pulse stretching. Ultimate control over the chirp parameter of the pulses is set by the position of the compressor line. Exiting the output port of the regenerative amplifier are finely-tuned high energy pulses of NIR light which can have a maximum average power of 6.0 W and a repetition rate between 1 kHz and 1.1 MHz, as controlled by the internal electronics through software.

A home-built second-harmonic intensity autocorrelator was used to characterize these pulses in the time domain [87]. In brief, the pulses are split in power by a beam-splitter and made to overlap non-collinearly on a BBO crystal. By configuring the two pulse replicas to arrive at the same time at the same spot on the crystal, the autocorrelation signal is created by the second-order nonlinear process of second harmonic generation. Momentum conservation finds that this newly generated beam appears halfway between the beams and therefore can be isolated for its measurement. Finally, by varying the time delay of one pulse with respect to the other, the strength of the generated second-harmonic is varied and constitutes a means to measure the temporal autocorrelation. Figure 3.4(a) shows a typical trace of the resulting temporal autocorrelation which has a FWHM-intensity duration of about 183 fs. After deconvolution by assuming our pulses have a Gaussian intensity profile, i.e. dividing by $\sqrt{2}$, this method finds a FWHM-intensity pulse duration of about 130 fs. The corresponding intensity spectrum shown in Fig. 3.4(b) was measured by directing a pulse into a USB spectrometer. The pulse spectrum has a FWHM-intensity of about 3.6 THz which makes available an FWHM-amplitude bandwidth of 5.1 THz as input to the model and previously shown in Fig. 2.8.

3.2 Design of the Experimental Setup

Our THz time-domain spectrometer is pumped by amplified femtosecond pulses produced from the PHAROS laser system. Figure 3.5 shows a schematic of the entire spectrometer. First, the NIR pulse train is split in power along two beam paths using an 80/20 beam splitter. Their differing intensities are indicative of their separate roles.

The more intense pulse runs along the THz generation arm. To reach the high intensities demanded by optical rectification, the pulse is focused using a lens on a noncentrosymmetric medium that exhibits an intrinsic second-order nonlinearity given by $\chi^{(2)}$. Shining the beam at normal incidence through the medium achieves collinear optical rectification (see Sect. 2.2.3) and generates a quasi-single-cycle pulse of THz radiation. This THz pulse, also known as a THz transient, is about 1 to 2 ps long and extends in spectral content over about 0-5 THz, both properties being due only to the pump laser bandwidth and choice of nonlinear medium. Importantly, recall from Sect. 2.2.4 that every THz pulse is phase-locked upon generation [76]. As the THz pulse diverges outwards from the source after emission, it is collected by a 90° off-axis parabolic mirror ($f = 2''$) coated in gold

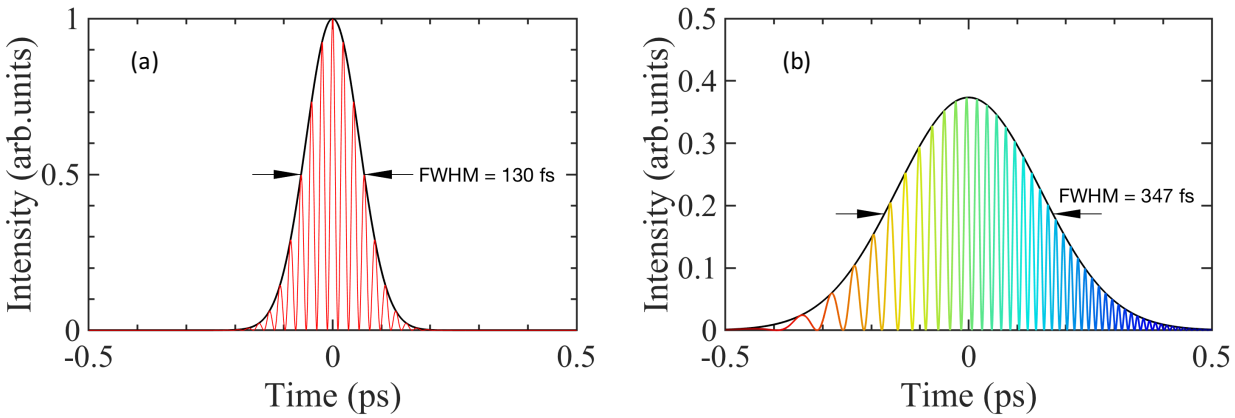

Figure 3.3: Illustration of numerically simulated pulses with Gaussian intensity profiles in time and with varying chirp. The artificial addition of negative chirp to the pulse shown in (a) produces the stretched pulse shown in (b). Since total intensity is conserved, the pulse duration is increased from about 130 fs to 347 fs and the peak amplitude decreases.

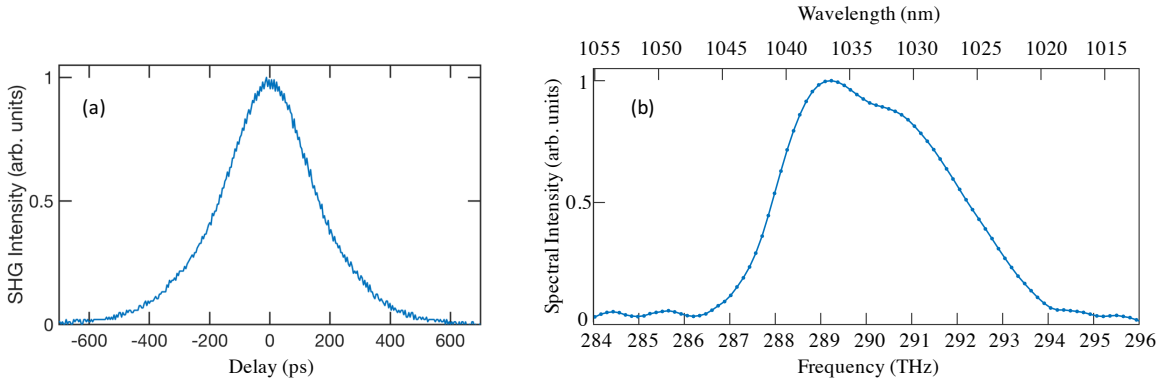

Figure 3.4: Measured (a) temporal autocorrelation based on second harmonic generation and (b) spectrum of an output pulse from the PHAROS regenerative amplifier. The FWHM duration of the intensity autocorrelation is about 180 fs and the corresponding FWHM-intensity bandwidth of the spectrum is about 3.6 THz.

whose high optical conductivity gives a large, broadband reflectance in the THz range [91]. Simply put, a parabolic mirror combines the ability to reflect light like a mirror and to focus (or collimate) it like a lens without the need to propagate through dispersive optics that would introduce undesirable chirp. Placing the THz source at the focus before the mirror ensures that the reflected THz beam is collimated. A Ge wafer is introduced in the THz beam path to remove any residual NIR pump light. As specified by the manufacturer, the thickness of the Ge wafer is 500 μm. Its high reflectivity allows the wafer to act as a dichroic mirror that transmits the THz radiation and reflects the NIR light to a beam dump. Next, an identical parabolic mirror brings all of the THz frequency components to a common focal plane [92]. Two more identical mirrors duplicate the geometry in order to re-collect and re-focus the THz pulses on a second noncentrosymmetric medium acting

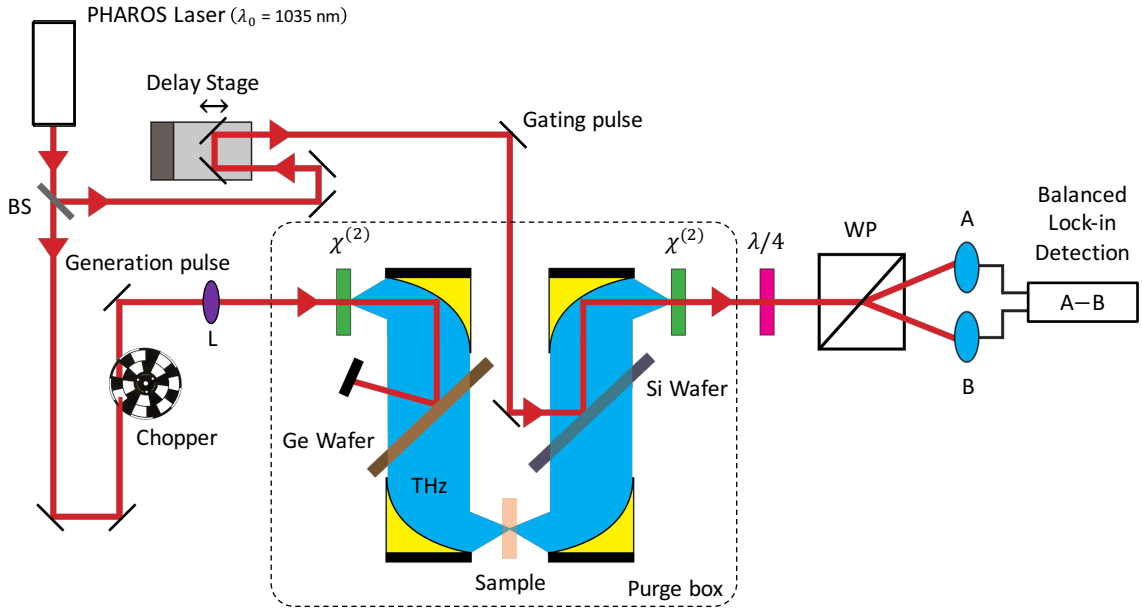

Figure 3.5: Experimental schematic of our THz time-domain spectrometer. $\chi^{(2)}$ = nonlinear crystal, BS = beam splitter, L = lens, $\lambda/4$ = quarter-wave plate, WP = Wollaston polarizer, A and B are photodiodes (Thorlabs FDS100).

as our THz detector. As shown in Fig. 3.5, the intermediate focus in between is used to conduct spectroscopy on a sample with high spatial resolution. Altogether, these guiding optics fix the path travelled by each generated THz pulse.

Meanwhile, the other arm of the beam splitter with lower optical power takes a different route. It first encounters two mirrors that are configured to retro-reflect the light and are mounted on a motorized translation stage. This NIR beam is then directed upon a high-resistivity Si beam splitter which picks off a partial reflection and aims it on the THz detector, focused via the final parabolic mirror, where it re-combines with the generation arm and acts as the optical gate in electro-optic detection. A crucial step in dealing with the two separate arms of the spectrometer is to maintain their spatial and temporal overlap at the location of the THz detector. This task ensures proper operation of the spectrometer and a high signal-to-noise ratio when the system is running. In this vein, the spectrometer was configured first as a second-harmonic intensity auto-correlator using a BBO crystal in the place of the THz detector. For this step we removed the Ge wafer. Spatial overlap was achieved by purposefully misaligning the gating arm with respect to the THz generation arm. A CCD camera focused on the exit of the BBO crystal was used to observe the appearance of a new beam at the second harmonic of the NIR light in between the two separate beams which signified spatial overlap. As the system was brought on line, the gating beam was walked back to the correct spot. Temporal overlap was achieved by carefully scanning the translation stage to maximize the brightness of the second harmonic beam.

Achieving spatial and temporal overlap in the spectrometer equates the optical path lengths travelled by the generated THz and NIR gating beams. As introduced in Sect. 2.3.2, translating the motorized stage imparts positive or negative optical delay on the NIR pulses. Since the THz beam path is fixed, performing a scan of the stage about the point of temporal overlap constitutes our coherent electro-optic detection scheme. For a

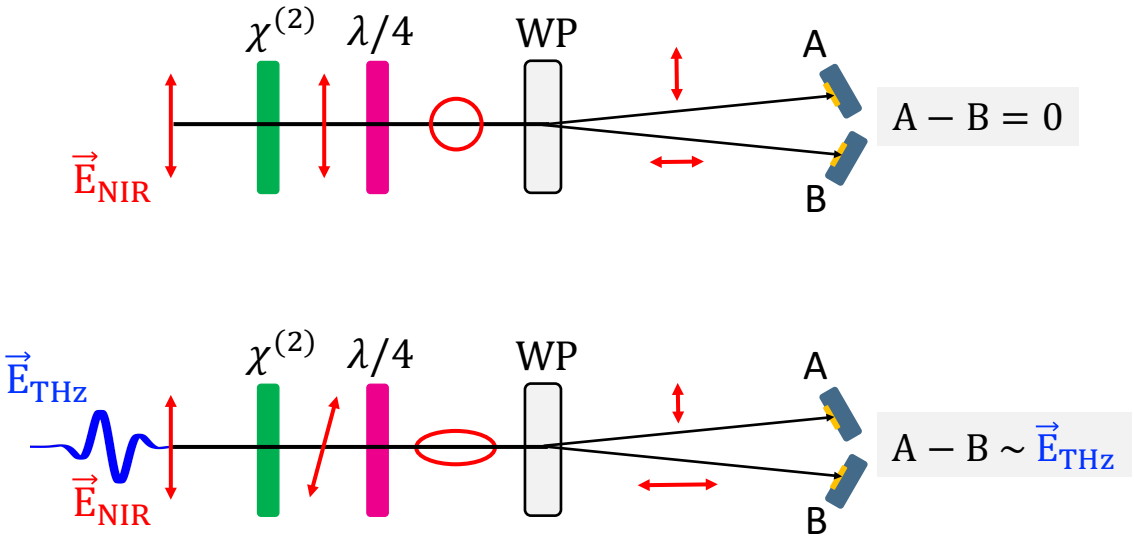

Figure 3.6: Illustration of the polarization rotation experienced by a NIR pulse via the THz-induced Pockels effect, producing a measurable intensity difference between photodiodes A and B in proportion to the collinear THz field. Symbols refer to Fig. 3.5.

prescribed delay, the NIR gating pulse opens up an ultrashort window within which it experiences a polarization rotation proportional to the instantaneous electric field of a THz pulse via the Pockels effect. The NIR pulse next passes through a quarter-wave plate that circularizes its polarization in the absence of the THz field and then a Wollaston polarizer to separate its orthogonal polarization components, as illustrated in Fig. 3.6. The intensity of the two arms of the Wollaston polarizer are measured by two photodiodes and a lock-in amplifier records their difference. As the delay stage is scanned across the THz pulse, the lock-in detection registers a time-varying intensity imbalance, as described mathematically in Sect. 2.3.2. Therefore, incrementally advancing the translation stage carries out a time-resolved measurement of the entire electric field, both amplitude and phase, of our THz pulses. To illustrate this point, Fig. 3.7 shows how the shot-by-shot method of reconstructing the THz field is performed. Importantly, the time-gated nature of this detection scheme suppresses incoherent thermal background radiation. A LabVIEW program was devised to control the step-size of the discrete motion taken by the translation stage and track the timing of the recorded data.

3.3 Spectral Analysis of the Measured THz Transients

Figure 3.8(a) shows a typical scan of a 1 ps long THz pulse emitted by a 200-μm thick (110)-oriented GaP crystal and detected using an identical crystal. The orientation of the nonlinear media were optimized in accordance with Sect. 2.2.2 for optical rectification and Sect. 2.3.2 for electro-optic detection. Note that the high THz absorption from atmospheric air in the room has been minimized by containing the essential optics in a purge box filled with N_2 gas to a constant relative humidity below 0.0%. In Fig. 3.8(b), the amplitude spectrum corresponding to this pulse was been determined using MATLAB's Fast Fourier Transform (FFT) function on the recorded data which shows coverage over 0-5 THz that peaks at 2.0 THz and has a FWHM bandwidth of 2.2 THz. An advantageous aspect of

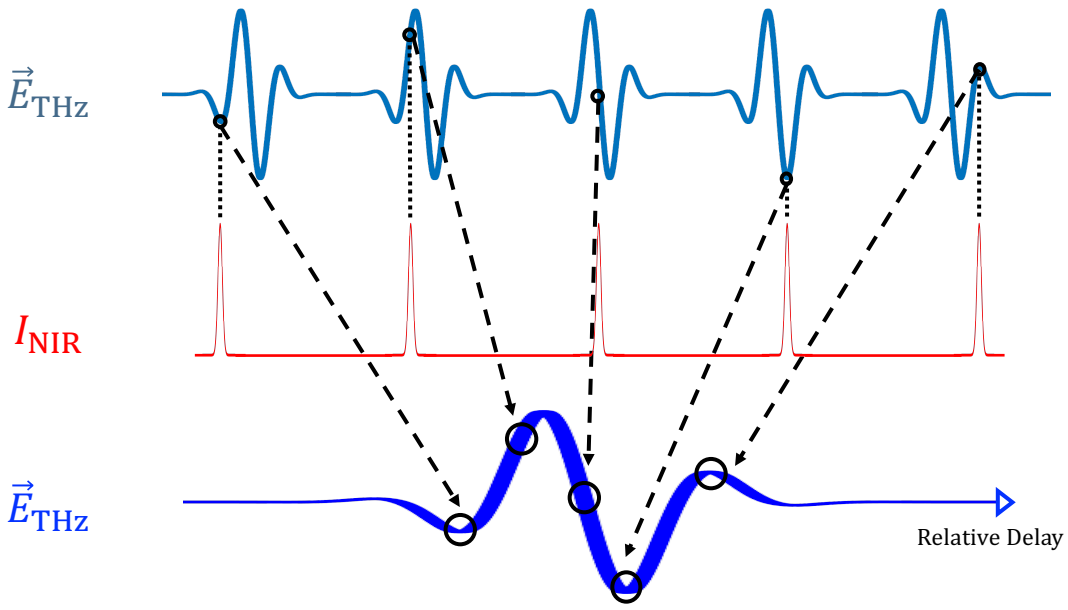

Figure 3.7: Illustration of the shot-by-shot procedure behind electro-optic sampling using the variably-delayed NIR pulses, each of which records the local oscillation of the electric field of the THz pulse.

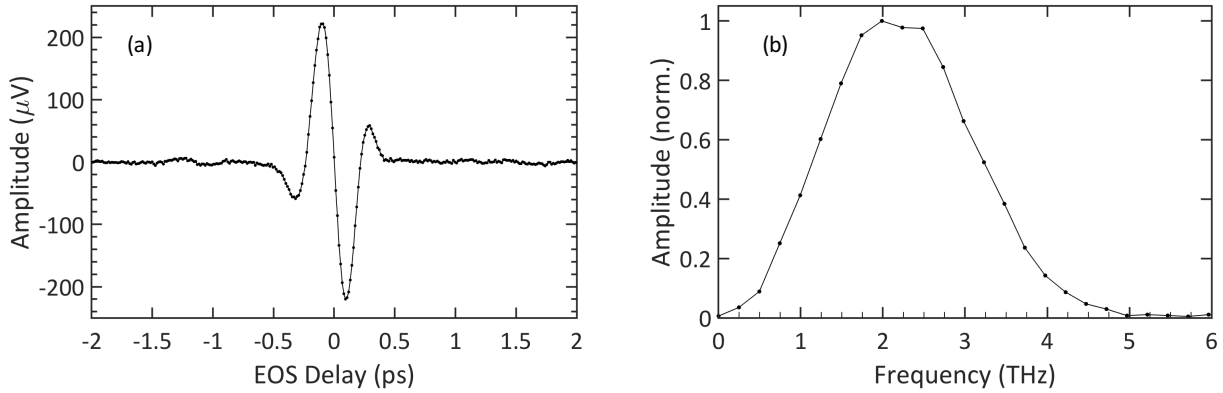

Figure 3.8: Measured THz transient (a) and corresponding amplitude spectrum (b) of a THz pulse generated by a 200-μm thick (110)-oriented GaP crystal and detected with by EO sampling with an identical crystal.

the time-resolved detection method described here is that the total scan length of 4 ps is the sole factor in determining the frequency resolution of $\Delta f = 0.25$ THz.

The delay stage was incremented in steps of $\Delta z = 2$ μm which translates to a time resolution of:

$$\Delta t = \frac{2\Delta z}{c} = 13.3 \text{ fs}, \tag{3.1}$$

where the factor of two accounts for the retro-reflection. Since the measured signal is obtained by a sequence of discrete samples taken at regular intervals, there is a corresponding

Nyquist frequency equal to half the sampling rate $f_{\text{sam}} = 1/\Delta t$:

$$f_{\text{Nyquist}} = \frac{f_{\text{sam}}}{2} \approx 75.0 \text{ THz}. \tag{3.2}$$

Through the Fourier transform, given earlier by eq. 2.12, we know that a continuous signal of finite bandwidth such as the THz electric field can be decomposed into a set of sinusoids. Any spectral power contained in frequency components greater than the Nyquist frequency will be folded into the range of $-f_{\text{Nyquist}} < f < f_{\text{Nyquist}}$ by the discrete sampling process [93]. Should folding occur, the recorded data would give a false representation, or an alias, of the true signal. The effect of undersampling is to make high frequency components appear as low frequencies in the measured spectrum. However, the results of the simulation presented in Chapter 2, in particular Fig. 2.15, indicate that the spectral content of a THz pulse detected by a similar 250 μm thick GaP crystal should extend up to about 6 THz. Therefore, under the specified operating conditions of the spectrometer, the signal is instead greatly oversampled and aliasing is avoided. Similarly, another stable point of the stage was found to occur for a step-size of 10 μm which gives a time resolution of 66.7 fs and a Nyquist frequency of about 7.5 THz, also beyond the spectral bandwidth of our THz pulses.

3.4 Phase-Sensitive Lock-In Detection

The working principle behind our THz time-domain spectrometer is the conversion of optical phase-modulation into a measurable electronic signal such as the THz transient shown in Fig. 3.8. From this figure, we see that the data recorded by our balanced photodetection scheme are on the order of micro-Volts and ride atop a layer of noise. To perform this measurement accurately, we utilize a lock-in amplifier (Stanford Research Systems, model SR830m) which is a device capable of extracting weak signals from noisy electronic environments. Commercial lock-in amplifiers are ubiquitous and contain a complex combination of analog and digital circuitry. Their distinctive feature is that they employ phase-sensitive detection to isolate the signal from the noise. Our goal here is to outline the considerations one makes in using a lock-in amplifier (LIA) with our THz spectrometer.

3.4.1 Noise Rejection through Lock-In Detection

Our method of electro-optic sampling relies on each NIR pulse in the gating arm to deposit its energy on balanced photodetectors, as shown before in Fig. 3.5. Each of the resulting DC photocurrents are converted to a voltage by passing them through their own load resistor of equivalent resistance at their respective connections to the LIA. Inside the LIA, a low noise differential voltage amplifier indiscriminately boosts the difference between the signals as well as the noise it carries. In order to isolate the signal, a chopper wheel, spinning at a frequency ω_{chop} set by a function generator, is placed in the generation arm of the THz spectrometer. The DC difference signal is then frequency-modulated into a slowly-varying AC signal. Consider this signal to take the following sinusoidal form:

$$V(t) = V_{\text{s}} \sin(\omega_{\text{chop}} t + \theta_{\text{s}}) \tag{3.3}$$

By means of an internal local oscillator (LO), a phase-locked loop in the LIA generates a reference signal:

$$V_{\mathrm{ref}}(t) = V_{\mathrm{r}} \sin(\omega_{\mathrm{LO}} t + \theta_{\mathrm{r}}) \tag{3.4}$$

Next, a phase-sensitive detector (PSD) multiplies these two sinusoidal signals:

$$\begin{aligned} V_{\mathrm{PSD}}(t) &= V_{\mathrm{s}} V_{\mathrm{r}} \sin(\omega_{\mathrm{chop}} t + \theta_{\mathrm{s}}) \sin(\omega_{\mathrm{LO}} t + \theta_{\mathrm{r}}) \\ &= \frac{V_{\mathrm{s}} V_{\mathrm{r}}}{2} \Big(\cos\big((\omega_{\mathrm{chop}} - \omega_{\mathrm{LO}})t + \theta_{\mathrm{s}} - \theta_{\mathrm{r}}\big) - \cos\big((\omega_{\mathrm{chop}} + \omega_{\mathrm{LO}})t + \theta_{\mathrm{s}} + \theta_{\mathrm{r}}\big) \Big). \end{aligned} \tag{3.5}$$

A low-pass filter would effectively eliminate both of the AC terms in eq. 3.5. However, if the local oscillator is triggered to the chopper frequency so that $\omega_{\mathrm{LO}} = \omega_{\mathrm{chop}}$, then the first term at the difference frequency would become DC and survive. To see how this occurs in the time domain, recall that a low-pass (LP) filter outputs the average of its input over a time span τ [94]:

$$\begin{aligned} V_{\mathrm{out}}(t) \equiv \langle V_{\mathrm{PSD}}(t) \rangle &= \frac{1}{\tau} \int_0^{\tau} V_{\mathrm{PSD}}(t)\ \mathrm{d}t \\ &= \frac{V_{\mathrm{s}} V_{\mathrm{r}}}{2} \left(\frac{\sin\big((\omega_{\mathrm{chop}} - \omega_{\mathrm{LO}})\tau + \theta_{\mathrm{s}} - \theta_{\mathrm{r}}\big)}{(\omega_{\mathrm{chop}} - \omega_{\mathrm{LO}})\tau} - \frac{\sin\big((\omega_{\mathrm{chop}} + \omega_{\mathrm{LO}})\tau + \theta_{\mathrm{s}} + \theta_{\mathrm{r}}\big)}{(\omega_{\mathrm{chop}} + \omega_{\mathrm{LO}})\tau} \right) \end{aligned} \tag{3.6}$$

Clearly, both of these AC terms will tend to zero for a very long integration time. However, the first term on the right hand side at the difference frequency $(\omega_{\mathrm{chop}} - \omega_{\mathrm{LO}})$ oscillates slower than the term at the sum frequency $(\omega_{\mathrm{chop}} + \omega_{\mathrm{LO}})$. Therefore, longer integration times will narrow the detected bandwidth at the cost of a longer total measurement time. By locking the local oscillator to the chopper frequency, the output of the phase-sensitive detector becomes:

$$V_{\mathrm{PSD}}(t) = \frac{V_{\mathrm{s}} V_{\mathrm{r}}}{2} \Big(\cos\big(\theta_{\mathrm{s}} - \theta_{\mathrm{r}}\big) - \cos\big(2\omega_{\mathrm{chop}} t + \theta_{\mathrm{s}} + \theta_{\mathrm{r}}\big) \Big). \tag{3.7}$$

An optimal choice of the integration time reduces the filtered output to:

$$\langle V_{\mathrm{PSD}} \rangle = \frac{V_{\mathrm{s}} V_{\mathrm{r}}}{2} \cos(\theta), \tag{3.8}$$

where $\theta = \theta_{\mathrm{s}} - \theta_{\mathrm{r}}$ is the relative phase of the local oscillator to that of the signal. Therefore, we have arrived at an equation describing a DC signal proportional to the amplitude of the input signal V_s. The phase-locked loop therefore has the ability to efficiently reject random noise because its phase would vary with time and average to zero. This is particularly true for random noise at the chopper frequency since its time-dependence results in an AC signal to be suppressed by the filter. Some sources of random noise will be identified in Sect. 3.4.3.

3.4.2 Time Sequencing and Signal Averaging

Essentially, the chopper wheel convolutes the NIR pulse train with a periodic window function. The duration of each window in between consecutive blades is equal to the period of rotation divided by the number of blades. The number of laser pulses that can contribute to the signal collected by the LIA is then a function of both the chopping

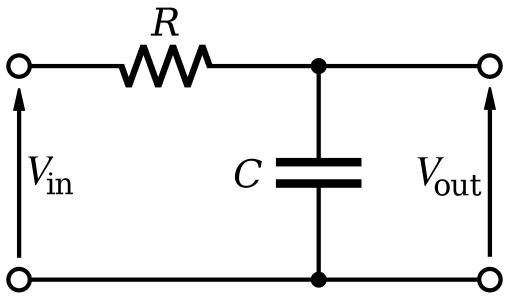

Figure 3.9: Simple schematic of a low-pass RC filter. The symbol V_{in} represents the voltage resulting from the difference signal produced by a phase-modulated NIR pulse impinging on the balanced photodetectors as shown in Fig. 3.5. The symbol V_{out} represents the output voltage. Adapted from [95].

frequency and the repetition rate of the laser. For this thesis, we tune the PHAROS laser to a fixed repetition rate of 1.1 MHz and use a chopping frequency of about 640 Hz which allows about 112 NIR pulses to pass per window. As a result, for each step of the translation stage, the LIA will take in the sum of the photocurrents produced by a set of identically-modulated NIR pulses impinging on the photodiodes.

As mentioned before, we use a LabVIEW program to control the timing sequence of the moving parts of the THz spectrometer. Remember in Sect. 3.4.1, we showed that every time a scan is performed with the THz spectrometer, one has to consider the trade-off between the total time one is willing to wait and the desired amount of signal averaging performed to reject electronic noise. For example, the trace we showed in Fig. 3.8 took about 4 minutes to complete. The time taken to measure each data point was mostly spent in the filtering stage of the LIA. Here, the input signal is passed through a series of identical low-pass RC filters whose basic constituent is shown in Fig. 3.9. The characteristic time constant $\tau_{RC} = RC$ defines the time needed to charge the capacitor to ~63% of its total amount. Waiting about $5\tau_{RC}$ settles the filter on its final value. Since these filters are stacked in the LIA, one typically waits an extra time constant to maximize the signal collected per data point. Additionally, the time constant sets the spectral bandwidth of the filter according to $\tau_{RC} = 1/2\pi f_{-3\text{ dB}}$[3]. Note that $f_{-3\text{ dB}}$ marks the frequency at which the output power is equal to half the input power and is determined by the transfer function of the filter. Passing the signal through multiple stages of RC filtering steepens the frequency roll-off of noise rejection at this point [96].

3.4.3 Intrinsic Noise Sources

The term noise signifies the presence of spurious voltages or currents interfering with our electrical signals. For example, random noise can enter into the measurement through intrinsic sources such as Johnson-Nyquist noise, shot noise and $1/f$ noise. Other noise sources of technical origin that depend on the electrical connections include ground loops, interference from the external environment, cross-talk, 60 Hz noise (and its harmonics) from AC mains and electro-magnetic pick-up [96]. In particular, we will focus on sources of noise that are intrinsic to measurement through lock-in detection.

[3]This expression is explicitly derived in [95].

First, we note that the quantity that determines the efficiency in noise rejection of a LIA is its dynamic reserve which is defined as the ratio of the largest tolerable noise level V_n to the maximum amplitude a system can attain V, also known as the full scale [97]:

$$\text{Dynamic Reserve [dB]} = 20\log_{10}\left(\frac{V_n}{V}\right). \tag{3.9}$$

For example, for a full scale of 1 μV, a dynamic reserve of 40 dB means that noise as large as 100 μV can be tolerated at the input without overloading the electronics. Modern LIAs can reach a dynamic reserve of 120 dB [96]. In other words, these devices can extract a signal in the presence of noise amplitudes up to 6 orders of magnitude higher than the signal itself! Before conducting the measurement, one chooses a dynamic range to reject a desirable amount of noise whilst providing amplification with enough headroom so that peaks in the signal do not overload the instrument. In practice, the acceptable level of noise is hard to specify beforehand and so the dynamic reserve is normally kept at a reasonable level to avoid detecting the output noise of the LIA itself.

As explained in 1928 by Nyquist [98], Johnson noise refers to thermal fluctuations in the electron density of a resistor of resistance R which generates a root-mean-square (RMS) voltage of:

$$V_n^{\text{Johnson}} = \sqrt{4k_BTR\Delta f_{\text{BW}}}, \tag{3.10}$$

where $k_B = 1.38\times10^{-23}$ V$^2/\Omega$ Hz K is Boltzmann's constant, T is temperature and Δf_{BW} is the frequency bandwidth of the measurement. At room temperature, Johnson noise is the dominant form of noise in the LIA and therefore is mainly responsible for the amount of dynamic reserve required. For instance, the differential voltage amplifier in our SR830m has a frequency bandwidth of about 300 kHz which corresponds to an effective noise at the amplifier input of $V_n^{\text{Johnson}} \approx 2.2$ μV_{rms} or about 11 $\mu\text{V}_{\text{pk-pk}}$ when our choice of a 1 kΩ terminal resistor is used [97]. Since Johnson noise is incoherent and relatively flat over all practical chopper frequencies, this noise is greatly suppressed when the LIA narrows its detection bandwidth after the phase-locked loop.

Shot noise originates from the non-uniformity of discrete events in nature. A coin flipped many times will on average land 50% of the time on heads while too few throws may show too many tails. Experimentally, one desires enough of these throws to build up the proper statistics but this comes at the cost of measurement time. Similarly, the analysis of electrons flowing in electrical currents and of photons contained in optical beams obey statistical distributions. The shot noise that arises from such independent random events is thus characterized by a Poisson distribution. In contrast, Johnson noise obeys a Gaussian distribution due to its proportionality to the square root of the frequency bandwidth within which the noise is measured. In our THz spectrometer, both the generation and gating arms display shot noise but the latter contribution is suppressed by the placement of the optical chopper in the generation arm. On the other hand, the balancing of our detection optics is prone to suffer from the shot noise in the gating beam which causes the Wollaston polarizer to separate an unequal amount of photons and passes this noise on to the LIA. Electro-optic detection routinely operates at the shot noise limit, although spectral post-filtering can be performed to reduce the noise even further [99]. For example, in 2002, Planken *et al.* presented a noise analysis with which to compare different THz spectrometers based on electro-optic detection [100]. Their calculations showed that the sensitivity of their setup was ultimately limited by the quantum shot noise of their gating pulses. Soon after, Abbot *et al.* outlined a general theoretical analysis which supported

this conclusion by weighing contributions to the shot noise from each of the typical THz sources over long scan times [101]. More recently, Leitenstorfer *et al.* have used the high sensitivity afforded by electro-optic detection to sample non-destructively the electric-field variance of vacuum fluctuations [102]. We verified that our detection scheme was shot noise limited by repeating scans as a function of the power of the gating beam, the results of which are not given. Fundamentally, the noise level of our THz system is fixed by the polarization extinction ratio of our Wollaston polarizer which is at best 100,000:1 or -50 dB if properly configured.

Since shot noise is so fundamental to our detection scheme, we now illustrate what happens when a shot in the form of a gating pulse triggers a signal. The following simple analysis can be found in most university-level electronics laboratory experiments, in particular we take inspiration from Ref. [103]. We know that light impinging on a photodiode excites electrons into the conduction band which then succumb to the local electric field in the depletion region and drive a current. For an average of N electrons produced in a time interval τ, the average current generated will be:

$$I_{\text{ave}} = \frac{Ne}{\tau}, \tag{3.11}$$

where e is the electron charge. The passage of each electron across the depletion region is a random event. We will then treat τ as large enough to assume that the number of electrons produced in consecutive time intervals are statistically independent. By Poisson statistics, the variance of the quantity N is also its mean, N, therefore a component of this current I_{fluc} will fluctuate in proportion as [93]:

$$I_{\text{fluc}}^2 = \frac{I_{\text{ave}}e}{\tau}, \tag{3.12}$$

The pulse of current produced by a single electron will decay due to the inductance in the circuit. Over the time interval τ, the total current produced will be a result of the superposition of many such pulses initiated at random times. Fourier analysis, such as that presented in Ref. [104], then reveals that:

$$I_{\text{fluc}}^2 = 2I_{\text{ave}}e\Delta f_{\text{BW}}, \tag{3.13}$$

where Δf_{BW} is the frequency bandwidth of the measurement, as before. In our case, we pass the current from the illuminated photodiode through a load resistor and therefore the average voltage across this resistor is simply $V_{\text{ave}} = I_{\text{ave}}R$, following the same statistics. Therefore, the amount of shot noise in our measured signals depends on the square root of the signal.

Both Johnson noise and shot noise are instances of white noise since they have relatively equal intensity at each frequency. On the other hand, the power spectral density of another prominent source of intrinsic noise related to electronic detection is defined by its $1/f$ dependence. For semiconductors and metals, this noise arises as a fluctuation in the bulk conductance due to the passage of current [105], although the exact sources of $1/f$ noise are widely debated. Figure 3.10 shows a qualitative noise spectrum for a typical experiment where lock-in detection is performed [96]. White noise from Johnson or shot noise creates a consistent layer across all frequencies while $1/f$ noise dominates at low frequencies and as such is usually referred to as pink noise. From the two possible chopper frequencies shown in Fig. 3.10, choosing the higher frequency at f_2 is optimal since it lies in a cleaner

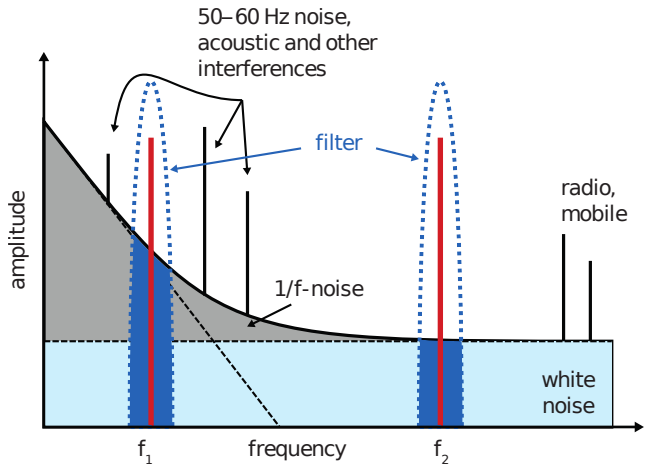

Figure 3.10: Illustration of a qualitative noise spectrum for a typical experiment performed using lock-in detection. Adapted from [96].

region above the $1/f$ noise and far from noise from technical sources. Finally, the total noise in the experiment is the square root of the sum of the squares of each of the discussed incoherent electronic sources. As noted, shot noise from the optical beams is coherent and will ultimately pass the noise rejection provided by the LIA.

3.4.4 Dual Phase-Sensitive Detection using a Lock-In Amplifier

In Sect. 3.4.1, we found that the signal output by the PSD depended on the relative phase θ of its reference oscillator to the measured modulated signal. To circumvent this phase dependence, LIAs bring the input signal through a second PSD configured to the same reference but passed through a 90° phase shifter. The resulting signal output by this PSD followed by the low-pass filter are simply:

$$V_{\mathrm{PSD2}}(t) = V_{\mathrm{s}} V_{\mathrm{r}} \sin(\omega_{\mathrm{chop}} t + \theta_{\mathrm{s}}) \cos(\omega_{\mathrm{LO}} t + \theta_{\mathrm{r}}) \tag{3.14}$$

$$\langle V_{\mathrm{PSD}} \rangle = \frac{V_{\mathrm{s}} V_{\mathrm{r}}}{2} \sin\left(\theta_{\mathrm{s}} - \theta_{\mathrm{r}}\right) \tag{3.15}$$

The two filtered outputs by the PSDs can be interpreted as a vector with components:

$$X = V_s \cos(\theta) \tag{3.16}$$

$$Y = V_s \sin(\theta), \tag{3.17}$$

where X is called the in-phase component and Y the quadrature component relative to the reference signal, since $Y = 0$ when $\theta = 0$. The magnitude of this vector gives the input signal amplitude V_s:

$$R = \sqrt{X^2 + Y^2} = V_s \tag{3.18}$$

and the relative signal phase:

$$\theta = \tan^{-1}\left(\frac{Y}{X}\right) \tag{3.19}$$

In practice, once the THz spectrometer is aligned, the Auto Phase button on the LIA is pressed to attempt to zero the Y component with a specific choice of phase and thereby put

all the signal into the X. However, the presence of noise can make this process imprecise and can afterwards be read as the fluctuations in Y. One then approximates the signal-to-noise ratio (SNR) from the displayed values of the in-phase and quadrature components of the signal:

$$\mathrm{SNR} = \frac{X}{Y}. \tag{3.20}$$

Ordinarily, one achieves experimentally a SNR of about 100 before performing a scan of the THz spectrometer.

3.5 Estimation of the Peak THz Field Strength

Recall that in Sect. 2.3.2, we discussed our electro-optic detection technique in the time domain. Our derivation arrived at an expression for the measured intensity imbalance due to the THz field-induced Pockels effect on a NIR probe. Note that the voltages measured by our LIA are proportional to the intensity of the light absorbed by the balanced photodetectors. Therefore, we can now use the derived eq. 2.81 to estimate the peak strength of the THz electric field $E_{\mathrm{THz,pk}}$ from the earlier measurement in Fig. 3.8. Recall that the detection medium was a (110)-oriented GaP crystal of thickness $d = 200$ μm. For easy reference, eq. 2.81 is reproduced below:

$$\Delta I(t, \omega, \alpha, \psi) = I_p \frac{\omega d}{c} \frac{n_O(\omega)^3 r_{41} |\vec{E}_{\mathrm{THz}}(t)|}{2} \Big(\cos(\alpha)\sin(2\psi) + 2\sin(\alpha)\cos(2\psi) \Big).$$

In order to do this estimation, we need to make some assumptions. First, we assume that we maximized the signal when we optimized the alignment of our THz spectrometer. As noted in Sect. 2.3.2, this means that we have set the orientation of the nonlinear media such that the polarizations of the THz and NIR fields are either perfectly parallel or orthogonal when they arrive at the THz detector. Second, we will consider the THz-induced phase modulation only for the central wavelength of $\lambda_0 = 1035$ nm of our NIR pulses. Third, we assume that the quantum efficiencies of our photodiodes and LIA are 100% so that the measured voltages are directly proportional to the intensities of the incident and absorbed NIR light. Finally, the phase-modulated NIR beam suffers Fresnel loss in amplitude at the exit of the weakly-absorbing detection medium by a factor of:

$$t_{\mathrm{GaP}}^{\mathrm{exit}} = 2n(\lambda_0)/(n_{\mathrm{air}} + n(\lambda_0)) \approx 1.5. \tag{3.21}$$

From these assumptions and using eq. 3.20, we have simplified the previously derived eq. 2.81 down to:

$$\frac{V_A - V_B}{V_A + V_B} = \frac{2\pi d n(\lambda_0)^3 r_{41} E_{\mathrm{THz,pk}} t_{\mathrm{GaP}}^{\mathrm{exit}}}{\lambda_0}. \tag{3.22}$$

For the voltage sum $V_A + V_B$ we take the maximum absolute value from Fig. 3.8 which was about 221.5 μV. We approximate the difference by calculating the standard deviation of the noisy signal beyond the edges of the THz transient as $V_A - V_B = 2.5$ μV. From eq. 3.22, we calculate a peak THz field strength of $E_{\mathrm{THz,pk}} \approx 2.3$ kV/cm.

Note that if we wanted to know the peak field strength at the position of the intermediate focus where a sample would be placed, we would need to account for the Fresnel losses of the fields entering the detection medium as well as the passage of the THz electric

field through the Si filter, which ideally has been set to Brewster's angle. Furthermore, since THz-induced nonlinearities come into effect for much higher field strengths on the order of many hundreds of kV/cm [106], we are well within the linear operating range of our detection scheme.

3.6 Comparison of the Numerical Simulation to Measurement

Our analysis in Chapter 2 presented an idealized scheme of THz generation and detection which should be reconciled with the experimental considerations outlined in this chapter. In practice, from generation to detection, each component of the THz spectrometer introduces some amount of frequency-dependent loss due to either material dispersion or geometry. For example, every parabolic mirror collects the incident THz radiation only over a finite numerical aperture beyond which the light is lost. Assuming a well-aligned setup, this loss is most significant for the first and final parabolic mirrors which serve respectively to collect the generated THz pulses and to overlap them with time-synchronized NIR pulses for electro-optic detection. In principle, a careful analysis could be performed to walk back through each stage of the THz spectrometer and calculate the evolving shape of the THz transient. A few analytical models have been presented in the literature [107, 108]. Using transfer function formalism, they arrive at a simple expression for the expected measured THz spectra from a typical THz spectrometer:

$$E_{\mathrm{THz}}^{\mathrm{meas}}(\Omega) = T_{\mathrm{setup}}(\Omega) E_{\mathrm{THz}}^{\mathrm{gen}}(\Omega), \tag{3.23}$$

where $T_{\mathrm{setup}}(\Omega)$ is a comprehensive transfer function that seeks to account for all of the frequency-dependent loss in the experimental setup. In reality, this transfer function contains a variety of fixed experimental parameters specific to each THz spectrometer such as the bandwidth and central frequency of the NIR gating beam and the numerical aperture and f-number of the parabolic mirrors.

Let us now directly compare the results predicted from our simulation with a measured signal. Figure 3.11 overlays the calculated spectrum from the simulation using a 200 μm thick (110)-oriented GaP crystal as both the THz emitter and the detector with the corresponding measured spectrum shown before in Fig. 3.8 with the same crystals. For the simulation, the NIR amplitude bandwidth at FWHM was adjusted to $\sigma_{\mathrm{FWHM}} = \sqrt{2} \times 3.6 = 5.1$ THz to better emulate the PHAROS laser. From this figure, we see that a common peak frequency of 2.0 THz which indicates that the phase-matching aspects of our analysis were accurate.

However, in Fig. 3.11 it is also apparent that the simulation appears to overestimate the amount of low and high frequency THz components compared to the measurement. One possible reason for this discrepancy is that our idealized model does not address beam diffraction and instead assumed plane wave propagation. In order to reach experimentally the high intensities demanded by nonlinear optics, we generate and detect our THz pulses using focused NIR pump and gating beams. Knowing that the generation of the THz field depends on the NIR pump intensity, one may assume that all of the THz field components are generated by a spot size of $w_{\mathrm{THz}} = w_{\mathrm{pump}}/\sqrt{2}$, where w_{pump} is the focused beam diameter of the NIR pump. The THz field then quickly spreads out from this focus before

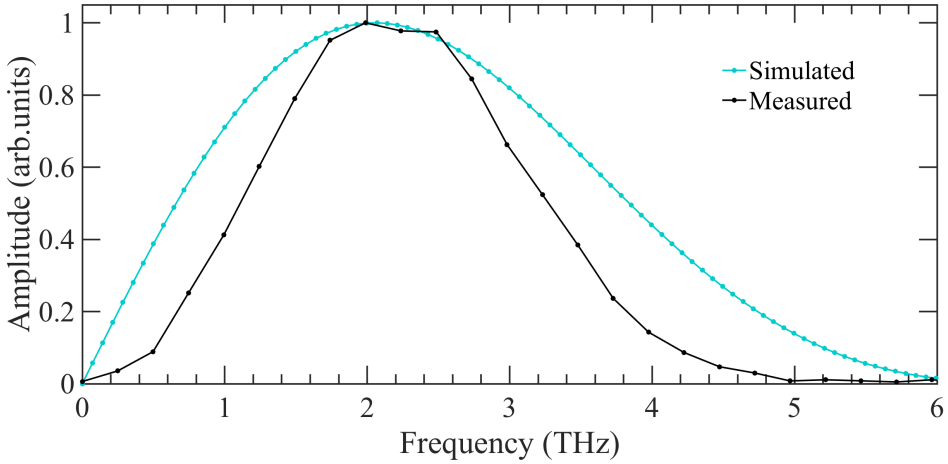

Figure 3.11: Simulated and measured results for the THz amplitude spectrum generated by a 200 μm thick (110)-oriented GaP crystal and detected by an identical crystal.

being collected by the first parabolic mirror in the far field. Recent literature has found that the low THz frequency components diverge faster than predicted by the usual paraxial approximation and can be modelled instead by Bethe theory [107]. Similarly, the role of the final parabolic mirror is to bring the THz field to a focus on a nonlinear detection medium. Therefore, wherever the THz beam is collimated or brought to a focus, the size of the THz field components will vary depending on their frequency. In particular, this frequency dependence manifests during electro-optic detection as a bias for the field components of a size comparable to or less than that of the gating beam for which there is better spatial overlap. Additionally, we recall from Sect. 2.3.3 that electro-optic sampling introduces another factor of frequency dependence through the spectral autocorrelation of the NIR gating beam. All together, the transfer function describing the setup takes at least the following terms:

$$T_{\text{setup}} \equiv T_{\text{FP}} T_{\text{Diff}} T_{\text{Foc}} T_{\text{EOS}} T_{\text{overlap}}, \tag{3.24}$$

where T_{FP} accounts for the Fresnel loss from the Fabry-Perot effect that arises from transmission through the optics and the factors T_{Diff} and T_{Foc} arise from each pair of parabolic mirrors. By numerically setting the frequency resolution of the simulation equal to that of the measurement and dividing the two normalized spectra, we obtain the transfer function shown in Fig. 3.12. This function peaks at around 2.0 THz as expected and drops off at higher and lower THz frequencies due to the limitations outlined above.

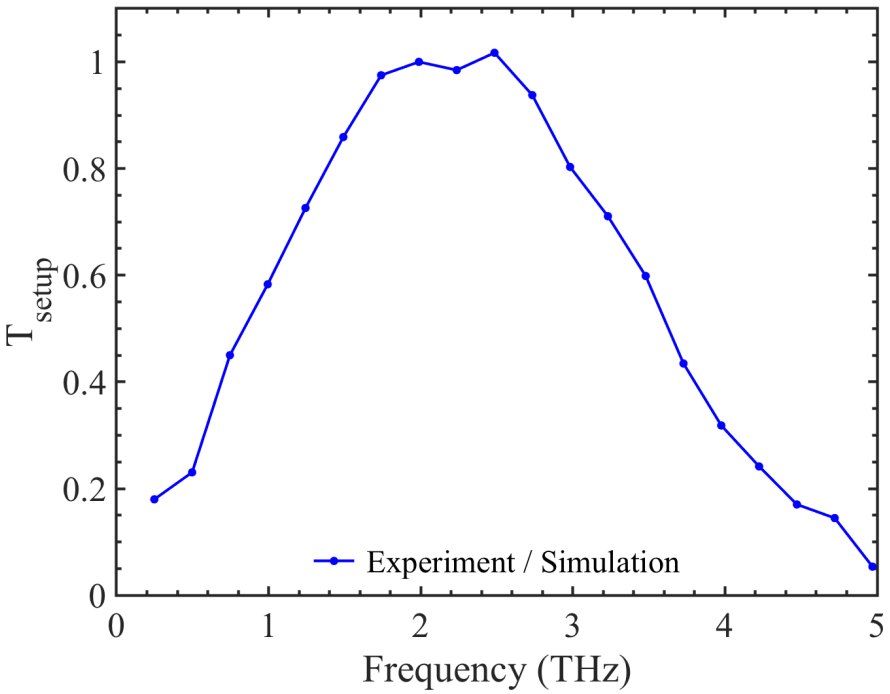

Figure 3.12: Comprehensive transfer function corresponding to the ratio of the experimentally measured to the simulated results shown in Fig. 3.8.

Chapter 4

Transmission Mode Terahertz Time-Domain Spectroscopy

This chapter outlines our procedure for extracting the optical properties of a sample material in the THz range from our measured signals using the technique of terahertz time-domain spectroscopy (THz-TDS). The technique requires the acquisition of at least two signals, one in the presence of the sample and a reference in its absence. Since electro-optic detection is sensitive to the electric field of a THz pulse, a numerical Fourier transform is performed on these signals to convert their amplitude and phase information into the frequency domain. An experimental transfer function is then obtained by taking the ratio of the transformed signals. This process is also known as deconvolution since it is used to isolate the effect of the sample on the propagating THz pulses from the reference background [109]. Similarly, the transfer function can be modelled based on the propagation of plane waves to describe the dispersive and absorptive properties of the sample under study. This theoretical model accounts for the loss in spectral amplitude at each interface of the sample as described by the Fresnel coefficients as well as the frequency-dependent phase developed by each THz pulse during propagation. Under the assumption that our samples are weakly absorbing of THz radiation, we equate the experimental and theoretical transfer functions and find simple expressions for the real and imaginary parts of their complex refractive indices as a function of frequency. The experimental phase difference between the two signals determines the real part of the refractive index which goes on to aid in the determination of the imaginary part from the change in amplitude. Stating the material parameters in the form of the complex refractive index is sufficient for our study since it is straightforward to relate these variables to other equivalent complex quantities such as the optical conductivity or the dielectric function.

It is worthwhile to note that the schematic of our THz spectrometer presented earlier in Fig. 3.5 shows that we conduct THz-TDS in transmission mode. Additionally, the THz beam path is entirely contained within an atmosphere purged of moisture by nitrogen gas which otherwise is highly absorptive of THz radiation [110]. In this configuration, the THz pulses are made to propagate before their detection through a sample that has been placed at an intermediate focus where high spatial resolution is achieved. We will assume that the front and back surfaces of our samples are planar and devoid of roughness on the scale of the wavelengths in our THz pulses so that we may neglect scattering effects. Like any other electromagnetic wave crossing an interface between two different media, each THz pulse will fractionate into a reflected and a transmitted pulse with strengths in proportion

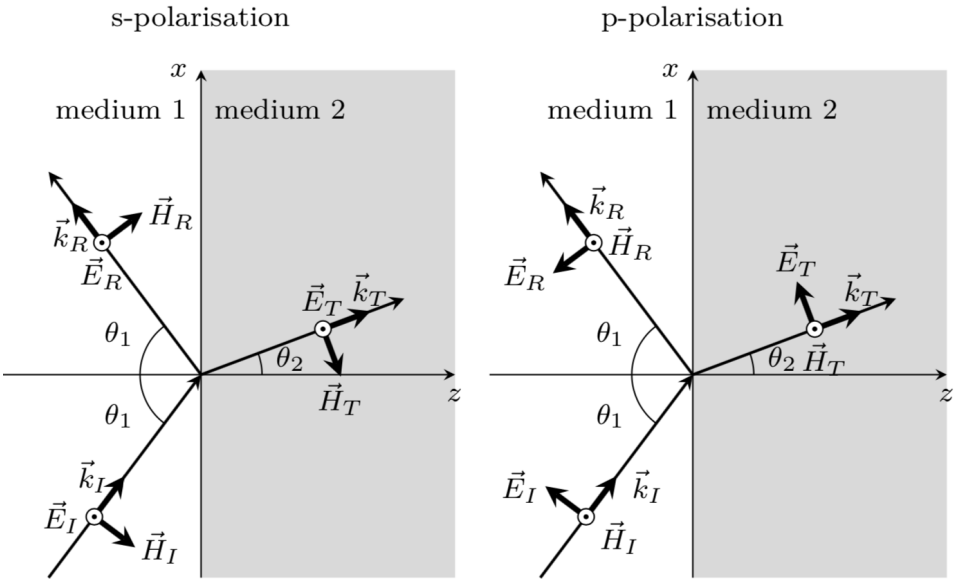

Figure 4.1: Diagrams showing the transmission and reflection of an incident electromagnetic wave with either *s*- or *p*-polarization due to crossing an interface between two different media. Adapted from [112].

to the Fresnel coefficients. Alternative geometries utilize the first THz pulse reflected by the air-to-sample interface. However, unlike for transmission setups, THz-TDS conducted in this reflection mode obtains its reference signal by replacing the sample by a conductive mirror and can suffer from phase correction issues even if the mirror is misaligned by only several micrometers [111]. Our samples weakly absorb THz radiation, therefore our use of the transmission mode geometry is optimal. Even so, a sufficiently thick sample can still significantly narrow the spectral content of the transmitted THz pulses and limit the frequency range accessible to the experiment. In this chapter we present experimental determinations of the complex refractive indices of the zinc-blende semiconductors GaP and ZnTe.

4.1 Theory of Transmission and Reflection

In order to analyse the dispersive and absorptive effects of the investigated sample, we first need to consider the theory of an incident electromagnetic wave crossing an interface between two different media as shown by Fig. 4.1. The interface divides the wave in two: one component is reflected back into the first medium and another is transmitted into the second medium. The well-known law of reflection states that the angle of reflection is equal to the angle of incidence such that $\theta_I = \theta_R \equiv \theta_1$. In addition, the transmitted component obeys Snell's law of refraction:

$$n_1 \sin\theta_1 = n_2 \sin\theta_2 \tag{4.1}$$

where n_1 and n_2 are the real parts of the refractive indices of the two media and θ_2 is the angle of refraction. Since light is a transverse wave, we need to distinguish between two possible polarizations of the incident field. By convention, the incident electric field is

decomposed into two orthogonal components:

$$\vec{E}_I = E_s \hat{s} + E_p \hat{p}, \tag{4.2}$$

where the s-polarization corresponds to the field component perpendicular to the plane of incidence formed by the incident wave-vector $\vec{k}_I$ and the vector normal to the interface that points in the $\hat{z}$ direction. The p-polarization takes the complementary direction parallel to the plane of incidence. For our discussion, the relevant boundary conditions imposed by Maxwell's equations (see Sect. 2.1) are that the tangential components of both the electric field $\vec{E}$ and the magnetic flux density $\vec{H}$ (in the absence of surface current) must be continuous at the interface at $z = 0$. As illustrated in Fig. 4.1, for an incident wave that is p-polarized these conditions become:

$$E_{I,p}(z=0)\cos\theta_1 - E_{R,p}(z=0)\cos\theta_1 = E_{T,p}(z=0)\cos\theta_2 \tag{4.3}$$

$$H_{I,p}(z=0) + H_{R,p}(z=0) = H_{T,p}(z=0). \tag{4.4}$$

In a medium of permeability μ, the magnetic and electric field strengths are related by $H = \frac{n}{c\mu}E$. Assuming nonmagnetic media such that $\mu_1 = \mu_2 = \mu_0$, plugging this relation into eq. 4.4 gives:

$$n_1(E_{I,p} + E_{R,p}) = n_2 E_{T,p}, \tag{4.5}$$

which in combination with eq. 4.3 leads to the following definitions:

$$r_p \equiv \frac{E_{R,p}}{E_{I,p}} = \frac{n_2\cos\theta_1 - n_1\cos\theta_2}{n_2\cos\theta_1 + n_1\cos\theta_2} \tag{4.6}$$

$$t_p \equiv \frac{E_{T,p}}{E_{I,p}} = \frac{2n_1\cos\theta_1}{n_2\cos\theta_1 + n_1\cos\theta_2}. \tag{4.7}$$

These expressions are called the Fresnel coefficients for an incident electric field that is p-polarized. They determine the fraction of incident electric field strength split into the reflected (r_p) or transmitted (t_p) waves. A similar derivation leads to the following expressions for s-polarized light:

$$r_s \equiv \frac{E_{R,s}}{E_{I,s}} = \frac{n_1\cos\theta_1 - n_2\cos\theta_2}{n_1\cos\theta_1 + n_2\cos\theta_2} \tag{4.8}$$

$$t_s \equiv \frac{E_{T,s}}{E_{I,s}} = \frac{2n_1\cos\theta_1}{n_1\cos\theta_1 + n_2\cos\theta_2}. \tag{4.9}$$

At normal incidence, we have $\theta_1 = 0 = \theta_2$ and these expressions reduce simply to:

$$r \equiv r_s = \frac{n_1 - n_2}{n_1 + n_2} = -r_p \tag{4.10}$$

$$t \equiv t_s = \frac{2n_1}{n_1 + n_2} = t_p. \tag{4.11}$$

We therefore define t_{12} as the transmission coefficient for the electric field crossing from medium 1 to medium 2 and likewise for the reflection coefficient.

Moisture-free air surrounds our optical components so we can neglect the absorption of our THz pulses in the purged environment and set $n_1 = n_{\text{air}}$. In our experiment, the second medium will be the sample under study and we must consider the complex nature of its refractive index, for which we use the following convention:

$$\tilde{n}_2 \equiv \tilde{n} = \mathbb{R}[\tilde{n}(\Omega)] + i\mathbb{I}[\tilde{n}(\Omega)] \equiv n(\Omega) + i\kappa(\Omega). \tag{4.12}$$

For all of our measurements, every THz pulse we generate through optical rectification must pass first through a Ge wafer to remove any residual NIR pump light and then through a Si wafer to recombine with a NIR gating pulse for electro-optic detection. As we know, a THz pulse passing through one of these optical components will produce a weaker replica of itself. For example, after entering the Ge wafer, a back-reflection is created at the exit interface which can then undergo several successive reflections off of each interface. Assuming normal incidence, every time one of these THz pulses reaches the exit interface, a fraction of it is transmitted and joins the THz pulse train. Each one of these pulse replicas propagates an additional distance equal to twice the thickness of the medium and becomes further delayed in time by an amount ΔT:

$$\Delta T = (n_g(\Omega) - n_{\text{air}})\frac{d}{c}. \tag{4.13}$$

Our Ge wafer has a thickness specified by the manufacturer of $d_{\text{Ge}} = 500$ μm and its refractive index is approximately flat in the THz range at about 4.0 [113]. We therefore expect the echo appearing at 5.0 ps in Fig. 4.2 to be a result of our Ge wafer. Furthermore, we know that each consecutive echo is weaker than the last until eventually being shrouded in the noise. The echo of the main THz transient produced from the Ge wafer has suffered loss from reflection, transmission and absorption in the wafer which totals to a factor of:

$$t_{\text{air,Ge}}\, t_{\text{Ge,air}} \times r_{\text{Ge,air}}\, r_{\text{air,Ge}} \times \mathrm{e}^{-\alpha_{\text{Ge}} d_{\text{Ge}}/2} \approx 22\%$$

Since our THz detector in this measurement was a 1 mm thick (110)-oriented GaP crystal, we can isolate the loss due to the Ge wafer alone by dividing by its loss factor of:

$$t_{\text{air,GaP}}\, t_{\text{GaP,air}} \times \mathrm{e}^{-\alpha_{\text{GaP}} d_{\text{GaP}}/2} \approx 68\%$$

which gives a value of 33% in support of the observed fraction of about 30% of the main peak. For these calculations, the power absorption coefficients in the THz range for Ge and GaP respectively are taken as the experimentally measured values $\alpha_{\text{Ge}} \approx 1.5$ cm^{-1} and $\alpha_{\text{GaP}} \approx 4.0$ cm^{-1} [113, 61]. Similarly, our THz detector is responsible for the second echo of the main THz transient appearing at 8.0 ps in Fig. 4.2.

4.2 Theory of Material Parameter Extraction from Measured Signals

Figure 4.3 shows that each pulse transmitted through the exit interface of an optical component will not only leave at a delayed time but also with a smaller amplitude due to the multiplication of Fresnel coefficients. Recall that we can use plane wave representation for each spectral component of the incident electric field of a THz pulse by its amplitude $S(\Omega)$ multiplied by an exponential phase factor:

$$\tilde{E}_I(\Omega) = S_I(\Omega)\ \mathrm{e}^{i\psi_I(\Omega)} \tag{4.14}$$

In Fig. 4.3(a), we see that every pulse picks up Fresnel loss due to the product of the transmission coefficients $t_{12}t_{21}$ and every successive reflected pulse takes on an additional pair of reflection coefficients $r_{21}r_{12}$. The spectral phase of each pulse component $\psi(\Omega)$ evolves as a function of the number of times the pulse has traversed the medium. In

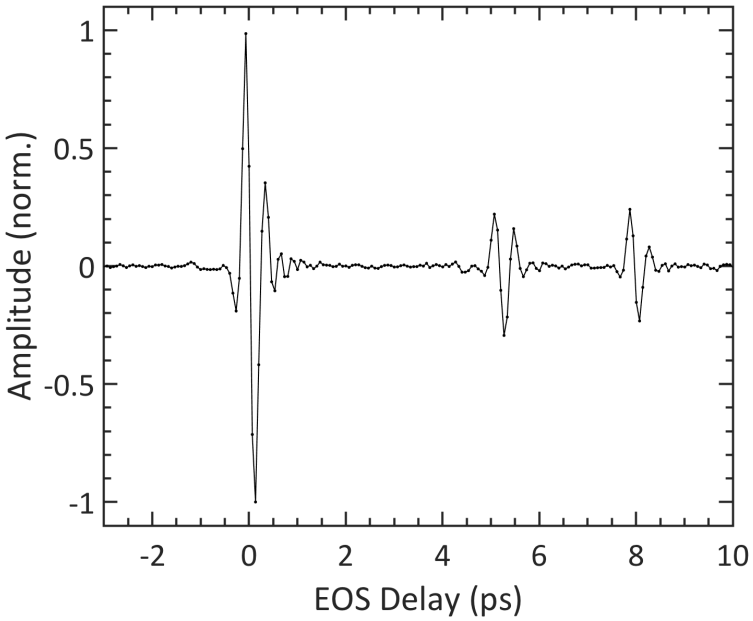

Figure 4.2: Example of a long scan of our THz spectrometer showing the appearance of pulse echoes that result from Fresnel reflection from optical components within the THz beam path. In the text, we ascribe the echo at 5.0 ps to our Ge wafer and the one at 8.0 ps to our THz detector, a 1 mm thick GaP crystal.

Fig. 4.3, the integer N indexes the order of transmitted pulses. The spectrum of the first transmitted pulse is then:

$$\tilde{E}_1(\Omega) = t_{12}(\Omega)t_{21}(\Omega)\ \mathrm{e}^{i\tilde{k}(\Omega)d}\tilde{E}_I(\Omega). \tag{4.15}$$

Assuming that the sample is weakly absorbing, $\tilde{n}(\Omega) \approx n(\Omega)$, the Fresnel transmission coefficients become:

$$t_{12}(\Omega) = \frac{2n_{\mathrm{air}}}{n_{\mathrm{air}} + n(\Omega)} \tag{4.16}$$

$$t_{21}(\Omega) = \frac{2n(\Omega)}{n(\Omega) + n_{\mathrm{air}}} \tag{4.17}$$

We often numerically truncate the data to include only the main THz transient in order to remove the influence of any reflections which would otherwise show up as oscillations in the results. Therefore, eq. 4.15 corresponds to the spectrum of the measurement we perform in the presence of the sample. Similarly, the spectrum of the reference measurement without the sample is:

$$\tilde{E}_{\mathrm{air}}(\Omega) = \ \mathrm{e}^{ik_{\mathrm{air}}d}\tilde{E}_I(\Omega). \tag{4.18}$$

The sample absorbs and also imparts dispersion to the propagating THz pulse, which are linear and time-invariant effects, therefore we may express its influence on the pulse theoretically through a frequency-dependent transfer function $\tilde{G}_{\mathrm{theory}}(\Omega, \tilde{n})$, which relates the input and output fields via:

$$\tilde{E}_1(\Omega) = \tilde{G}_{\mathrm{theory}}(\Omega, \tilde{n})\tilde{E}_{\mathrm{I}}(\Omega). \tag{4.19}$$

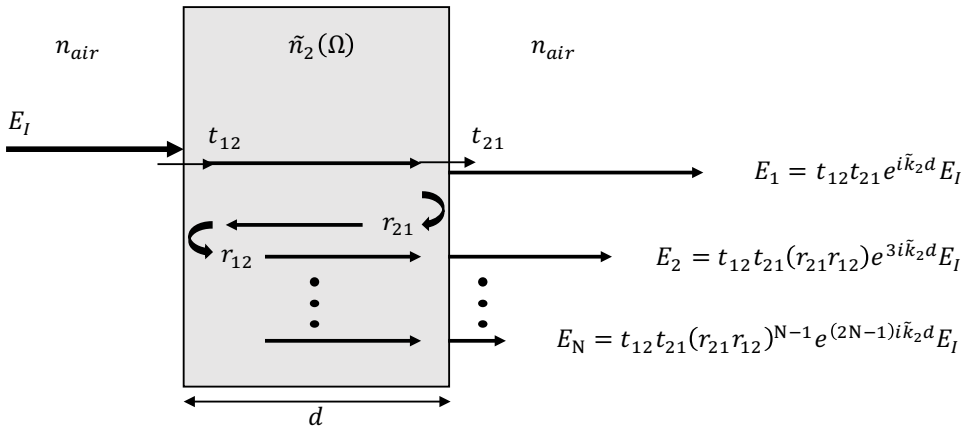

(a) Measurement in the presence of the sample.

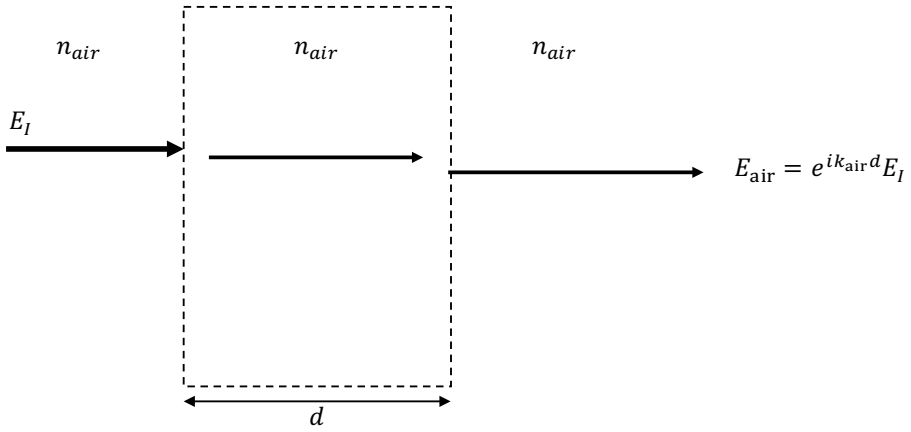

(b) Measurement in the absence of the sample.

Figure 4.3: Diagrams showing the measurements performed with or without the sample. (a) In the presence of the sample, the Fabry-Perot effect leads to weaker, delayed replicas of the incident pulse whose strengths are determined by the multiplicative Fresnel coefficients as shown. (b) In the absence of the sample, the pulse simply propagates through air instead.

Next, we apply deconvolution by dividing both sides by the spectrum of the reference measurement in air and solve for the theoretical transfer function:

$$\tilde{G}_{\mathrm{theory}}(\Omega, \tilde{n}) = \frac{\tilde{E}_1(\Omega)}{\tilde{E}_{\mathrm{air}}(\Omega)}. \tag{4.20}$$

$$= \frac{4n_{\mathrm{air}}n(\Omega)}{(n(\Omega)+n_{\mathrm{air}})^2}\ \mathrm{e}^{i\tilde{k}(\Omega)d}\ \mathrm{e}^{-ik_{\mathrm{air}}d} \tag{4.21}$$

$$= \frac{4n_{\mathrm{air}}n(\Omega)}{(n(\Omega)+n_{\mathrm{air}})^2}\ \mathrm{e}^{-\alpha(\Omega)\frac{d}{2}}\ \mathrm{e}^{i(n(\Omega)-n_{\mathrm{air}})\frac{d}{c}} \tag{4.22}$$

where the power absorption coefficient is defined as $\alpha(\Omega) \equiv 2\kappa(\Omega)\Omega/c$.

In the reference measurement, the THz transient has propagated through an extra distance of air equal to the thickness of the absent sample. Therefore, dividing the sample

measurement by the reference spectrum isolates the effect of the sample from any dependence on the incident field predicted by eq. 4.19. We may perform the same action numerically on experimentally measured signals by dividing their spectra that we obtain by Fast Fourier Transform:

$$\tilde{G}_{\text{exp}}(\Omega) = \frac{\tilde{E}_{\text{sam}}(\Omega)}{\tilde{E}_{\text{ref}}(\Omega)} \tag{4.23}$$

$$= \frac{S_{\text{sam}}(\Omega)\ \mathrm{e}^{i\psi_{\text{sam}}}}{S_{\text{ref}}(\Omega)\ \mathrm{e}^{i\psi_{\text{ref}}}} \equiv m(\Omega)\ \mathrm{e}^{i\Delta\psi(\Omega)} \tag{4.24}$$

where the ratio of the spectral amplitudes m and the spectral phase difference $\Delta\psi$ are:

$$m(\Omega) \equiv S_{\text{sam}}(\Omega)/S_{\text{ref}}(\Omega) \tag{4.25}$$

$$\Delta\psi(\Omega) = \psi_{\text{sam}}(\Omega) - \psi_{\text{ref}}(\Omega). \tag{4.26}$$

The phase relationship after equation the experimental and theoretical transfer functions leads to an expression for the real part of the refractive index of the sample:

$$n(\Omega) = n_{\text{air}} + \frac{\Delta\psi(\Omega)c}{\Omega d} \tag{4.27}$$

In turn, the imaginary parts of the transfer functions result in an expression for the absorption coefficient:

$$\alpha(\Omega) = -\frac{2}{d}\ln\left(\frac{(n(\Omega)+n_{\text{air}})^2}{4n_{\text{air}}n(\Omega)}m(\Omega)\right) \tag{4.28}$$

which requires the real part of the refractive index previously calculated in eq. 4.27.

4.3 Demonstration of Material Parameter Extraction for a GaP Sample

Here we present our first use of THz-TDS to extract the material properties of a (110)-oriented GaP crystal that has a manufacturer-specified thickness of 400 μm. A major motivation for this experiment is to better understand the widespread use of GaP as a source or detector of THz radiation. In fact, we use an crystal identical to the sample derived from the same wafer as the THz emitter for this measurement in addition to one that is only 200 μm thick as the THz detector. However, a Vernier calliper used to measure the thickness of the sample gives a reading of 310 μm with an accuracy of 10 μm. From the model presented in Sect. 2.2, this 100 μm discrepancy means the difference between generating a phase-matched bandwidth of up to 5.6 THz (if 400 μm is correct) or to 6.1 THz (for 310 μm) with this crystal. For another independent measurement of the sample thickness, we perform an additional scan of the THz spectrometer with the sample placed in the gating arm. Figure 4.4 shows this measurement along with the two other sample and reference measurements. Rearranging eq. 4.13 for the unknown thickness d and using the well-known NIR group refractive index gives:

$$d = \frac{c\Delta T_{\text{GaP}}}{n_g(\lambda_0) - n_{\text{air}}}. \tag{4.29}$$

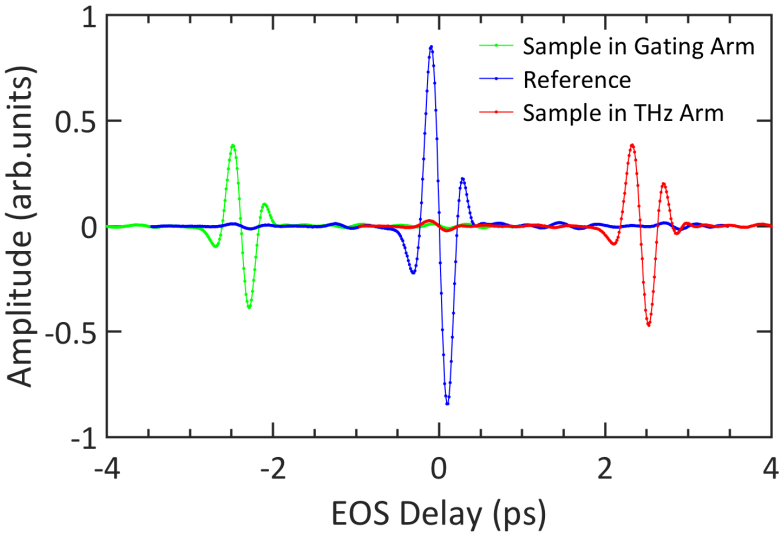

Figure 4.4: Measured traces with our THz spectrometer under the conditions of the reference measurement (blue), the sample measurement (red) and the additional thickness measurement (green).

The observed group delay of about -2.4 ps corresponds to a sample thickness of 312 μm, in agreement with the calliper measurement. The frequency spectra of the sample and reference measurements are given in Fig. 4.5 showing that the presence of the sample cuts the signal amplitude by about half. Note that we have used MATLAB to apply some post-processing on the data in order to cut out the echoes that appear in the traces. Briefly, the data outside of a rectangular window positioned over the main THz transients was set to zero and additional zero-padding was performed using MATLAB's `fft()` command. Next, the spectral phase information is obtained for each transformed signal via its complex argument:

$$\psi(\Omega) = \arg\left(\tilde{E}(\Omega)\right) = \arctan\left(\frac{\mathbb{R}[\tilde{E}(\Omega)]}{\mathbb{I}[\tilde{E}(\Omega)]}\right) \tag{4.30}$$

using MATLAB's `angle()` command. The periodic nature of the arctan function will wrap the phase to within the range $[-\pi, \pi]$. In order to calculate the refractive index properly and correct for this discontinuous behaviour, we use a numerical phase unwrapping algorithm as exemplified in Fig. 4.6 for the reference measurement. Next, the real part of the refractive index and the power absorption coefficient are calculated using eqs. 4.27 and 4.28 as shown in Fig. 4.7. There is a average difference between the accepted literature model and the calculated real part of the refractive index of our GaP sample of about -0.05. Meanwhile, we observe high absorption at low THz frequencies, peaking at around 1 THz, likely attributable to a plasmonic resonance formed by the presence of free charge carriers that were created by doping agents during the fabrication of the sample. Interestingly, the manufacturer specifications list the sample as undoped in disagreement with our phase-sensitive detection scheme. Unfortunately, the literature is lacking in THz-TDS experiments performed on GaP with which to compare our results.

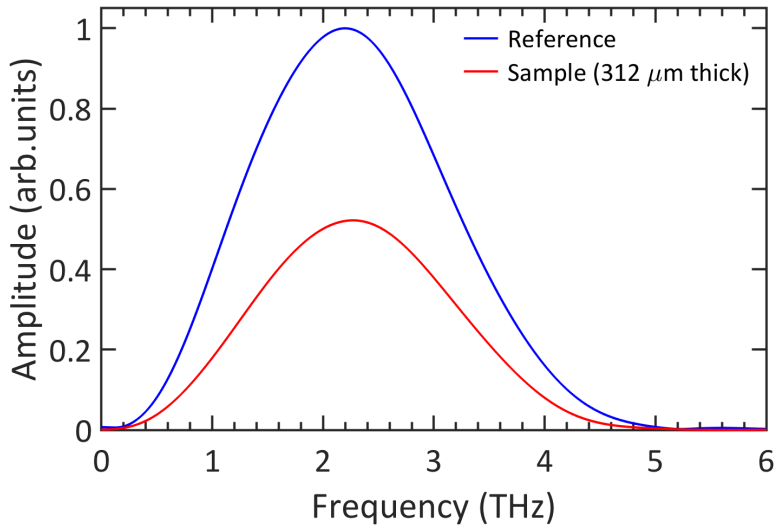

Figure 4.5: Spectra calculated by Fast Fourier Transform corresponding to the measured traces in Fig. 4.4.

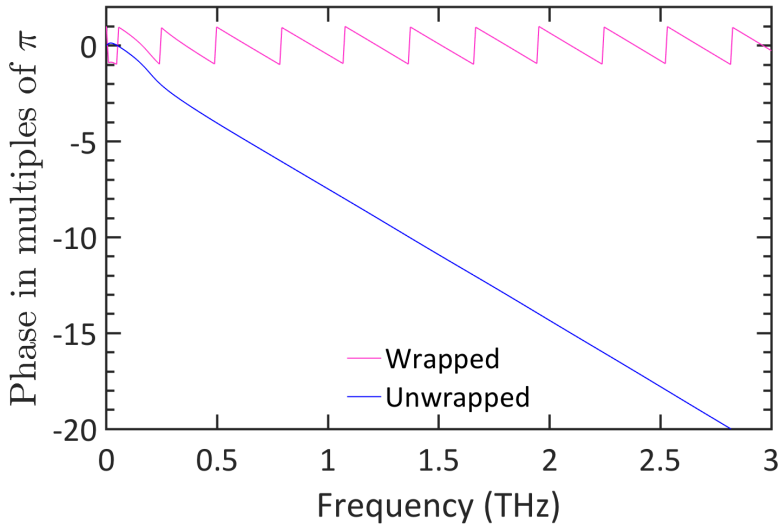

Figure 4.6: Spectral phase of the reference measurement before and after applying MATLAB's phase unwrapping algorithm.

4.4 Demonstration of Material Parameter Extraction for a ZnTe Sample

The zinc-blende ZnTe crystal is one of the most widely used materials as either a THz emitter or a detector and is therefore useful to benchmark our extraction procedure for

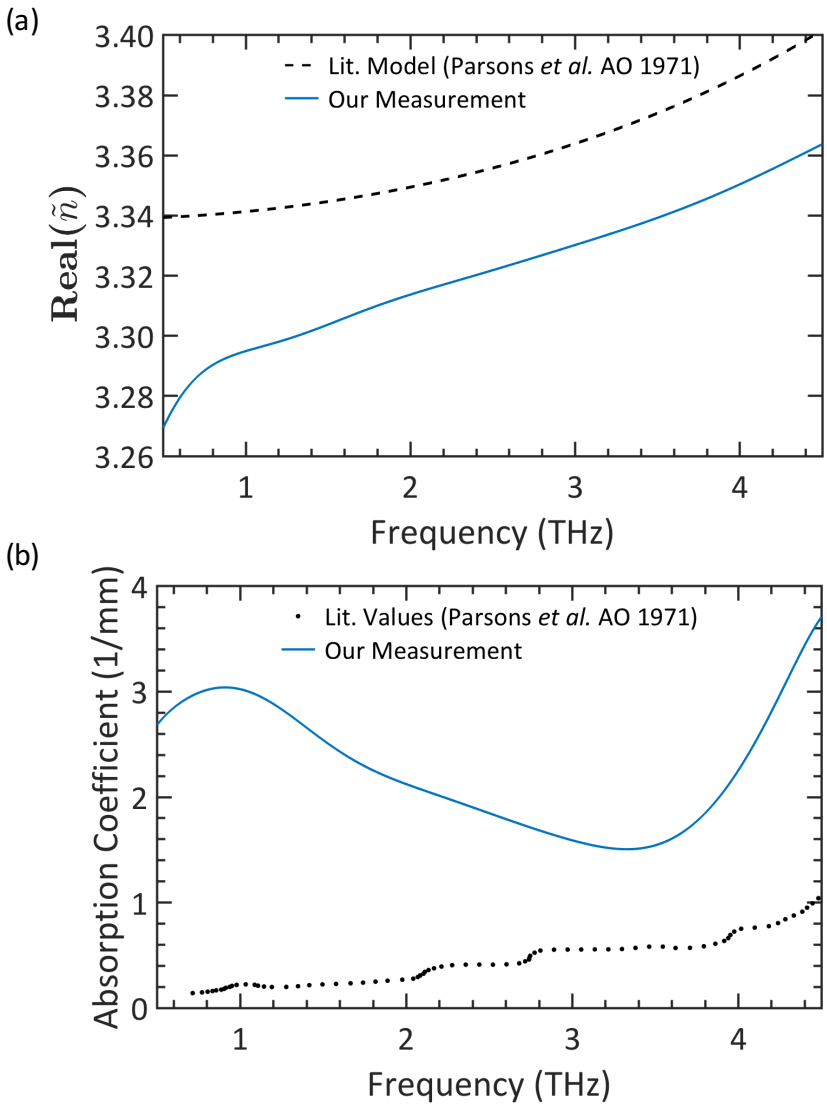

Figure 4.7: Results of our material parameter extraction procedure for a 310 ± 10 μm thick (110)-oriented GaP crystal: (a) real part of the refractive index and (b) power absorption coefficient. Black curves refer to Ref. [61].

THz-TDS. The experimental conditions described in the previous section are repeated here with a (110)-oriented ZnTe crystal as the sample having a thickness specified by the manufacturer of 200 μm. The two measurements with and without the sample in the THz beam path are shown in Fig. 4.8(a) alongside the additional one with the sample placed in the NIR gating arm. From this third measurement, the observed group delay is about -1.3 ps and corresponds to a sample thickness of 201 μm which agrees well with the manufacturer.

The calculated power spectra are shown in Fig. 4.8(b) in dB scale. After applying the same rectangular windowing as in Sect. 4.3, no additional zero padding was performed. These measurements have a spectral resolution of 0.07 THz which, as a reminder, is entirely determined by the scan duration. The blue dashed line at -58.9 dB indicates the noise floor, in the absence of the sample, calculated from the mean spectral power beyond the shown frequency range. Importantly, the sample and reference spectra intersect at around 4.5 THz. As expected, Fig. 4.8(d) shows the power absorption coefficient resulting from

eq. 4.28 which crosses the literature model a little lower at just below 4.4 THz. This feature was also seen in the THz-TDS experiment that was done to calculate the model [69]. Additionally, two peaks are observed at about 1.63 THz and 3.82 THz which were also observed in Refs. [69, 70]. In particular, Ref. [69] was the first experiment to assign these two features to the transverse TA(X) and longitudinal LA(X) phonon absorption lines, respectively. Two years later, Ref. [70] emphasized that these phonon modes are typically forbidden in pure crystals, indicating a departure from crystal purity in composition or in structure. Impurities in the composition of the crystal can occur when dopant materials are added during fabrication while structural defects result from vacancies or dislocations, for example. We observe about the same level of absorption at low frequencies as for GaP in Sect. 4.3, so we favour the former possibility and attribute this result to the presence of free charge carriers.

The resulting real part of the refractive index is shown in Fig. 4.8(c). There is good overall agreement between our results and the literature model of the refractive index for ZnTe [69]. Notably, we see that our results appear insensitive to the presence of the observed phonon absorption peaks since they do not show the distinctive dispersive shape of a resonance as we saw in Fig. 2.6. Ref. [70] have verified this statement by varying the temperature of the sample until the peaks themselves disappeared, a process for which they observed a consistent decrease across the board in the real part of the refractive index.

Figure 4.8: Results of our material parameter extraction procedure for a 201 ± 10 μm thick (110)-oriented ZnTe crystal: (a) measured THz transients; (b) power spectra with the dashed line indicating the noise floor at -58.9 dB; (c) real part of the calculated refractive index; (d) calculated power absorption coefficient. Black curves refer to Ref. [69].

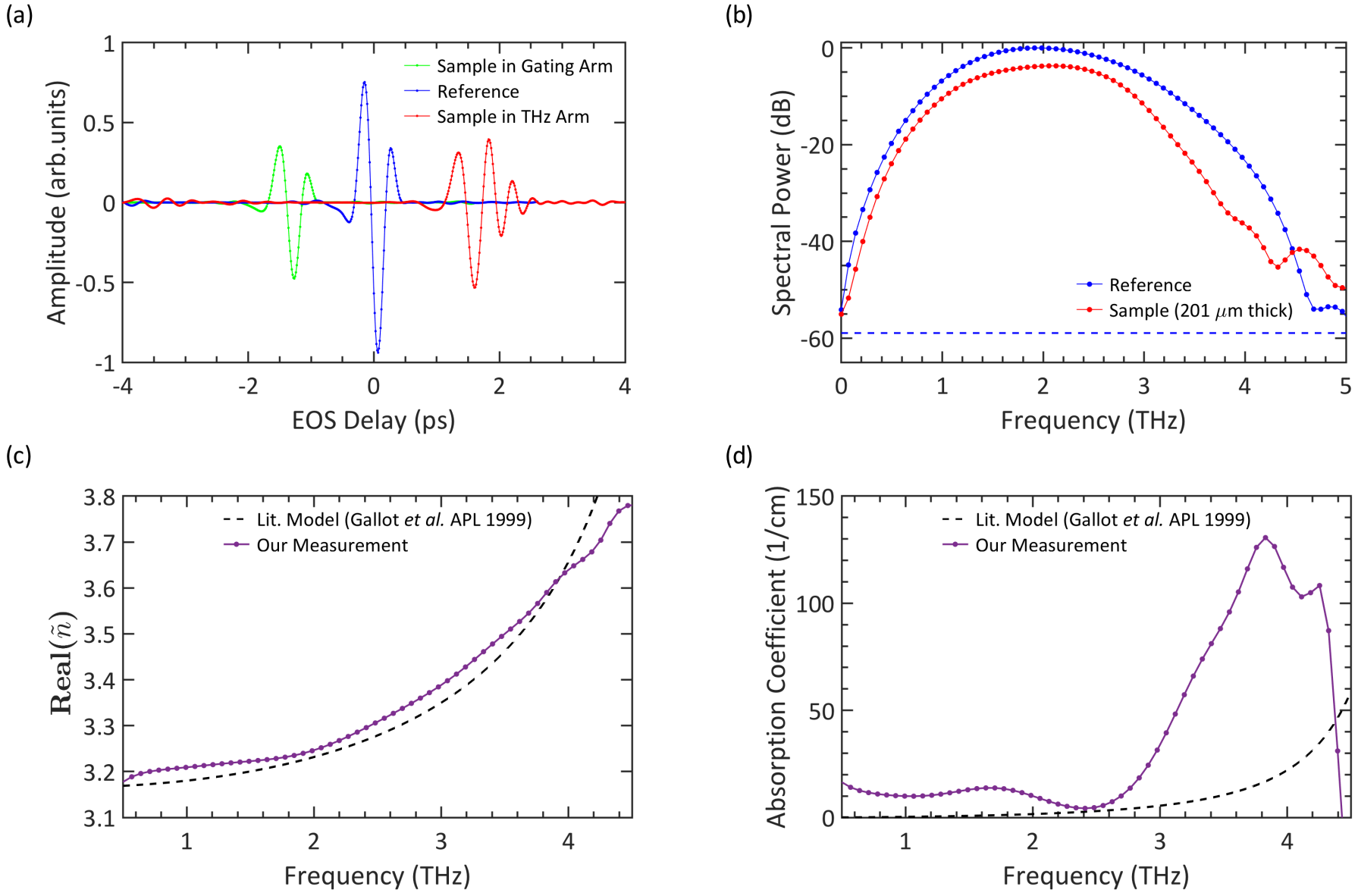

Chapter 5

Conclusion

In this work, the operation of a THz time-domain spectrometer based on nonlinear optical methods has been detailed. In Chapter 2, a theoretical framework for the generation and detection stages was derived based on a one-dimensional solution to the nonlinear optical wave equation. We described the generation of THz pulses from the second-order nonlinear process of optical rectification followed by their subsequent coherent electro-optic detection using the inverse nonlinear process based on the Pockels effect. In Chapter 3, the THz spectrometer was realized in the laboratory through the use of intense, near-infrared femtosecond pulses to seed these nonlinear processes. Furthermore, we discussed the various intrinsic sources of noise that arise in our measurements and their efficient rejection through lock-in detection. In Chapter 4, we outlined a procedure to perform THz-TDS which takes advantage of our coherent detection scheme to extract the real and imaginary parts of the complex refractive index of a sample under study. Our samples of interest were the zinc-blende semiconductor crystals GaP and ZnTe for their widespread popularity in THz science due to their low dispersion and absorption in the THz regime.

There are a number of research directions one can take with our benchmarked THz-TDS system. One example is to extend the system by introducing an additional optical line to pump the samples with NIR light at some delay in time with respect to the probing THz line. Such a pump-probe configuration is referred to as optical-pump/THz-probe (OPTP) spectroscopy. Recall that, in Chapter 4, we attributed the appearance of high absorption at low THz frequencies to the presence of doping agents inherent in our samples. By varying the charge carrier density in the sample as a function of NIR pump fluence, the use of OPTP spectroscopy could extend our technique to the observation and control of ultrafast dynamics on a sub-ps time scale. For example, this technique finds use in the study of the formation of exciton-polariton condensates created in quantum-well heterostructres [49]. Alternatively, methods of utilizing THz radiation continue to prosper from advances in semiconductor fabrication technology. In this vein, a current research effort with our THz spectrometer is to improve dielectric deposition and etching techniques on semiconductor samples with the goal of adjusting their phase-matching properties and leading to the next generation of novel, tunable THz emitters and detectors.

APPENDICES

Appendix A

MATLAB Code for the Numerical Simulation

What follows is the MATLAB code used to numerically simulate THz generation by optical rectification and electro-optic detection. Two external functions are used (`my_XMinorTick.m` and `reorderLegend.m` from the StackExchange), otherwise the code is self-contained. Where appropriate, references to the literature are given.

Verbatim MATLAB Code

```
clear
clc, format compact, format short
set(groot, 'DefaultFigureWindowStyle','docked',...
           'DefaultFigureColor','w',...
           'DefaultLineLineWidth', 2, ...
           'DefaultLineMarkerSize',22,...
           'DefaultAxesFontName', 'Times', ...
           'DefaultAxesFontSize', 26, ...
           'DefaultAxesLineWidth',2, ...
           'DefaultAxesBox', 'on', ...
           'DefaultAxesColor', [1, 1, 1],...
           'DefaultAxesTickLength',[0.02, 0.005]);
close all

nair = 1.000396145;
%^ http://emtoolbox.nist.gov/Wavelength/Edlen.asp
%^ input values: 1035nm, 22C, 1.5bar, 0% RH

%Arrays for all frequencies, wavelengths, wave-vectors
acc = 2^10;
T = 7*1e-12*linspace(-1,1,acc); %[s] temporal domaina
ech = mean(diff(T)); %[s] sampling interval
freq = (-(acc/2):acc/2-1) /acc /ech; %[Hz]
c0 = 2.99792458e8; %[m/s] vacuum speed of light
```

```
lambdaO = 1035*1e-9; %[m] laser central wavelength
vO = c0/lambdaO; %[Hz] laser central frequency
wO = 2*pi*vO; %[rad/s]
w_lO = c0./vO; %[m]
v = freq+vO; %[Hz] laser frequencies
k = (2*pi*v)./c0; %[1/m]
w_l = c0./v; %[m] laser wavelengths
vT = linspace(0,v(end)-v(1),length(v)); %[Hz] THz frequencies
kT = (2*pi*vT)./c0; %[1/m]



%Material Dispersion in the THz - GaP (1971 Parsons)
Se = [2.570, 4.131, 1.390];
Ve = [2.90,  4.27,  5.80]*1e4; %[cm^-1]
S0 = 2.056;
Y0 = 1.1; %[cm^-1]
V0 = 363.4; %[cm^-1] V0*c0*1e12/1e12 = 10.89 THz
Sj = [7.0, 3.5]*1e-4;
Vj = [349.4, 358.4]; %[cm^-1]
Yj = [21.0, 12.6]; %[cm^-1]
% Relative dielectric constant
rel_d = @(v) 1+...
    Se(1)*Ve(1)^2./(Ve(1)^2 - v.^2)+...
    Se(2)*Ve(2)^2./(Ve(2)^2 - v.^2)+...
    Se(3)*Ve(3)^2./(Ve(3)^2 - v.^2)+...
    S0*(1-sum(Sj))*V0^2./(...
    V0^2 - v.^2 + 1i*v*Y0 - V0^2*(...
    Sj(1)*Vj(1)^2./(Vj(1)^2 - v.^2 + 1i*v*Yj(1))+...
    Sj(2)*Vj(2)^2./(Vj(2)^2 - v.^2 + 1i*v*Yj(2))) ); %[v]=cm^-1


func_nT_gap =@(v_)  real(sqrt(rel_d(v_/(c0*1e2)))); %[v_]=Hz
func_eT_gap =@(v_) -imag(sqrt(rel_d(v_/(c0*1e2)))); %[v_]=Hz
nT_gap = func_nT_gap(vT);
eT_gap = func_eT_gap(vT);
aT_gap = eT_gap.*(2*pi*vT)/c0; %[1/m] amplitude absorption
nTc_gap = nT_gap + 1i*eT_gap; %complex refractive index

%Material Dispersion in the NIR - GaP (1971 Parsons)
func_nO_gap = func_nT_gap; %Parsons model extends from microwave
    to visible
nO_gap = func_nO_gap(v);
[~,p0]=min(abs(v - vO));
ng_lO_gap = nO_gap(p0) -...
    w_l(p0).*(nO_gap(p0-1) - nO_gap(p0+1))./(w_l(p0-1) - w_l(p0
        +1));%3.3156

```

```
71
72 figure(1)
73 clf
74 subplot(211)
75
76 yyaxis left
77 plot(vT/1e12,nT_gap,'linew',2)
78 line([0 max(vT)/1e12],[ng_lO_gap ng_lO_gap],'lines','--')
79 ylabel('GaP')
80 ylim([0 12])
81 yticks([0 3 6 9 12])
82 % ylabel('{\bf Real($n$) }','interpreter','latex')
83 text(15,4.5,['$n_g(\lambda_0) =$ ',num2str(ng_lO_gap,'%2.3f')
       ],...
84      'interpreter','LaTeX','fontsize',22,...
85      'color',[0     0.4470     0.7410])
86
87 yyaxis right
88 plot(vT/1e12,aT_gap/1e3,'linew',2)
89 % ylabel('Amplitude Absorption (1/mm)')
90 ylim([0 10])
91 xlim([0 20])
92 xticks(0:5:20)
93 set(gca,'XMinorTick','on')
94
95
96 %Material Dispersion in the THz - ZnTe (1999 Gallot)
97 einf4 = 7.44;
98 edc4 = 2.58;
99 vTO4 = 5.32; %THz
100 yTO4 = 0.025; %THz
101 rel_d =@(v) einf4 + (edc4*vTO4^2)./(vTO4^2 - v.^2 - 2i*yTO4*v); %
       [v]=THz
102
103 func_nT_znte =@(v_) real(sqrt(rel_d(v_/1e12))); %[v_]=Hz
104 func_eT_znte =@(v_) imag(sqrt(rel_d(v_/1e12))); %[v_]=Hz
105 nT_znte = func_nT_znte(vT);
106 eT_znte = func_eT_znte(vT);
107 aT_znte = eT_znte.*(2*pi*vT)/c0; %[1/m] amplitude absorption
108 nTc_znte = nT_znte + 1i*eT_znte; %complex refractive index
109
110 %Material Dispersion in the NIR - ZnTe (1964 Marple)
111 nOfunc_ =@(wl) sqrt(4.27 + 3.01*wl.^2./(wl.^2 - 0.142)); %[wl]=um
112 func_nO_znte =@(v_) nOfunc_(c0*1e6./v_);
113 nO_znte = func_nO_znte(v);
114
115 [~,p0]=min(abs(v - vO));
116 ng_lO_znte = nO_znte(p0) -...
```

```
117       w_l(p0).*(nO_znte(p0-1)-nO_znte(p0+1))./(w_l(p0-1) - w_l(p0
              +1));%2.9727
118
119
120 h212=subplot(212);
121
122 yyaxis left
123 plot(vT/1e12,nT_znte,'linew',2)
124 line([0 max(vT)/1e12],[ng_lO_znte ng_lO_znte],'lines','--')
125 ylabel('ZnTe')
126 ylim([0 12])
127 yticks([0 3 6 9 12])
128 % ylabel('{\bf Real($n$) }','interpreter','latex')
129 aLIM = axis;
130
131 text(9.35,4.25,['$n_g(\lambda_0) =$ ',num2str(ng_lO_znte,'%2.3f')
        ],...
132      'interpreter','LaTeX','fontsize',22,...
133      'color',[0      0.4470      0.7410], 'Parent', h212)
134
135 yyaxis right
136 plot(vT/1e12,aT_znte/1e3,'linew',2)
137 % ylabel('Amplitude Absorption (1/mm)')
138 ylim([0 10])
139 xlim([0 12.5])
140 xticks(0:2.5:12.5)
141 set(gca,'XMinorTick','on')
142
143
144
145 %% Coherence lengths in GaP and ZnTe
146 dk_gap = (2*pi*vT).*abs(ng_lO_gap - nT_gap)/c0; %[1/m]
147 lc_gap = pi./dk_gap; %[m] 1996 Nahata (eq.2) or Boyd (eq. 2.4.8)
148
149 dk_znte = (2*pi*vT).*abs(ng_lO_znte - nT_znte)/c0; %[1/m]
150 lc_znte = pi./dk_znte;%[m] 1996 Nahata (eq.2) or Boyd (eq. 2.4.8)
151
152 figure(2)
153 clf
154 hold on
155 plot(vT/1e12,lc_znte*1e3,'-','color',[0      0.4470      0.7410],...
156      'linewidth',2,'displayname',' ZnTe')
157 plot(vT/1e12,lc_gap*1e3,'r-','linewidth',2,'displayname',' GaP')
158 ylabel('Coherence Length (mm)')
159 xlabel('Frequency (THz)')
160 axis([0 12 0 1.1])
161 yticks(0:.2:1), ytickformat('%2.1f')
162 line([0 vT(end)/1e12],[1.0 1.0],'color','k','lines','--')
```

```
line([0 vT(end)/1e12],[0.310 .310],'color','k','lines','--')
line([0 vT(end)/1e12],[0.20 .20],'color','k','lines','--')

%Control minor ticks
cd('/Users/Aidan/Documents/MATLAB/my_XMinorTick')
my_XMinorTick(2,'k','on')
h=legend('show');
reorderLegend([15 16])
legend boxoff
h.Position = [0.1967    0.7258    0.1250    0.1060];

text(4.15,.945,' $L = 1000$ $\mu$m','interpreter','LaTeX',...
    'fontsize',32,'color','k')
text(5.5,0.36,' $L = 310$ $\mu$m','interpreter','LaTeX',...
    'fontsize',32,'color','k')
text(6,0.25,' $L = 200$ $\mu$m','interpreter','LaTeX',...
    'fontsize',32,'color','k')
set(gca,'fontsize',32)


disp('Predict coherence length at:')
[~,p]=min(abs(vT/1e12 - 4));
disp(['   ',num2str(vT(p)/1e12,'%2.2f'),' THz -> ',...
    num2str(lc_gap(p)*1e3,'%2.2f'),' um'])

fprintf('\n')
disp('Predict phase-matched bandwidth:')
thickness_gap = 220e-6;
[~,pos2]=min(abs(2*lc_gap - thickness_gap));
disp(['GaP:    ',num2str(thickness_gap*1e3,'%2.2f'),' mm -> ',...
    num2str(vT(pos2)/1e12,'%2.2f'),' THz'])

thickness_znte = thickness_gap;
[~,pos3]=min(abs(2*lc_znte - thickness_znte));
disp(['ZnTe:   ',num2str(thickness_znte*1e3,'%2.2f'),' mm -> ',...
    num2str(vT(pos3)/1e12,'%2.2f'),' THz'])



%% Nonlinear Coefficients for GaP and ZnTe

%Chi(2) for GaP
%   eq.1 in Faust Henry Eick PR 173(1968)
%or eq.5 in Faust Henry PR 17(1966)
f0_gap = V0*c0*1e2; %[Hz]
dE_gap = 1e-12; %[m/V] (2005 Casalbuoni)
d14_gap =@(f_) dE_gap*(1 - 0.47*f0_gap^2./...
    ( f0_gap^2 - f_.^2 - 1i*(0.02*f0_gap).*f_ ) );%[f_]=THz
```

```
X2_gap = 2*d14_gap(vT); %[m/V]

%Chi(2) for ZnTe (2005 Casalbuoni & 1999 Leitenstorfer)
f0_znte = vTO4*1e12; %[Hz]
dE_znte = 4.25e-12; %[m/V]
d14_znte =@(f_) dE_znte*(1 - 0.47*f0_znte^2./...
    ( f0_znte^2 - f_.^2 - 1i*(0.02*f0_znte).*f_) ); %[f_]=THz
X2_znte = 2*d14_znte(vT); %[m/V]

figure(3)
clf
yyaxis left
hold on
plot(vT/1e12,abs(X2_gap),'-','displayname',' GaP')
plot(vT/1e12,abs(X2_znte),':','displayname',' ZnTe')
ylabel('$|\chi^{(2)}|$ (pm/V)','interpreter','LaTeX')
yyaxis right
hold on
plot(vT/1e12,angle(X2_gap)/pi,'-','HandleVisibility','off')
plot(vT/1e12,angle(X2_znte)/pi,':','HandleVisibility','off')
ylabel('$Arg[\chi^{(2)}]$ ($\pi$ multiples)','interpreter','LaTeX
    ')
xlabel('Frequency (THz)')
xlim([0 20])
h3 = legend('show');
h3.FontSize = 24;
legend boxoff
set(gca,'linew',2)

% plt = gca;
% plt.YAxis(1).Color = 'm'; %left y-axis colour
% plt.YAxis(2).Color = 'm'; %right y-axis colour
%% Choose pump for optical rectification
%::: loads 3 types of pump beams and you pick one at the end

%%% load PHAROS RA measured via USB spectrometer
Shift = 2;
A1    = 4.7989625821555E4;
xc1   = 1.03779584358558E3 - 2 + Shift; %[nm]
w1    = 5.1966998197966 * 0.8; %[nm]
A2    = 5.8894054011212E4 * 4.1;
xc2   = 1.0310777648997E3 + Shift; %[nm]
w2    = 8.0767811102964 * 1.3; %[nm]
y0    = 294.27754564929;
x     = (c0*1e9)./v; %[nm]
U2_Intensity = y0*0 +...
    sqrt(2/pi)*A2/w2.*exp(-2*(x-xc2).^2/w2^2) +...
    sqrt(2/pi)*A1/w1.*exp(-2*(x-xc1).^2/w1^2);
```

```
U2_field = sqrt(U2_Intensity);
U2_fldfun =@(x_) sqrt(y0*0 +...
    sqrt(2/pi)*A2/w2.*exp(-2*(x_-xc2).^2/w2^2) +...
    sqrt(2/pi)*A1/w1.*exp(-2*(x_-xc1).^2/w1^2) );
spump_PHAROS = U2_field./max(U2_field);


%%% load measured NIR spectra and build a model
cd('/Users/Aidan/Documents/MATLAB/data/Wei Cui data/20180416')
rf = xlsread('NIR_specttrum_1205');
pump_source_loadme = '7p5bar';
switch pump_source_loadme
    case '0bar',   column = 2;
    case '2p5bar', column = 3;
    case '5bar',   column = 4;
    case '7p5bar', column = 5;
    case '10bar',  column = 6;
end
rf_freqs = c0./(rf(end:-1:1,1)*1e-9); %[Hz]
intensity = rf(end:-1:1,column);
intensity = intensity - mean(intensity); %bgnd subtract
intensity(intensity < 0) = 0; %no negative intensities
amplitude = sqrt(intensity);
% fit to data to build gating function:
[~,p1] = min(abs(rf_freqs - v(1)));
[~,p2] = min(abs(rf_freqs - v(end)));
xf = rf_freqs(p1:p2);
yf = amplitude(p1:p2);
pp = spline(xf,[0 yf(:)' 0]);
U2_fieldfunc = @(xx) ppval(pp,xx); %gating function
spump_LOADME = U2_fieldfunc(v)./max(U2_fieldfunc(v));
spump_LOADME(spump_LOADME<0)=0; %no negative intensities


%%% load Gaussian model
% 1) simple trial model:
%     s_gate = @(v_) ...
%         0*exp(-(v_/1e12 - 290).^2./(0.8).^2) +...
%         1*exp(-(v_/1e12 - c0./w_lO/1e12).^2./(10).^2) +...
%         0*exp(-(v_/1e12 - 294).^2./(0.8).^2);
% 2) Gaussian model:  exp(-(x-x0).^2/(2*s.^2)) --> FWHM=2*sqrt(2*
    log(2))*s
%    ^ http://mathworld.wolfram.com/GaussianFunction.html

%0.441
sFWHM_pump = 5; %THz
sigma_pump = sFWHM_pump/(2*sqrt(2*log(2)));
s_pump_ = @(v_) 1*exp(-(v_/1e12 - vO/1e12).^2./sigma_pump.^2 /2);
```

```
spump_GAUSSIAN = s_pump_(v);



%pick pump beam
pump_source = 'gaussian'; %{PHAROS, loadme, gaussian}
disp(['source = ',pump_source])
switch pump_source
    case 'PHAROS'
        spump = spump_PHAROS;
    case 'loadme'
        spump = spump_LOADME;
    case 'gaussian'
        spump = spump_GAUSSIAN;
end

figure(4)
clf
hold on
plot(v/1e12,spump./max(abs(spump)),'r')
ylabel('Amplitude (arb.units)')
xlabel('Frequency (THz)')
axis([280 300 0 1])
yticks(0:0.5:1)
set(gca,'linew',2)

fprintf('\n')
disp('find pump amplitude bandwidth:')
signal = abs(spump)./max(abs(spump));
%search either side for values closest to 0.5
[~,idx(1)] = max(abs(signal)); %location of peak
[~,idx(2)] = min(abs(signal(1:idx(1)) - 0.5)); %search values
    before peak
[~,idx(3)] = min(abs(signal(idx(1):end) - 0.5)); %search values
    after peak
idx(3) = idx(3)+idx(1)-1; %update index to after peak
bwFWHM=abs( v(idx(3)) - v(idx(2)) )/1e12;
disp(['  Peak = ',num2str(v(idx(1))/1e12,'%.1f'),' THz'])
disp(['  FWHM = ',num2str(bwFWHM,'%.1f'),' THz'])


line([v(1)/1e12,v(end)/1e12],[0.5,0.5],...
    'lines','--','color',[0    0.4470    0.7410],'linew',3)
line([v(idx(2))/1e12,v(idx(2))/1e12],[0,1],...
    'lines','--','color',[0    0.4470    0.7410],'linew',3)
line([v(idx(3))/1e12,v(idx(3))/1e12],[0,1],...
    'lines','--','color',[0    0.4470    0.7410],'linew',3)

```

```
351 text(294,0.56,['FWHM = ',num2str(bwFWHM,'%2.1f'),' THz'],...
352     'fontsize',32,'color',[0      0.4470      0.7410])
353 set(gca,'fontsize',36)
354
355
356
357 %% Phase-Matching (works for multiple GaP emitters / same GaP
    detector)
358
359 G_Lgap = 250e-6*[1,2,4,8]; %[m] THz emitter thickness
360 D_Lgap = 300e-6; %[m] THz detector thickness
361 colorme_gap = flipud(colormap(jet(numel(G_Lgap)+1)*.8)); %red to
    blue
362
363
364 clear sgen_gap
365 clear sdet_gapgap
366
367 figure(5)
368 clf
369 hold on
370 %--- Generation Phase Matching ---
371 G_prefactors = sqrt(4/3)*(2*pi*vT).*X2_gap./(2*nTc_gap*c0);
372 %^ sqrt(4/3) is geometric, see 2001 Chen et al. JOSAB 18 (eq.9)
373
374 for kk = length(G_Lgap):-1:1 %for multiple crystal thicknesses
375     % predict lowest-frequency minimum in generated THz spectrum
376     [~,pos2(kk)]=min(abs(2*lc_gap - G_Lgap(kk))); %2*Lcoh == L
377     lowmin(kk) = vT(pos2(kk))/1e12; %location of lowest predicted
        minimum
378
379
380     G_ethz = zeros(1,numel(vT)); %cleared upon iteration
381     %  For w3=w2-w1
382     for jj = 1:length(v) %select w1
383         for ii = jj:length(v) %select w2>w1
384             %  wavevector mismatch: K1(-w1)+K2(w2)-K3(w3)
385             dK = ((-nO_gap(jj)*k(jj)...
386                    +nO_gap(ii)*k(ii))...
387                    -nTc_gap(ii-jj+1)*kT(ii-jj+1)); %[1/m]
388
389             G_ethz(ii-jj+1) = G_ethz(ii-jj+1) +...
390                 spump(jj)*spump(ii).*( (exp(-1i*dK.*G_Lgap(kk))
                    -1) / dK );
391         end
392     end
393     sgen_gap(kk,:) = G_prefactors.*G_ethz;
394
```

```
395       legendmatrix_gap{kk} = [' gen ' num2str(G_Lgap(kk)*1e3,'%.2f'
              )];
396       plot( vT/1e12,abs(sgen_gap(kk,:))./...
397                         max(abs(sgen_gap(length(G_Lgap),:))),':',...
398           'color',colorme_gap(kk,:),...
399           'displayname',legendmatrix_gap{kk})
400
401       [~,peak_gap(kk)] = max(abs(sgen_gap(kk,:))); %find peak
402       peakval_gap(kk) = abs(sgen_gap(kk,peak_gap(kk)))./...
403                         max(abs(sgen_gap(length(G_Lgap),:)));
404       disp(['Thickness = ',num2str(G_Lgap(kk)*1e3,'%2.2f'),' mm ->
              min at ',num2str(lowmin(kk),'%2.2f'),' THz -> peak at ',
              num2str(vT(peak_gap(kk))/1e12,'%2.2f'),' THz -> value at
              peak = ',num2str(peakval_gap(kk),'%2.2f')])
405
406   end
407   sgen_gap(:,1) = 0; %erase NaN at DC (from dividing by 0 freq)
408   xlim([0  8])
409
410
411   % ---- Electro-Optic Detection (here fixed for a GaP detector) ----
412   %Spectral autocorrelation of NIR gate
413   s_gate = s_pump_; %same gate as pump
414   acf = zeros(1,numel(vT));
415   for i=1:numel(v)
416       acf(i) = sum(s_gate(v).*s_gate(v-vT(i)));
417   end
418
419   %Phase matching in GaP detector:
420   %DeltaK = -Ka(vO+vT) + Kb(vT) + Kc(vO)
421   %^ see eq.64 in Gallot_Grisch_1999
422   for ii=1:numel(v) %find not-quite k-vectors
423       Ka = func_nO_gap(vO+vT(ii)) *(vO+vT(ii));
424       Kb = func_nT_gap(vT(ii))    *vT(ii);
425       Kc = func_nO_gap(vO)        *vO;
426       Delta_K_gap(ii) = (-Ka + Kb + Kc)*2*pi/c0; %[rad/m]
427   end
428   phasematching_gap = (exp(1i*Delta_K_gap*D_Lgap)-1)./(1i*
          Delta_K_gap);
429   phasematching_gap(1) = 0; %erase NaN at DC
430   Teos_gap = phasematching_gap.*acf;
431   for mm = length(G_Lgap):-1:1
432           sdet_gapgap(mm,:) = sgen_gap(mm,:).*Teos_gap;
433
434       plot( vT/1e12,abs(sdet_gapgap(mm,:))./max(max(abs(sdet_gapgap
              )))),...
435           'color',colorme_gap(mm,:),'displayname',[legendmatrix_gap
                {mm},', det ',...
```

```
436             num2str(D_Lgap(kk)*1e3,'%.2f')])
437 end
438 h5=legend('show');
439 title(h5,'Thickness (mm)')
440 legend boxoff
441 xticks(0:12)
442 xlabel('Frequency (THz)')
443 ylabel('Amplitude (arb.units)')
444
445
446 %%
447
448 [~,pa]=min(abs(acf./max(acf) - 0.5));
449 line([0 vT(pa)/1e12],[0.5 0.5],'color','k','lines','--')
```

Bibliography

[1] J. P. Gordon, H. J. Zeiger, and C. H. Townes. The maser-new type of microwave amplifier, frequency standard, and spectrometer. *Physical Review*, 99(4):1264, 1955.

[2] T. H. Maiman. Stimulated optical radiation in ruby. *Nature*, 187:493, 1960.

[3] A. L. Schawlow and C. H. Townes. Infrared and optical masers. *Physical Review*, 112(6):1940, 1958.

[4] Charles H. Townes. *How the Laser Happened*. Oxford University Press, New York, 1999.

[5] Yeun-Ron Shen. Reflections on the early days of thz spectroscopy. IRMMW-THz, 2015.

[6] P. F. Moulton. Spectroscopic and laser characteristics of Ti:Al_2O_3. *J. Opt. Soc. Am. B*, 3(1):125, 1986.

[7] P. H. Siegel. Terahertz Pioneer: David H. Auston. *IEEE Trans. Terahertz Sci. Technol.*, 1(1):5–8, 2011.

[8] N. Horiuchi. Bright terahertz sources. *Nature Photon.*, 7:670–671, 2013.

[9] P. H. Siegel. Terahertz Pioneer: Daniel R. Grischkowky. *IEEE Trans. Terahertz Sci. Technol.*, 2(4):377–382, 2012.

[10] G. P. Swift. *Propagation of terahertz radiation in non-homogeneous materials and structures*. PhD thesis, Durham theses, Durham University, 2016.

[11] D. Abbott and X.-C. Zhang. Scanning the issue: T-ray imaging, sensing, and retection. *Proceedings of the IEEE*, 95(8):1509, 2007.

[12] M. Tonouchi. Cutting-edge terahertz technology. *Nature Photon.*, 1:97–105, 2007.

[13] M. Razeghi, Q. Y. Lu, N. Bandyopadhyay, W. Zhou, D. Heydari, Y. Bai, and S. Slivken. Quantum cascade lasers: from tool to product. *Optics Express*, 23(7):8462, 2015.

[14] S. S. Dhillon et al. The 2017 terahertz science and technology roadmap. *J. Phys. D*, 23(7):8462, 2015.

[15] R. A. Lewis. A review of terahertz sources. *Jour. Phys. D: Appl. Phys*, 47:374001, 2014.

[16] P. R. Smith, D. H. Auston, and M. C. Nuss. Subpicosecond photoconducting dipole antennas. *IEEE J. Quantum Electron.*, 24(2):255, 1988.

[17] K. P. Cheung, D. H. Auston, and M. C. Nuss. Subpicosecond photoconducting dipole antennas. *IEEE J. Quantum Electron.*, 24(2):255, 1988.

[18] Ch. Fattinger and D. Grischkowsky. Point source terahertz optics. *Applied Physics Letters*, 53(16):1480, 1989.

[19] Q. Wu and X.-C. Zhang. Free-space electro-optic sampling of terahertz beams. *Applied Physics Letters*, 67(24):3523, 1995.

[20] S. Keiber, S. Sederberg, A. Schwarz, M. Trubetskov, V. Pervak, F. Krausz, and N. Karpowicz. Electro-optic sampling of near-infrared waveforms. *Nature Photon.*, 10:159, 2016.

[21] D. Strickland and G. Mourou. Compression of amplified chirped optical pulses. *Optics Communications*, 55:447, 1985.

[22] C. E. Cook. Pulse compression - key to more efficient radar transmission. *Proceedings of the IEEE*, 48:310, 1960.

[23] L. Xu, X.-C. Zhang, and D. H. Auston. Terahertz beam generation by femtosecond optical pulses in electro-optic materials. *Applied Physics Letters*, 61(15):1784, 1992.

[24] G. A. Mourou, D. M. Bloom, and C.-H. Lee. Picosecond electronics and optoelectronics. Proceedings of the Topical Meeting, 1985.

[25] M. Bass, P. A. Franken, J. F. Ward, and G. Weinreich. Optical rectification. *Physical Review Letters*, 9(11):446, 1962.

[26] Robert W. Boyd. *Nonlinear Optics*. Academic Press, Burlington, Massachusetts, third edition, 2008.

[27] J. Hebling, G. Almási, I. Z. Kozma, and J. Kuhl. Velocity matching by pulse front tilting for large-area THz-pulse generation. *Optics Express*, 10(21):1161, 2002.

[28] J. A. Fulop, Z. Ollmann, Cs. Lombosi, C. Skrobol, S. Klingebiel, L. Palfalvi, F. Krausz, S. Karsch, and J. Hebling. Efficient generation of THz pulses with 0.4 mJ energy. *Optics Express*, 2(17):20155, 2014.

[29] R. Huber, A. Brodschelm, F. Tauser, and A. Leitenstorfer. Generation and field-resolved detection of femtosecond electromagnetic pulses tunable up to 41 THz. *Applied Physics Letters*, 76(22):3191, 2000.

[30] M. Knorr, J. Raab, M. Tauer, P. Merkl, D. Peller, E. Wittmann, E. Riedle, C. Lange, and R. Huber. Phase-locked multi-terahertz electric fields exceeding 13 MV/cm at 190 kHz repetition rate. *Optics Letters*, 42(21):4367, 2017.

[31] B. Clough, J. Dai, and X.-C. Zhang. Laser air photonics: beyond the terahertz gap. *Materials Today*, 15:50, 2012.

[32] C. Vicario, M. Jazbinsek, A. V. Ovchinnikov, O. V. Chefonov, S. I. Ashitkov, M. B. Agranat, and C. P. Hauri. High efficiency thz generation in DSTMS, DAST and OH1 pumped by Cr:forsterite laser. *Optics Express*, 23(4):4573, 2015.

[33] H. A. Hafez, X. Chai, A. Ibrahim, S. Mondal, D. Férachou, X. Ropagnol, and T. Ozaki. Intense terahertz radiation and their applications. *Journal of Optics*, 18(9):093004, 2016.

[34] H. Y. Hwang et al. A review of non-linear terahertz spectroscopy with ultrashort tabletop-laser pulses. *Journal of Modern Optics*, 62(18):1447, 2014.

[35] K. Aoki, J. Savolainen, and M. Havenith. Broadband terahertz pulse generation by optical rectification in GaP crystals. *Applied Physics Letters*, 110(20):201103, 2017.

[36] A. Schneider, M. Neis, M. Stillhart B. Ruiz, R. U. A. Khan, and P. Gunter. Generation of terahertz pulses through optical rectification in organic DAST crystals: theory and experiment. *J. Opt. Soc. Am. B*, 23(9):1822, 2006.

[37] F. Blanchard et al. Generation of 1.5 μJ single-cycle terahertz pulses by optical rectification from a large aperture ZnTe crystal. *Optics Express*, 15(20):13212, 2007.

[38] T. J. Carrig, G. Rodriguez, T. S. Clement, A. J. Taylor, and K. R. Stewart. Scaling of terahertz radiation via optical rectification in electro-optic crystals. *Applied Physics Letters*, 66(2):121, 1995.

[39] A. Rovere et al. Generation of high-field terahertz pulses in an HMQ-TMS organic crystal pumped by an ytterbium laser at 1030 nm. *Optics Express*, 26(3):2509, 2018.

[40] K. L. Vodopyanov. Optical thz-wave generation with periodically-inverted GaAs. *Laser & Photon. Rev.*, 2:11, 2008.

[41] X. Zheng, A. Sinyukov, and L. M. Hayden. Broadband and gap-free response of a terahertz system based on a poled polymer emitter-sensor pair. *Applied Physics Letters*, 87(8):081115, 2005.

[42] C. Vicario, A. V. Ovchinnikov, S. I. Ashitkov, M. B. Agranat, V. E. Fortov, and C. P. Hauri. Generation of 0.9-mJ thz pulses in DSTMS pumped by a Cr:Mg_2SiO_4 laser. *Optics Letters*, 39(23):6632, 2014.

[43] F. Brunner et al. Diode-pumped femtosecond Yb:$KGd(WO_4)_2$ laser with 1.1-W average power. *Optics Letters*, 25(15):1119, 2000.

[44] J. Zhang, K. F. Mak, and O. Pronin. Kerr-lens mode-locked 2-m thin-disk lasers. *IEEE J. Sel. Top. Quantum Electron.*, 24(5):1–11, 2018.

[45] P. R. Griffith and J. A. de Haseth. Fourier transform infrared spectrometry. 2007.

[46] S. S. Ng, Z. Hassan, and H. A. Hassan. Kramers-Kronig analysis of infrared reflectance spectra with a single resonance. *Jurnal Teknologi*, 44(76):67, 2006.

[47] M. Autore, P. Di Pietro, A. Di Gaspare, F. D'Apuzzo, F. Giorgianni, M. Brahlek, N. Koirala, S. Oh, and S. Lupi. Terahertz plasmonic excitations in Bi_2Se_3 topological insulator. *J. Phys.: Condens. Matter*, 29:183002, 2017.

[48] G. C. Cho, P. Y. Han, and X.-C. Zhang. Time-resolved THz phonon spectroscopy in semiconductors. ThU2 CLEO Pacific Rim, 1999.

[49] J.-M. Ménard, C. Poellmann, M. Porer, U. Leierseder, E. Galopin, A. Lematre, A. Amo, J. Bloch, and R. Huber. Revealing the dark side of a bright exciton-polariton condensate. *Nature Communications*, 5(4648), 2014.

[50] T. Hong et al. Terahertz time-domain and fourier-transform infrared spectroscopy of traditional Korean pigments. *J. Korean Phys. Soc.*, 64(5):727, 2014.

[51] P. U. Jepsen, D. G. Cooke, and M. Koch. Terahertz spectroscopy and imaging - modern techniques and applications. *Laser Photonics Rev.*, 5(1):124, 2011.

[52] J. B. Baxter and G. W. Guglietta. Terahertz spectroscopy. *Anal. Chem.*, 83(12):4342, 2011.

[53] D. Turton, T. Harwood, A. Lapthorn, E. Ellis, and K. Wynne. Ultrabroadband terahertz spectroscopies of biomolecules and water. Proc. SPIE 8623, Ultrafast Phenomena and Nanophotonics XVII, 2013.

[54] M. Naftaly, R. G. Clarke, D. A. Humphreys, and N. M. Ridler. Metrology state-of-the-art and challenges in broadband phase-sensitive terahertz measurements. *Proceedings of the IEEE*, 105(6):1151, 2017.

[55] Yeun-Ron Shen. *The Principles of Nonlinear Optics*. John Wiley & Sons, Hoboken, New Jersey, 1984.

[56] David K. Cheng. *Field and Wave Electromagnetics*. Addison-Wesley, Boston, Massachusetts, 1983.

[57] T. Brabec and F. Krausz. Nonlinear optical pulse propagation in the single-cycle regime. *Physical Review Letters*, 78(17):3282, 1997.

[58] A. Sommer *et al.* Attosecond nonlinear polarization and lightmatter energy transfer in solids. *Nature Letters*, 534:86, 2016.

[59] F. Schapper. *THz-Spektroskopie von Graphit und Erzeugung geformter Laserpulse im mittleren Infrarot*. PhD thesis, Freien Universität Berlin, 2005.

[60] W. H. Streyer. *Reststrahlen band optics for the advancement of far-infrared optical architecture*. PhD thesis, University of Illinois at Urbana-Champaign, 2016.

[61] W. L. Faust and C. H. Henry. Mixing of visible and near-resonance infrared light in GaP. *Physical Review Letters*, 17(25):1265, 1966.

[62] W. L. Faust, C. H. Henry, and R. H. Eick. Dispersion in the nonlinear susceptibility of GaP near the reststrahl band. *Physical Review*, 173(3):781, 1968.

[63] A. Leitenstorfer, S. Hunsche, J. Shah, M. C. Nuss, and W. H. Knox. Detectors and sources for ultrabroadband electro-optic sampling: Experiment and theory. *TESLA Report 2005-01*, 2005.

[64] S. Casalbuoni, H. Schlarb, B. Schmidt, P. Schmüser, B. Steffen, and A. Winter. Numerical studies on the electro-optic sampling of relativistic electron bunches. *TESLA Report 2005-01*, 2005.

[65] Q. Chen, M. Tani, Z. Jiang, and X.-C. Zhang. Electro-optic transceivers for terahertz-wave applications. *Applied Physics Letters*, 74(11):1516, 1999.

[66] D. Han. *Lattice vibrations of mineral and polarization dependence of material in a slit using terahertz waves*. PhD thesis, Korea Advanced Institute of Science and Technology, 2016.

[67] Mary L. Boas. *Mathematical Methods in the Physical Sciences*. John Wiley & Sons, Hoboken, New Jersey, second edition, 1983.

[68] Otfried Madelung. *Semiconductors: Data Handbook*. Springer, New York, third edition, 2004.

[69] G. Gallot, J. Zhang, R. W. McGowan, T.-I. Jeon, and D. Grischkowsky. Measurements of the THz absorption and dispersion of ZnTe and their relevance to the electro-optic detection of thz radiation. *Applied Physics Letters*, 74:3450, 1999.

[70] M. Schall, M. Walther, and P. Uhd Jepsen. Fundamental and second-order phonon processes in CdTe and ZnTe. *Physical Review B*, 64:094301, 2001.

[71] D. T. F. Marple. Refractive index of ZnSe, ZnTe, and CdTe. *Journal of Applied Physics*, 35(3):539, 1964.

[72] D. F. Parsons and P. D. Coleman. Far infrared optical constants of gallium phosphide. *Applied Optics*, 10(7):1683, 1971.

[73] A. S. Barker Jr. Dielectric dispersion and phonon line shape in gallium phosphide. *Physical Review*, 165(3):917, 1968.

[74] W. L. Bond. Measurement of the refractive indices of several crystals. *Journal of Applied Physics*, 36(5):1674, 1965.

[75] A. Nahata, A. S. Weling, and T. F. Heinz. A wideband coherent terahertz spectroscopy system using optical rectification and electro-optic sampling. *Applied Physics Letters*, 69(16):2321, 1997.

[76] L. Gingras, W. Cui, A. W. Schiff-Kearn, J.-M. Ménard, and D.G. Cooke. Active phase control of terahertz pulses using a dynamic waveguide. *Optics Express*, 26(11):13876, 2018.

[77] Q. Wu and X.-C. Zhang. 7 terahertz broadband GaP electro-optic sensor. *Applied Physical Letters*, 70(14):1784, 1997.

[78] P. C. M. Planken, H.-K. Nienhuys, H. J. Bakker, and T. Wenckebach. Measurement and calculation of the orientation dependence of terahertz pulse detection in ZnTe. *J. Opt. Soc. Am. B*, 18(3):313, 2001.

[79] J. Hebling, K.-L. Yeh, M. C. Hoffmann, B. Bartal, and K. A. Nelson. Generation of high-power terahertz pulses by tilted-pulse-front excitation and their application possibilities. *J. Opt. Soc. Am. B*, 7825(7):B6, 2004.

[80] W. D. Johnston Jr. and I. P. Kaminow. Contributions to optical nonlinearity in GaAs as determined from raman scattering efficiencies. *Physical Review*, 188:1209, 1969.

[81] Y. Berozashvili, S. Machavariani, A. Natsvlishvili, and A. Chirakadze. Dispersion of the linear electro-optic coefficients and the non-linear susceptibility in GaP. *J. Phys. D: Appl. Phys.*, 22:682, 1989.

[82] Q. Wu and X.-C. Zhang. Ultrafast electro-optic field sensors. *Applied Physics Letters*, 68:1604, 1996.

[83] G. Sharma, K. Singh, I. Al-Naib, R. Morandotti, and T. Ozaki. Terahertz detection using spectral domain interferometry. *Optics Letters*, 37(20):4338, 2012.

[84] G. Gallot and D. Grischkowsky. Electro-optic detection of terahertz radiation. *J. Opt. Soc. Am. B*, 16(8):1204, 1999.

[85] B. Wu, L. Cao, Z. Zhang, Q. Fu, and Y. Xiong. Terahertz electro-optic sampling in thick ZnTe crystals below the reststrahlen band with a broadband femtosecond laser. *IEEE Trans. THz Sci. Technol.*, 8(3):305, 2018.

[86] W. Cui, A. W. Schiff-Kearn, E. Zhang, N. Couture, F. Tani, D. Novoa, P. St.J. Russell, and J.-M. Ménard. Broadband and tunable terahertz source using argon-filled hollow-core photonic crystal fiber. *APL Photonics*, 3:111301, 2018.

[87] Jean-Claude Diels and Wolfgang Rudolph. *Ultrashort Laser Pulse Phenomena*, chapter 9.3.3.1, page 469. Academic Press, New York, second edition, 2006.

[88] G. Polónyi, M. I. Mechler, J. Hebling, and J. A. Fülöp. Prospects of semiconductor terahertz pulse sources. *IEEE J. Quantum Electron.*, 23(4):8501508, 2017.

[89] Claude Rulliére. *Femtosecond Laser Pulses*. Springer, New York, second edition, 2005.

[90] Light Conversion Ltd. *PHAROS laser manual (model PH1-SP-1.5mJ)*. 2017.

[91] T. H. Isaac, W. L. Barnes, and E. Hendry. Determining the terahertz optical properties of subwavelength films using semiconductor surface plasmons. *Applied Physics Letters*, 93:241115, 2008.

[92] T. Hattori, R. Rungsawang, K. Ohta, and K.Tukamoto. Gaussian beam analysis of temporal waveform of focused terahertz pulses. *Jpn. J. Appl. Phys.*, 41(8):5198, 2002.

[93] Gwilym M. Jenkins and Donald G. Watts. *Spectral analysis and its appliations*. Holden-Day, San Francisco, 1968.

[94] G. Bradley Armen. Phase sensitive detection: the lock-in amplifier. http://www.phys.utk.edu/labs/modphys/Lock-In%20Amplifier%20Experiment.pdf, 2008. Appendix A.

[95] Craig. The RC Filter Transfer Function. http://www.analogzoo.com/2015/12/deriving-the-rc-filter-transfer-function/, 2015.

[96] Zurich Instruments. Principles of lock-in detection and the start of the art. https://www.zhinst.com/sites/default/files/li_primer/zi_whitepaper_principles_of_lock-in_detection.pdf, 2016.

[97] Stanford Research Systems. Model SR830m Lock-In Amplifier. https://www.thinksrs.com/downloads/pdfs/manuals/SR830m.pdf, 2011.

[98] H. Nyquist. Thermal agitation of electric charge in conductors. *Physical Review*, 32(1):110, 1928.

[99] M. Porer, J.-M. Ménard, and R. Huber. Shot noise reduced terahertz detection via spectrally postfiltered electro-optic sampling. *Optics Letters*, 2639(8):2435, 2014.

[100] G. Zhao, R. N. Schouten, N. van der Valk, W. T. Wenckebach, and P. C. M. Planken. A terahertz system using semi-large emitters: noise and performance characteristics. *Phys. Med. Biol.*, 47(21):3699, 2002.

[101] S. Mickan, J. Xu, J. Munch, X.-C. Zhang, and D. Abbott. The limit of spectral resolution in thz time-domain spectroscopy. *Proceedings of the SPIE*, 5277:54, 2004.

[102] C. Riek, D. V. Seletskiy, A. S. Moskalenko, J. F. Schmidt, P. Krauspe, S. Eckart, S. Eggert, and A. Leitenstorfer. Direct sampling of electric-field vacuum fluctuations. *Science*, 350:420, 2015.

[103] Keith Ruddick. Noise Measurements. http://spa-mxpweb.spa.umn.edu/resources/ExpWriteups/LabManNoise.pdf, 2009.

[104] Tony Tyson. Manual for Physics 123, Project 1, Shot Noise. http://123.physics.ucdavis.edu/shot_files/ShotNoise.pdf, 2013.

[105] F. N. Hooge. $1/f$ noise sources. *IEEE Trans. Electron Devices*, 41(11):1926, 1994.

[106] Y. Shen, T. Watanabe, D. A. Arena, C.-C. Kao, J. B. Murphy, T. Y. Tsang, X. J. Wang, and G. L. Carr. Nonlinear cross-phase modulation with intense single-cycle terahertz pulses. *Physical Review Letters*, 99:043901, 2007.

[107] J. Faure, J. van Tilborg, R. A. Kaindl, and W. P. Leemans. Modelling laser-based table-top thz sources: Optical rectification, propagation and electro-optic sampling. *Opt. Quant. Electron.*, 36(8):681, 2004.

[108] A. Tomasino, A. Parisi, S. Stivala, P. Livreri, A. C. Cino, A. C. Busacca, M. Peccianti, and R. Morandotti. Wideband thz time domain spectroscopy based on optical rectification and electro-optic sampling. *Sci. Rep.*, 3, 2013. Art. no. 3116.

[109] W. Withayachumnankul et al. T-ray sensing and imaging. *Proceedings of the IEEE*, 95:1528, 2003.

[110] M. van Exter, Ch. Fattinger, and D. Grischkowsky. Terahertz time-domain spectroscopy of water vapor. *Optics Letters*, 14:1128, 1989.

[111] H. Igawa, T. Mori, and S. Kojima. Terahertz time-domain spectroscopy of congruent $LiNbO_3$ and $LiTaO_3$ crystals. *Jpn. J. Appl. Phys.*, 53(5S1):05FE01, 2014.

[112] M. H. Kristensen. *Optimisation and Benchmarking of a Terahertz Time-Domain Spectrometer*. PhD thesis, Aalborg University, 2017.

[113] D. Grischkowsky, S. Keiding, M. van Exter, and Ch. Fattinger. Far-infrared time-domain spectroscopy with terahertz beams of dielectrics and semiconductors. *J. Opt. Soc. Am. B.*, 7:2006, 1990.